Engineering synthetic cytokine receptors to utilize monoclonal antibodies as ligands

Inaugural-Dissertation

Zur Erlangung des Doktorgrades
Der Mathematisch-Naturwissenschaftlichen Fakultät
Der Heinrich-Heine-Universität Düsseldorf

Vorgelegt von

Christoph Wittich
Aus Coesfeld

Düsseldorf, März 2025

Aus dem Institut für Molekularbiologie und Biochemie II
des Universitätsklinkums Düsseldorf und
der Heinrich-Heine- Universität Düsseldorf

Gedruckt mit der Genehmigung der

Mathematisch-Naturwissenschaftlichen Fakultät der

Heinrich-Heine-Universität Düsseldorf

Referent: Prof. Dr. rer. nat. Jürgen Scheller

Korreferent: Prof. Dr. rer. nat. Lutz Schmitt

Tag der mündlichen Prüfung: 23.06.2025

I Met a Genius

I met a genius on the train today
About six years old he sat beside me
And as the train ran along the coast
We came to the ocean
And we both looked out the
Window at the ocean
And then he looked at me and said
"It's not pretty"
It was the first time I'd realized that

Charles Bukowski

Table of contents

I Abbreviations

(v/w) volume/weight

µg microgram

AIP anti-idiotypic palivizumab

APS ammonium persulfate

BP base pair

CAR chimeric antigen receptors

CSF colony-stimulating factor

CT-1 cardiotrophin 1

CNTF ciliary neurotrophic factor

DMEM dulbecco's modified eagle medium

DMSO dimethyl sulfoxide

DNA deoxyribonucleic acid

DISC death-inducing signaling complex

E.coli escherichia coli

EGFR epidermal growth factor receptor

EPOR erythropoietin receptor

ECD extracellular domain

FACS fluorescence-activated cell sorting

FBS fetal bovine serum

Fc fragment crystallizable region

FDA food and drug administration

GP130 glycoprotein 130

GEMS generalized extracellular molecule sensors

H hour

HER3 human epidermal growth factor receptor 3

Ig immunoglobulin

IL interleukin

IL-6R interleukin-6 receptor

ICD intracellular domain

IFN interferons

JAK janus kinase

KD dissociation constant

KDA kilodalton

LIF leukemia inhibitory factor

MAP mitogen-activated protein

MAPK mitogen-activated protein kinase

mg/ml milligram/milliliter

min minute

ml milliliter

mRNA messenger rna

NG nanogram

NM nanomole

OSM oncostatin m

PCR polymerase chain reaction

PDB protein data bank

pDNA plasmid dann

pg picogram

PI3K phosphoinositide-3-kinase

RSV respiratory syncytial virus

RT room temperature

SAXS small-angle x-ray scattering

scFV single-chain variable fragment

SDS-PAGE sodium dodecyl sulfate polyacrylamide gel electrophoresis

s second

SEC size exclusion chromatography

SHP2 src homology region 2 domain-containing phosphatase 2

SOCS suppressors of cytokine signaling

SPR surface plasmon resonance

STAT signal transducers and activators of transcription

TMD transmembrane domain

TNF tumor necrosis factor

TS twin-strep-tag

U unitVHH heavy-chain antibody

II Figures

III Tables

IV Equations

1 Introduction

1.1 About Computing

The quest to create computational systems spans over two millennia, beginning with the remarkable Antikythera mechanism from 200 BC. This ancient Greek orrery, discovered in a Hellenistic shipwreck, functioned as an analog computer capable of predicting astronomical positions and eclipses decades in advance, though it likely served primarily as an academic demonstration tool(*1-3*). It would take humanity nearly 2000 years to advance computational technology significantly with Charles Babbage's "difference engine", an automatic mechanical calculator designed for navigational calculations(*4, 5*). While Babbage conceptualized a more sophisticated device capable of arithmetic logic and conditional branching, manufacturing limitations of the era prevented its realization(*6*).

The invention of the transistor in 1947 by Bardeen, Brattain, and Shockley at Bell Labs marked a revolutionary advancement in computational capability(*7*). This breakthrough enabled the development of microchips and modern computing devices, with contemporary microprocessors containing up to 134 billion transistors organized into logic gates(*8*).

Now, synthetic biology aims to translate these computational principles into living systems by creating controllable and consistent biological logic gates. While simple on/off switches have been achieved, developing more complex operations like AND-gates or programmable circuits remains challenging, particularly in eukaryotic cells(*9-12*). Our research, using cytokine signaling as a model system, seeks to advance this field by developing a novel component capable of functioning within biological logical circuits, potentially bridging the gap between traditional computing and cellular decision-making systems.

1.2 Cytokine signaling

Cytokines constitute a group of polypeptides with molecular weights up to 25 kDa that play a crucial role in the communication of multicellular organisms and especially in immunity(*13*). Unlike hormones, cytokines are not stored in glands but are secreted by various cell types, including dendritic cells, macrophages, B cells, and various T cell subsets(*14*). Through these mechanisms, cytokines regulate cellular proliferation, differentiation, and other functions at nano- to picomolar concentrations. They act in autocrine, paracrine, juxtacrine, or endocrine manners by binding to specific receptors. These receptors can be categorized into three groups of transmembrane receptors: receptor tyrosine kinases, receptors with associated kinases, and G-protein coupled receptors(*15*). Consequently, cytokines can exert both anti- and pro-

inflammatory effects, while dysregulation of cytokine function may lead to cancer, autoimmune diseases, or chronic inflammation(*16, 17*). Due to partially high sequence homologies, cytokines exhibit a certain redundancy, enabling different cytokines to elicit similar reactions within the organism(*18*). Cytokines are classified both based on their biological responses (e.g. pro- or anti-inflammatory), and according to their utilized receptors or protein structures. Based on their function, they are classified as, either interferons (IFN), interleukins (IL), chemokines, colony-stimulating factors (CSF), or tumor necrosis factors (TNF)(*18, 19*).

Upon cytokine binding to its specific receptor, intracellular signal transduction is initiated. The receptors themselves are categorized into different classes based on their structural properties: class I and II cytokine receptors, chemokine receptors, receptor tyrosine kinases, receptor serine/threonine kinases, TNF receptors, and IL-1 and IL-17 family receptors(*20*). In class I receptors, which include the IL-6 family, signal transduction primarily occurs via the Janus kinases (JAK)- Signal Transducers and Activators of Transcription (STAT) pathway(*21, 22*).

1.2.1 Gp130 signaling

One of the biggest groups of cytokines is the IL-6 family, which is especially linked to the receptor glycoprotein of 130 kDa (gp130). gp130 is, a versatile transmembrane protein and ubiquitous cytokine receptor critical for immune responses and inflammation, serving as a common beta subunit for multiple cytokine receptors(*23, 24*). While alpha subunits like IL-6Rα, IL-11Rα, and LIFRα provide cytokine-specific binding sites, gp130 functions as the signal-transducing beta component(*25, 26*). Several additional members of the IL-6 family signal through gp130, including oncostatin M (OSM), leukemia inhibitory factor (LIF) ciliary neurotrophic factor (CNTF), cardiotrophin-1 (CT-1), and cardiotrophin-like cytokine (CLC) (*25*). Upon cytokine binding to their respective alpha subunits, gp130 is recruited to form receptor complexes, such as the hexameric (IL-6:IL-6Rα:gp130) complex(*27*). This complex brings gp130 molecules into close proximity, allowing them to activate JAKs. Upon ligand binding, JAKs phosphorylate gp130 on specific tyrosine residues. These phosphorylated residues serve as docking sites for STAT proteins, primarily STAT3, but also STAT1 and STAT5. Activated STAT proteins are phosphorylated and subsequently dimerize and translocate to the nucleus, where they act as transcription factors of target genes involved in various cellular processes, including inflammation, cell proliferation, and survival (*28, 29*).

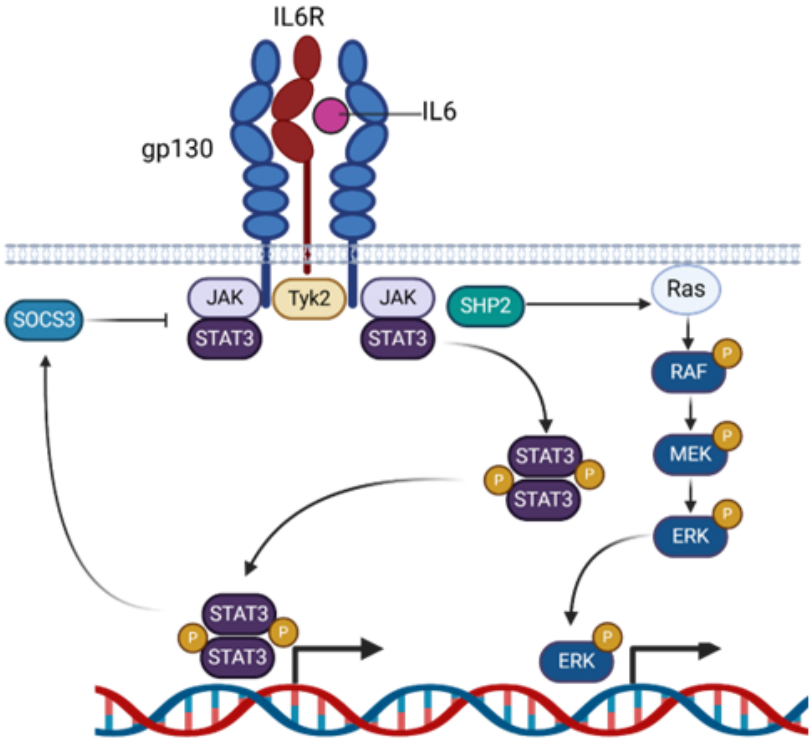

Figure 1: Schematic depiction of IL-6 signaling
The formation of a hexameric complex consisting of two cytokines, α-receptors (IL-6R), and gp130 leads to transphosphorylation of the intracellular JAKs. Shown here with IL-6 (pink), IL-6R (red), and gp130 (blue). These kinases subsequently phosphorylate tyrosines in the intracellular domain (ICD) of gp130, enabling the activation of STAT/MAPK pathways. The adaptor protein SHP2 induces the MAPK pathway, eventually leading to phosphorylated ERK acting as a transcription factor. When phosphorylated, STAT3 forms a homodimer, thereby inducing the transcription of target genes. SOCS3 is one of these target genes, which in turn blocks the activation site of Janus kinases during sustained signal transduction, thereby inhibiting the cascade.To prevent excessive signaling, gp130 signaling is subject to negative regulation. Key players are suppressors of cytokine signaling (SOCS) proteins, they inhibit JAK activity by, for example, binding to phosphorylated receptor sites and blocking STAT protein recruitment(*30*). SOCS3 is a particularly important regulator of IL-6 and IL-11 signaling, as it binds to a specific tyrosine residue on gp130. This mechanism helps maintain cellular homeostasis(*31*).Besides the JAK-STAT pathway, gp130 signaling also activates the MAPK and PI3K pathways. The MAPK pathway is involved in cell proliferation, differentiation, and survival, while the PI3K pathway is implicated in cell survival and metabolism. These pathways are interconnected and can influence each other's activities(*32*). The entire signaling cascade is depicted in Figure 1.

Dysregulation of gp130 signaling has been implicated in various diseases, including autoimmune disorders, cancer, and inflammatory diseases. For instance, elevated IL-6 levels

and hyperactive gp130 signaling have been associated with chronic inflammation and autoimmune diseases(*33*).

As a potential therapeutic target, gp130 offers promising avenues for intervention. Research strategies include blocking cytokine receptors, inhibiting JAKs, and modulating specific signaling components to address various disease mechanisms(*17, 34*).

1.2.2 Fas signaling

The Fas receptor is a critical death receptor, playing a complex role in cellular processes inducing cell death and can be activated on cancer cells through therapeutic approaches(*35*). Its ligand (FasL) is primarily expressed on activated T cells and natural killer cells, existing as a type I transmembrane protein that forms a pre-associated trimer crucial for apoptotic signal transduction(*36*). Through shedding a soluble version can be formed that act's on distant cells(*37*).

The Fas receptor belongs to the TNF superfamily(*38*). While TNF receptors (TNFR1 and TNFR2) are important in cellular signaling, the Fas signaling pathway presents a more direct mechanism of apoptosis. Upon FasL binding, the receptor trimerizes and undergoes a conformational change that facilitates ligand clustering and recruits adapter proteins to form the Death-Inducing Signaling Complex (DISC)(*39*).

The DISC mechanism is particularly interesting, since it contains Pro-Caspase-8, whose spatial proximity directly triggers autoactivation. This unique feature allows for rapid caspase activation, with activated Caspase-8 quickly initiating Pro-Caspase-3 activation and subsequently inducing apoptosis. Unlike TNF receptors, which have multiple potential signaling outcomes, Fas signaling is more streamlined in its cell death induction(*40*). It has however been found that soluble Fas ligand can activate non apoptotic cell survival signaling pathways (*41*). However expression levels of the receptor seems to play pivotal roles in cell fate after signal activation (*42*). The Fas signaling cascade is depticted in **Error! Reference s ource not found.**.

In contrast, TNF receptors (TNFR1 and TNFR2) exist in membrane-bound, juxtacrine, and soluble forms. TNFR1, with its death domain, typically induces cell death and inflammation, while TNFR2 promotes cellular survival. Both can activate the NF-κB signaling pathway, with their mechanism depending on specific protein interactions and ubiquitination processes(*43, 44*).

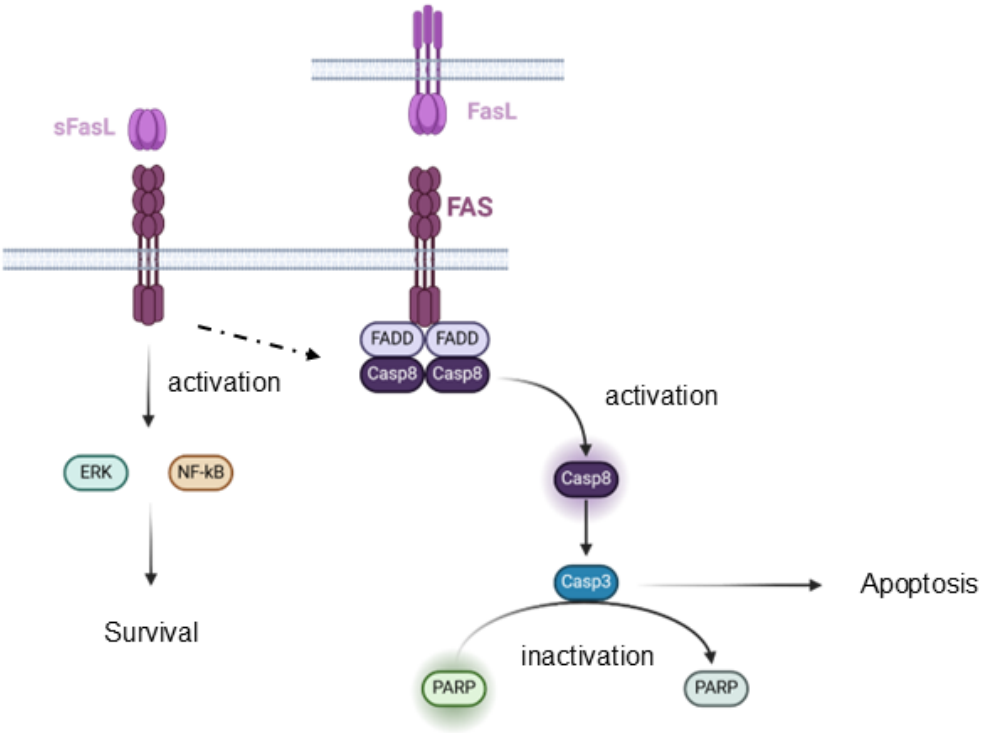

Figure 2: Schematic depicton of Fas signaling.
Soluble FasL (sFasL) can bind to Fas and stimulate cell survival pathways ERK and NF-kB or cause apoptotic cell fate. Upon binding of membrane bound ligand FasL the FasR (purple) forms the DISC complex consisting of FADD and pro-caspase-8. This very streamlined process subsequently leads to the induction of apoptosis and inactivation PARP, an enzyme involved in DNA repair.

The Fas signaling pathway's efficiency lies in its ability to rapidly induce apoptosis through DISC formation, caspase autoactivation, and a highly regulated molecular mechanism. This process makes it a critical component in maintaining cellular homeostasis, immune response, and a potential target therapeutic interventions.

1.3 Synthetic Cytokines

To modulate cytokine signaling several protein fusions or novel proteins have been engineered to prevent off target effects and increase specificity for use in human therapy.

Neoleukin 2/15 represents a breakthrough in computational protein design, offering a novel approach to cytokine-based therapies(*45*). This synthetic molecule recapitulates some aspects of the natural cytokines IL-2 and IL-15 but with a completely unrelated topology and amino acid sequence (Figure 3 A). Neoleukin 2/15 selectively binds and activates IL-2Rβ and the common γ chain, while avoiding interaction with IL-2Rα and IL-15Rα IL. This unique receptor complex specificity results in increased antitumor activity against murine melanoma and colon carcinoma, with reduced toxicity and undetectable immunogenicity. The key advantage of neoleukin-2/15 lies in its ability to expand CD8+ T cells more effectively than regulatory T cells, potentially enhancing antitumor immune responses while minimizing immunosuppressive effects(*46*)

Immunocytokines are engineered proteins that combine the targeting capabilities of antibodies with the immunomodulatory effects of cytokines(*47*). These molecules typically consist of cytokines fused to antibodies, single chain variable fragments (scFvs), single domain antibodies, or peptides that recognize tumor-specific antigens. A wide array of cytokines has been incorporated into immunocytokines, including G-CSF, GM-CSF, interleukins, interferons, and TNF. For example, the immunocytokine F8-IL-2 (Figure 3 B), which fuses IL-2 to an antibody recognizing a cancer-specific fibronectin isoform, has shown promise in targeting IL-2 to tumors and slowing tumor growth in murine melanoma models. Other immunocytokines, such as those based on IL-12 and TNF, are currently in clinical trials for various malignancies. The goal of these fusion proteins is to concentrate cytokine activity in the tumor microenvironment, potentially enhancing therapeutic efficacy while reducing systemic side effects(*48*).

Advances in protein engineering have facilitated the design of multiple synthetic cytokine variants that demonstrate enhanced therapeutic potential.

Fusokines represent an innovative class of engineered proteins that combine two distinct cytokines into a single fusion protein that are strategically designed to achieve synergistic effects by combining pro-inflammatory cytokines with growth factors, thereby enhancing immune responses beyond what individual cytokines could achieve alone. For instance, a

fusokine might combine a pro-inflammatory cytokine with a growth factor to simultaneously activate immune cells and promote their proliferation, leading to a more robust immune response (Figure 3 C). The therapeutic potential of fusokines spans from cancer immunotherapy, where they can boost anti-tumor immunity through enhanced T cell and dendritic cell activation, to the treatment of autoimmune disorders through targeted immunosuppression(*49*).

Cytokine mimetics are engineered molecules designed to mimic the function of natural cytokines and modulate immune responses, offering a high degree of customization. Their modularity allows for precise engineering of antibody architectures, paratope valencies, and receptor binding geometries, enabling the creation of surrogate agonists with tailored biological effects. Thanks to advances in computational biology, it has been shown that cytokine mimetics can induce varied receptor configurations, significantly influencing the strength and bias of downstream signaling. This has significant therapeutic potential, as seen in the development of biased mimetics for type I interferons, which show potent antiviral activity with reduced proinflammatory effects. Similarly, engineered IL-18 mimetics resist inhibition by the natural decoy receptor IL-18BP, offering promise in cancer therapies (Figure 3 D). Additionally, bispecific and multispecific antibody formats allow for the design of cytokine-like functions targeting specific cell populations, paving the way for combining the actions of different cytokines in a single therapeutic entity. Despite the potential for immunogenicity and the need for further development, these cytokine mimetics are poised to enter clinical trials, holding promise for treating diseases like cancer and viral infections with greater specificity and fewer side effects than traditional cytokine therapies(*50, 51*).

Cytokimeras, a class of engineered cytokine fusion proteins, have demonstrated promising results in terms of biological activity and specificity. Cytokines are being engineered through loop swapping where specific receptor-binding loops from one cytokine are genetically exchanged with corresponding loops from another cytokine. Cytokimera are biologically active and like natural cytokines primarily signal through the JAK/STAT and MAPK/ERK pathways. Most Cytokimera do not efficiently trigger the trans-signaling pathway. The new molecules combine receptor-binding properties of their parent molecules, exemplified by GIL-11, which incorporates loops from IL-11 and LIF to interact with a unique receptor complex comprising gp130, IL-11Rα, and LIFR (*52*) (Figure 3 E). Through precise loop exchanges, researchers can effectively alter receptor specificity and create molecules with novel signaling capabilities,

opening new possibilities for therapeutic applications. One cytokimera, IC7-Fc, has been shown to improves glucose tolerance, prevents weight gain and liver steatosis in obese mice, proving the therapeutic potential of this approach (*53*).

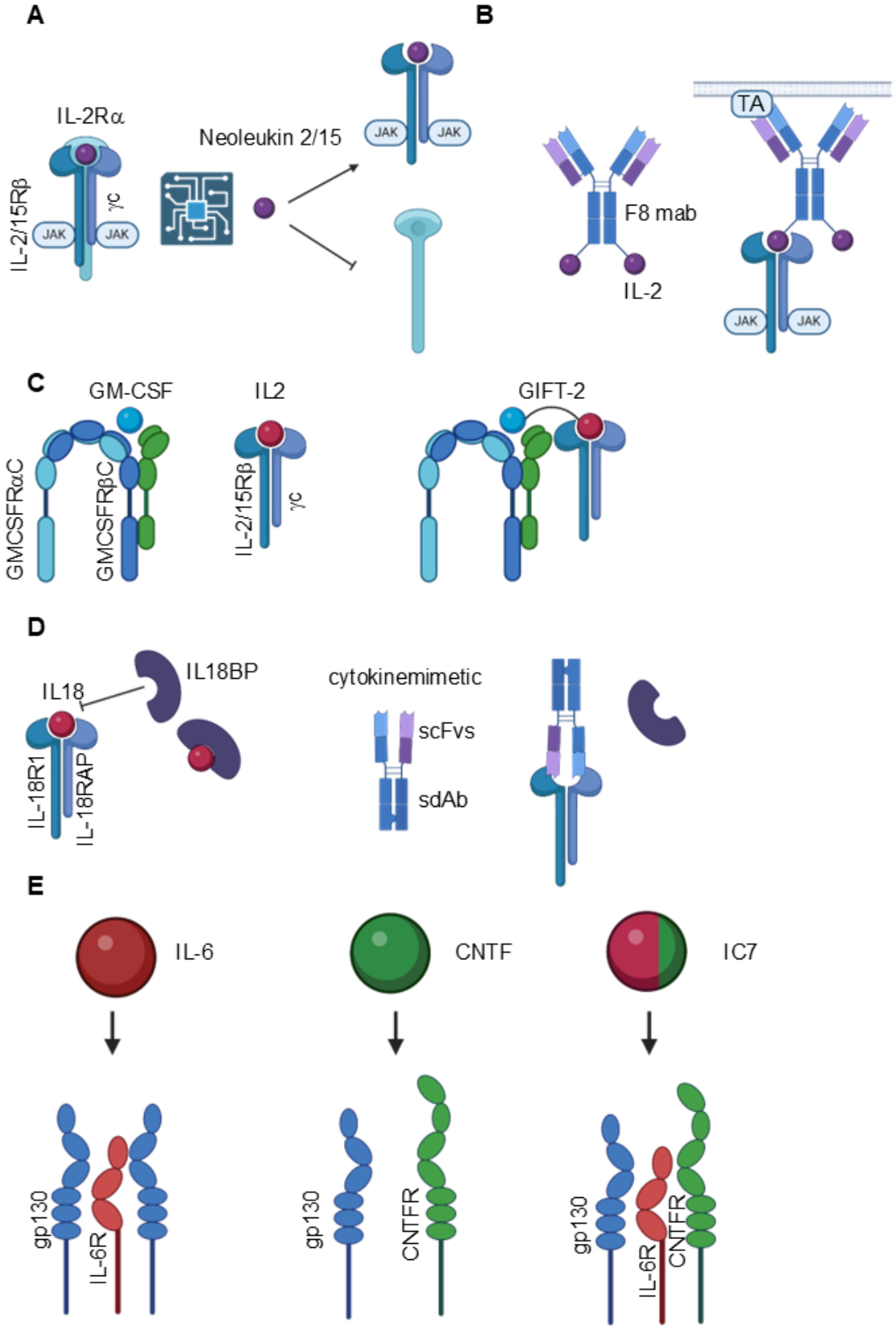

Figure 3: Overview of engineered cytokine-based therapeutic strategies.
(A) Neoleukin-2/15 engineering: Comparison of natural IL-2 signaling, which requires binding to IL-2Rα (CD25), IL-2Rβ, and common gamma chain (γc), with the AI-designed Neoleukin-2/15. This synthetic protein selectively engages only IL-2Rβ and γc to initiate signaling, bypassing IL-2Rα dependency. (B) Immunocytokine design using the F8 antibody: IL-2 is

conjugated to the F8 monoclonal antibody, enabling targeted delivery to the tumor microenvironment where it can activate local IL-2 signaling pathways. (C) Fusokine engineering exemplified by GIFT-2: A genetic fusion of GM-CSF and IL-2 creates a bifunctional cytokine that enhances downstream signaling of both parent cytokines specifically in cells expressing both receptor types. (D) Cytokine mimetic development: Natural IL-18 signaling requires binding to both IL-18R1 and IL-18RAP, and can be inhibited by IL-18BP. The engineered bispecific seedbody (sdAb) contains two different single-chain variable fragments (scFvs) targeting IL-18R1 and IL-18RAP, enabling IL-18-like signaling while being resistant to IL-18BP inhibition. (E) Cytokimera design: Comparison of natural IL-6 and CNTF signaling pathways, where IL-6 engages IL-6R and gp130, while CNTF binds to gp130 and CNTFR. The engineered Cytokimera IC7 incorporates specific loops from CNTF into the IL-6 scaffold, creating a chimeric cytokine capable of binding gp130, IL-6R, and CNTFR simultaneously, thereby achieving enhanced cell-type specificity through multi-receptor engagement.

Antibody engineering

The humoral immune response plays a critical role in immunity, with antibodies undergoing affinity maturation to produce higher affinity variants during infection or vaccination(*54*). Antibodies, also known as immunoglobulins, are crucial components of the adaptive immune system, providing highly specific defense against pathogens. Produced by B lymphocytes (B cells), antibodies circulate in the blood and other fluids(*55*). Each antibody is designed to recognize and bind to a specific antigen, a molecule found on the surface of pathogens like bacteria, viruses, and parasitesThis binding can neutralize the pathogen directly by blocking its ability to infect cells, or it can mark the pathogen for destruction by other immune cells, such as phagocytes or natural killer cells(*56*).. The remarkable diversity of antibodies generated through gene rearrangement and somatic hypermutation allows the adaptive immune system to recognize and respond to a vast array of foreign invaders, providing long-lasting immunity(*57*).

Monoclonal antibodies (mAbs) are often selected for their high affinity through technologies like hybridoma, antibody display platforms, and direct sequencing(*58*). The development of antibodies and antibody-derived macromolecules for therapeutic use requires advanced protein engineering, drawing on detailed knowledge of protein structure and function. This understanding has been shaped by crystallographic studies of antibodies, which began in the 1970s. Currently, the Protein Data Bank (PDB) contains over 3,500 antibody fragment structures, providing insights into their interactions with various molecules. Antibodies are Y-shaped proteins composed of two identical light and two identical heavy chains, which are linked through disulfide bonds. Human light chains (κ or λ) consist of a constant and a variable domain, while heavy chains can belong to one of five isotypes (IgA, IgD, IgE, IgG, or IgM), each playing distinct roles in the immune system(*59, 60*).

The IgG isotype is a monomer formed from heavy-light chain pairs, while IgA and IgM can form dimers or pentamers due to the presence of a J-chain(*61*). These structural features are being exploited through engineering techniques like antibody humanization, affinity modulation, and stability enhancement. Such methods aim to fine-tune the functional and biophysical properties of antibodies, optimizing them for specific therapeutic applications and improving efficacy, stability, and manufacturability(*62*).

Human IgG1 (Figure 4 A) and IgG3 (Figure 4 C) are potent activators of immune pathways due to their strong binding affinity to both C1q of the complement system and FcγR family proteins. In contrast, IgG2 (Figure 4 B) and IgG4 (Figure 4 D) are weaker immune activators, stemming from their lower affinity for these immune mediators, especially IgG2 has no affinity for FcγRI(*63, 64*).

Interestingly, the IgG2 isotype features a short hinge region (12 amino acids) with four disulfide bonds, which restricts the Fab arms' conformational flexibility relative to the Fc portion. IgG2 exists in three major conformational states: IgG2A which is Y-shaped, with independent Fab disulfide bonds, IgG2B can be imagined T-shaped, with Fab arms covalently linked to the hinge, and IgG2A/B being a hybrid form with one independent and one linked Fab arm. The compact IgG2B conformation particularly enhances receptor engagement in allosteric agonist antibodies(*65*). This disulfide switching, which affects antibody flexibility and clustering, occurs independently of Fcγ receptor engagement, challenging the traditional view that Fc regions are essential for immune activation(*66, 67*). These findings open new possibilities for engineering mAbs by targeting the hinge region to enhance therapeutic efficacy, especially in immunostimulatory applications. This has been extensively studied by creation of artificial variants of IgG2 backbone with mutations of cysteins in the hinge region leading to increased rigidity in the hinge region. Functionally these mutations exert higher agonism of antibodies with increasing rigidity in the hinge region(*68, 69*).

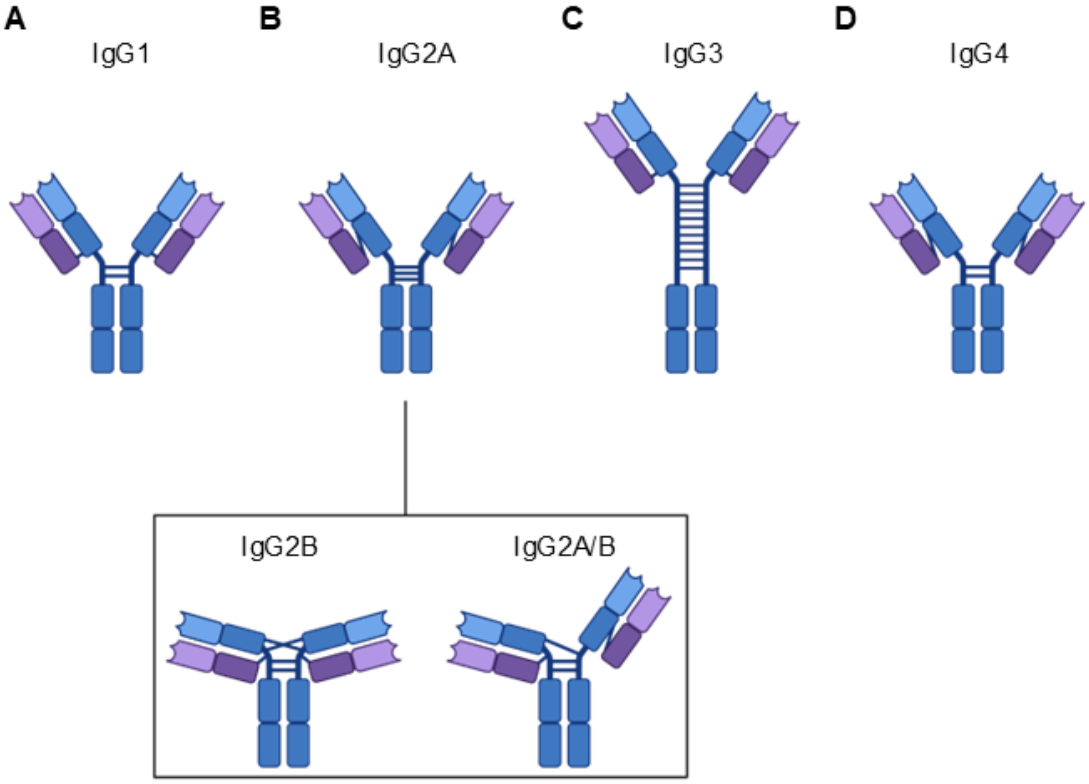

Figure 4: Structural comparison of human IgG antibody subclasses highlighting distinct disulfide bond patterns.
The light chain is always depicted in purple while heavy chains are always in blue. (A) IgG1 structure featuring two disulfide bonds in the hinge region. (B) IgG2 variants: The predominant IgG2A form contains three disulfide bonds in the hinge region and one connecting the heavy and light chains. Inset shows the T-shaped IgG2B variant characterized by two disulfide bonds in the hinge region and two additional bonds between the hinge-CH1 and CL domains. Also depicted is the IgG2A/B hybrid form combining structural elements of both variants. (C) IgG3 structure distinguished by an elongated hinge region containing 11 disulfide bonds. (D) IgG4 configuration showing two disulfide bonds in the hinge region and two unique inter-chain disulfide bonds formed between distant cysteine residues of the heavy and light chains. Disulfide bonds are represented as connecting lines between protein domains.

Since antibodies have been purified for the first time they have become powerful tools in modern medicine, revolutionizing the treatment of a wide range of diseases. Their inherent ability to specifically recognize and bind to targets has been harnessed to develop various therapeutic strategies. mAbs are a major therapeutic tool, accounting for around 80% of therapeutic biologics. By may 2021, the Food and Drug Administration (FDA) had approved around 100 mAb drugs, owing to their ability to bind diverse targets with high specificity and trigger immune effector functions(*70*). Being produced in the lab to target a single epitope, they are widely used to treat cancer by directly inducing cancer cell death, blocking tumor growth signals, or enhancing immune responses against tumors(*71*). In autoimmune diseases, antibodies can neutralize pro-inflammatory cytokines or deplete autoreactive immune cells(*72*).

They are also employed to prevent transplant rejection, treat infectious diseases by neutralizing pathogens, and deliver targeted therapies by conjugating them to drugs or toxins(*73, 74*). The versatility and specificity of antibodies continue to drive innovation in therapeutic development, offering increasingly effective and targeted treatments for numerous conditions.

Antibodies are no longer merely raised but are now extensively engineered. Early antibody engineering efforts focused on humanizing mouse or rabbit antibodies(*75*). Today, antibody development has advanced far beyond this, employing a wide range of innovative approaches. While mAbs are highly effective therapeutic agents, their utility is constrained by their ability to target only a single antigen, despite many complex diseases involving multiple factors. Bispecific antibodies (bsAbs) overcome this limitation by possessing two antigen-binding sites, allowing them to engage with distinct epitopes on the same or different antigens(*76*). A key mechanism of bsAbs is the redirection of T cells to tumors, as exemplified by T cell engagers that simultaneously target tumor antigens and cluster of differentiation 3 (CD3) on T cells, thereby facilitating tumor cell destruction. Clinically successful bsAbs include Catumaxomab and Blinatumomab for cancer treatment, as well as Emicizumab, approved for hemophilia A, which mimics the activity of clotting factor VIII(*76-78*).

Around 30 bsAb-based drugs are currently in clinical trials, with another 60 in preclinical development. They are being explored for various therapeutic strategies, such as dual pathway inhibition. For instance, Roche's Duligotzumab targets Epidermal Growth Factor Receptor (EGFR) and human epidermal growth factor receptor 3 (HER3) to address resistance in cancers like colorectal and head and neck cancer. Another bsAb, Merrimack Pharmaceuticals' MM-111, targets Her2 and Her3 to enhance tumor response. Additionally, bsAbs like CrossMab RG7221, which targets VEGF-A and Ang-2, are used to inhibit tumor angiogenesis. In the field of immunology, bsAbs like M1095/ALX-07613 neutralize cytokines (IL-17A and IL-17F) for treating inflammatory diseases(*79*).

Many therapeutic antibodies, particularly those used for antiviral and anticancer treatments, belong to the IgG1 subclass due to their potent immune-activating properties. Examples include Palivizumab, an FDA-approved humanized IgG1 monoclonal antibody designed to target the respiratory syncytial virus (RSV). On the other hand, IgG2 antibodies are less effective at activating complement but are often used in cases where a more subdued immune response is desired(*63*). IgG2 antibodies are commonly applied in therapies targeting cellular receptors involved in inflammation or cancer(*67*). The first IgG2 antibody to receive food and drug

administration (FDA) approval was Panitumumab in 2006, targeting the epidermal growth factor receptor (EGFR) for cancer treatment. More recently, Nemolizumab, an IL-31 receptor alpha blocker, was approved in 2024 to treat pruritic conditions(*80, 81*).

While conventional mAbs target pathogens or tumor cells and rely on Fc-mediated immune responses, a distinct class of mAbs, called agonistic antibodies, target immune receptors like TNFRs (e.g., CD40, 4-1BB) to trigger intracellular signaling. Notably, antibodies targeting immune receptors, such as CD40, can mimic natural ligands and trigger immune responses, as seen with anti-CD40 antibodies for cancer treatment(*67*). These agonistic mAbs are complex, with their activity depending on factors like epitope, isotype, and Fcγ receptor interaction. Although they hold promise for cancer immunotherapy, the role of affinity in their function has not been systematically studied, leaving it unclear if high affinity is as critical for their efficacy as it is for direct-targeting antibodies(*69*).

Palivizumab, an IgG1 antibody, stands out as a therapeutic agent developed to prevent infection and severe disease caused by respiratory syncytial virus (RSV), particularly in infants at high risk. Approved by the FDA in 1998, Palivizumab specifically binds to an epitope on the fusion (F) protein of RSV, blocking the virus from entering host cells and preventing infection(*82*). This monoclonal antibody has become a critical tool in reducing the incidence of severe RSV-related respiratory diseases in vulnerable populations(*83*). While other FDA and European Medicines Agency (EMA)-approved antibodies, such as Tocilizumab (anti-IL-6R)(*84*), Infliximab (anti-TNF)(*85*), and Ipilimumab (anti-cytotoxic T-lymphocyte-associated Protein 4 (CTLA-4))(*86*), are effective in treating inflammatory and cancerous conditions, they target human proteins, making them unsuitable for targeting viral antigens. In contrast, Palivizumab, along with other antiviral monoclonal antibodies like Nirsevimab (also targeting RSV)(*87*), Sotrovimab (targeting Severe acute respiratory syndrome coronavirus 2)(*83*), and Ansuvimab (targeting Ebolavirus)(*88*), specifically bind to foreign viral proteins, providing highly targeted immune protection against these pathogens.

1.4 Nanobodies and anti-idiotypes

Nanobodies are a unique class of antibody derived from Camelidae heavy chain antibodies(*89*). These small, single-domain antibodies have gained significant attention in the field of biomedical research and therapeutic development due to their exceptional properties. Nanobodies are known for their small size, high stability, and low immunogenicity, making them ideal candidates for various biomedical applications(*90*). Their ability to penetrate tissues

and recognize unique epitopes that are often inaccessible to conventional antibodies further enhances their therapeutic potential(*91*).

In cancer therapy, nanobodies can be employed for targeted delivery of cytotoxic agents or radioisotopes to tumor cells by binding specific antigens, such as HER2 in breast cancer, while engineered nanobodies in immuno-oncology enhance anti-tumor immunity by blocking immune checkpoints like PD-1 and CTLA-4 or engaging T cells to destroy tumor cells(*92-94*). In inflammatory and autoimmune diseases, nanobodies show potential by neutralizing pro-inflammatory mediators such as TNF, offering therapeutic benefits in conditions like rheumatoid arthritis and inflammatory bowel disease(*95*). In infectious diseases, nanobodies can disrupt viral or bacterial functions or prevent their entry into host cells, as demonstrated by nanobodies targeting the SARS-CoV-2 spike protein for potential antiviral therapy(*96*). The ability of some naturally occurring VHHs, by means of receptor-mediated transcytosis, or other VHH by using liposomes in carrier-mediated transcytosis to cross the blood-brain barrier makes nanobodies attractive for neurological applications, such as targeting amyloid-beta in Alzheimer's disease(*97, 98*). Furthermore, the FDA- and EMA-approved nanobody Caplacizumab (Cablivi), which targets von Willebrand factor, has demonstrated efficacy in treating acquired thrombotic thrombocytopenic purpura, a rare and life-threatening blood clotting disorder(*99*). Collectively, these applications highlight the versatility and therapeutic promise of nanobodies in precision medicine and drug development.

One particularly interesting subclass of nanobodies are anti-idiotypic nanobodies. These specialized nanobodies are designed to bind specifically to the variable regions or hypervariable loops of other antibodies, effectively mimicking the original antigen or blocking the antibody's activity(*100*). This unique property makes anti-idiotypic nanobodies potentially powerful tools in immunomodulation and targeted therapy, however few were used in research and none entered clinical studies to date.

1.5 Synthetic Receptors

Synthetic biology has made significant strides in engineering artificial cellular receptors, enabling precise control over cellular responses to specific stimuli. Various types of engineered receptors were developed each with unique mechanisms and for different applications. The different synthetic receptors discussed here are summarized in Figure 5.

Modular Extracellular Sensor Architecture (MESA) receptors offer an alternative approach to antigen-mediated signaling. These receptors consist of multiple chains extracellularly binding the same ligand or antigen, one of them contains a proteinase, the other a cleavable protein sequence followed by a transcription factor intracellularly. Antigen-mediated dimerization of MESA receptor chains increases the probability of transcription factor cleavage. The cleaved transcription factor then moves to the nucleus to activate transgene expression. MESA receptors can be used to create cells with programmable responses to specific antigens, useful in cell-based therapies and synthetic biology circuits(*101*).

Generalized Extracellular Molecule Sensors (GEMS) represent another class of synthetic receptors, engineered for remarkable versatility in sensing and signaling. These adaptable molecular devices can be tailored to recognize a wide spectrum of inputs, from tumor markers to common dietary molecules, and trigger specific cellular responses by activating multiple endogenous signaling pathways. The design flexibility of GEMS allows for their application across diverse fields, including cancer diagnostics, environmental monitoring, and the creation of intricate synthetic cellular circuits. For instance, GEMS have been applied to sense caffeine in the Caffeine-Stimulated Therapeutic Activation Response (C-STAR) system, which showcases the potential of these receptors in therapeutic interventions. In this approach, GEMS are equipped with caffeine-specific antibody chains, effectively repurposing a common stimulant into a powerful tool for controlled protein expression. The C-STAR system has been applied experimentally in diabetes treatment, where caffeine consumption triggers the production of glucagon-like peptide-1 (GLP-1), a crucial hormone in blood sugar regulation. This represents a novel-approach in drug administration, where a ubiquitous dietary component becomes the key to unlocking targeted therapeutic effects(*102, 103*).

Chimeric cytokine receptors combine components from different cytokine receptor systems to create novel signaling properties. One example is a receptor with the extracellular domain (ECD) of IL-4R fused to the intracellular domain (ICD) of IL-7R. This chimeric receptor heterodimerizes with endogenous IL-2Rγ in response to IL-4 but activates IL-7-specific signaling pathways. Another example involves the ECD of IL-6R fused to the ICD of Vascular Endothelial Growth Factor Receptor (VEGFR). This receptor activates VEGFR-specific Ca^{2+} signaling in response to IL-6. An advanced feature of this system translates polar differences in intracellular Ca^{2+} into directed cell migration via an engineered RhoA GTPase. These approaches allow reprogramming of cellular responses to specific cytokines, potentially useful

in immunotherapy and controlling cell migration in tissue engineering and regenerative medicine(*104*).

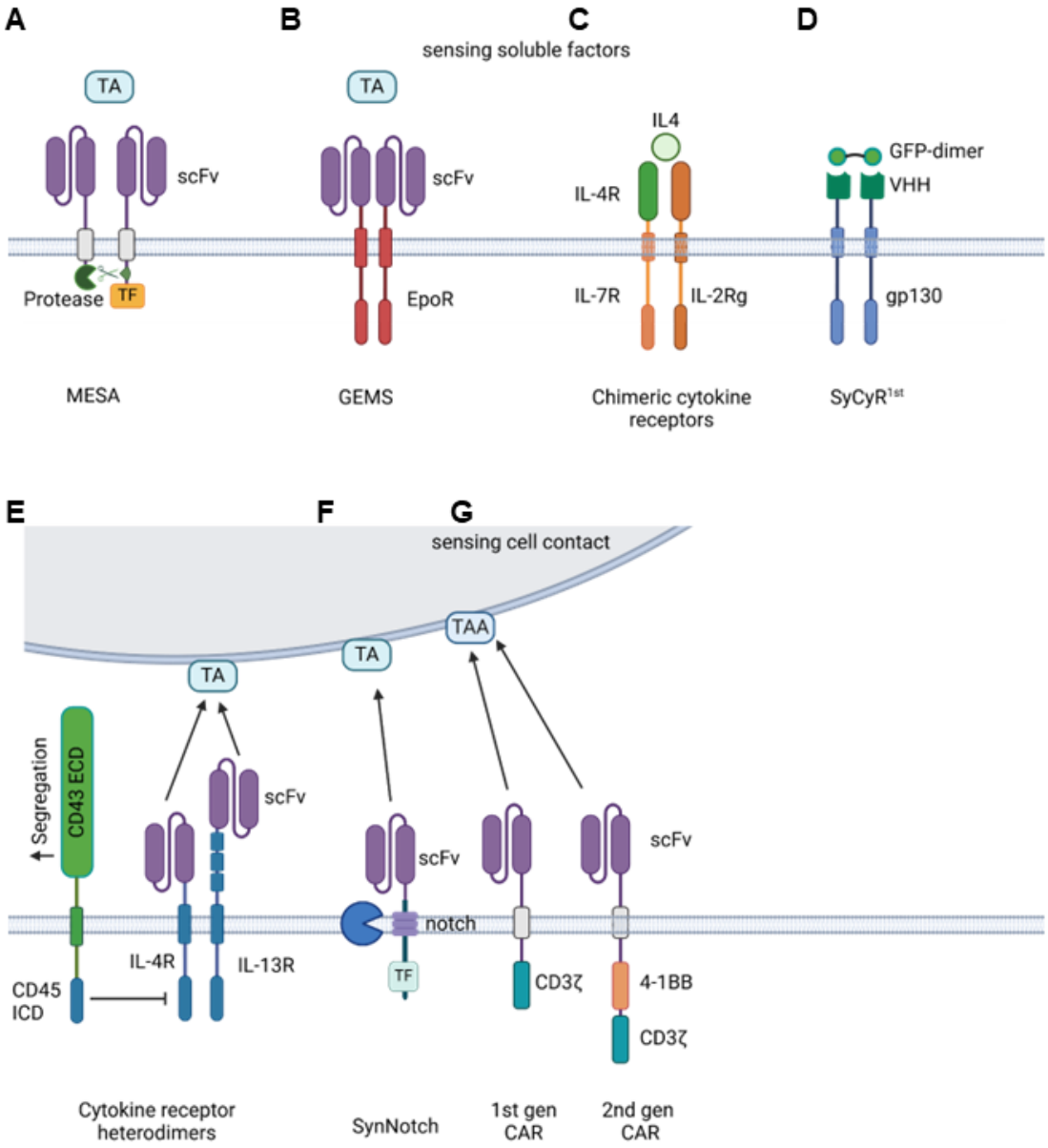

Figure 5: Depicted is a selection of mammalian synthetic receptors.

These receptors respond to two primary categories of inputs: soluble extracellular targets (A-D) and surface-bound antigens (E-G). Soluble target detection systems include: (A) MESA receptors, where antigen-mediated dimerization enhances transcription factor cleavage and subsequent nuclear translocation for transgene activation. (B) GEMS (Generalized Extracellular Molecule Sensor) receptors that detect specific target antigens and activate endogenous signaling pathways, illustrated here with Epo signaling. (C) Chimeric cytokine receptors combining IL-4R extracellular domains with IL-7R intracellular domains, which heterodimerize with endogenous IL-2rγ upon IL-4 binding to trigger IL-7-specific signaling. (D) Synthetic Cytokine Receptors (SyCyRs) that respond to non-endogenous ligands (e.g., dimeric GFP) to initiate endogenous cytokine signaling, shown here activating gp130-mediated STAT3 signaling. Surface-bound antigen detection systems include: (E) Engineered IL-4R/IL-

13R heterodimers that enable cell-contact-dependent signaling. Target recognition via scFv binding reduces intercellular distance, segregating the CD43 extracellular domain (fused to inhibitory CD45 intracellular domain) from the interface, thereby restoring cytokine signaling. (F) SynNotch receptors, which utilize (single chain variable fragment) scFv-mediated binding to release membrane-tethered transcription factors upon binding to the target antigen (TA), enabling targeted gene expression. (G) Chimeric Antigen Receptors (CARs) that activate T cell responses through CD4ζ signaling cascades upon target recognition via scFv against the tumor associated antigen (TAA). Evolution from first-generation CARs (CD4ζ-ECD only) to second-generation incorporating costimulatory domains e.g., 4-1BB-ICD shown or CD28-ICD has improved T cell activation against cancer markers. Figure adapted from (*103, 105*).

Synthetic Cytokine Receptors (SyCyRs) represent an innovative class of engineered cellular receptors designed to respond specifically to non-endogenous ligands, such as dimeric Green Fluorescent Protein (GFP). These receptors enable cell specific control over cytokine signaling pathways by initiating endogenous signaling cascades upon activation. The mechanism and different variants of SyCyRs will be thoroughly examined in paragraph 1.7.

Engineered cytokine receptor heterodimers exploit cell-contact-dependent signaling to achieve localized activation. The system comprises engineered interleukin-4 receptor (IL-4R) and interleukin-13 receptor (IL-13R) heterodimers, combined with a CD43-CD45 inhibitory system. The mechanism involves scFv-mediated binding to a membrane-displayed target, which brings the sender and receiver cells into close proximity. This close contact excludes the bulky extracellular domain (ECD) of CD43 from the cell-cell interface. The CD43 ECD is fused to the inhibitory intracellular domain (ICD) of CD45. Segregation of CD45 domains from the receptor dimers restores cytokine signaling. This system allows for highly localized activation of cytokine signaling, reducing off-target effects(*106*).

Synthetic Notch (SynNotch) receptors are modular synthetic receptors inspired by the natural Notch signaling pathway. These receptors consist of an extracellular scFv domain, a Notch core, and an intracellular transcription factor. When the scFv binds to its target antigen, the receptor undergoes a conformational change, leading to the intramembrane-cleavage by gamma-secretase and release of the ICD, comprising the custom transcription factor. This liberated transcription factor then translocates to the nucleus, where it activates specific transgene expression. SynNotch receptors can be used to engineer cells with customized input-output relationships, enabling novel cellular therapies and biosensors(*107*).

Therapeutically most important are engineered receptors that combine the specificity of antibodies with the signaling capacity of T cells called Chimeric Antigen Receptors (CARs).

These receptors comprise an extracellular single-chain variable fragment (scFv) derived from an antibody, linked to intracellular signaling domains. Upon binding to a specific antigen on a target cell, CARs activate endogenous signaling cascades that trigger T cell responses. The intracellular domains (ICDs) are engineered to ensure effective T cell activation in response to cancer markers. CAR-T cell therapy has shown remarkable success in treating certain types of blood cancers, representing a significant breakthrough in immunotherapy(*108-110*).

1.6 Synthetic Cytokine Receptors

Synthetic cytokine receptors (SyCyRs) represent a powerful tool in synthetic biology, enabling precise control over cellular signaling pathways. First-generation SyCyRs ($SyCyR^{1st}$) feature a modular architecture comprising two key components: nanobody-based receptors and their corresponding soluble protein dimers as ligands. The receptor component integrates extracellular nanobodies—single-domain antibody fragments derived from Camelidae heavy-chain antibodies—that recognize specific epitopes such as GFP and mCherry, fused to the transmembrane and intracellular domains of target receptors.

The versatility of this system has been demonstrated through successful integration with various transmembrane, and intracellular signaling domains, including those derived from TNF(*111*), Fas(*111*), gp130(*112*), IFNAR(*113*), IL-12Rβ1(*114*), and IL-23(*14*) receptors. Constitutively active receptors with a PPCL motif in their trans-membrane region have also been developed(*115*). The ability to force dimerization of receptors that are usually not interacting leads to new activation patterns of the phosphoproteome and can be used as a research tool.

The juxtamembrane region, or stalk, plays a critical role in determining signaling output by influencing receptor dimerization, orientation, endosomal internalization, and accessibility of intracellular signaling motifs(*116, 117*). Nanobodies demonstrate favorable immunological profiles due to their high sequence identity to the human antibody heavy chain, making them safer for therapeutic applications compared to alternative approaches like GEMS(*102*).

By understanding the interplay between the stalk region, binding angles of synthetic ligands to nanobodies, and the synthetic ligands themselves in receptor signaling, novel synthetic receptors with tailored properties can be designed. This enables precise control over signaling strength and downstream pathways, opening new possibilities for diverse biomedical applications.

1.7 CAR-T cell therapy

CAR-T cell therapy represents a groundbreaking advancement in cancer immunotherapy, leveraging synthetic receptor biology to create highly targeted and potent anti-tumor responses. This innovative approach, first approved by the U.S. Food and Drug Administration (FDA) in 2017, making it the first approved cell gene therapy, has shown remarkable success in treating certain types of blood cancers, particularly refractory or relapsed B cell precursor acute lymphoblastic leukemia (ALL) and diffuse large B cell lymphoma (DLBCL) (*108-110*).

The process of CAR-T therapy involves collecting a patient's T cells, genetically modifying them to express the CAR, expanding these cells in vitro, and then reinfusing them back into the patient. Once in the body, these engineered T cells can recognize and bind to their target antigen on cancer cells, triggering T cell activation, proliferation, and cytotoxic activity against the tumor(*118*).

At its core, CAR-T cell therapy involves genetically modifying a patient's own T cells to express chimeric antigen receptors. These CARs are designed synthetic receptors composed of an extracellular scFv antibody, or a VHH that recognizes a specific tumor antigen, commonly CD19 or BCMA for B cell malignancies(*119, 120*). A hinge region, a transmembrane domain, and intracellular signaling domains derived from T cell activation pathways(*121-123*). The intracellular portion typically includes the CD3ζ chain of T cell receptors coupled with one costimulatory domain in second generation CARs such as 4-1BB(*124*) or CD28(*125*) in FDA approved CAR-T cells. In experimental third generation CAR-T cells a second costimulatory domains such as CD27(*126*), ICOS (*127*), or OX40(*128*) is fused to the ICD, enhancing T cell activation and persistence

While CAR-T cell therapy has shown unprecedented success in certain hematological malignancies, researchers are working to overcome challenges related to efficacy in solid tumors, off-tumor toxicities, and long-term persistence of CAR-T cells. On-target, off-tumor effects like B-cell aplasia in CD19-targeted therapies, macrophage activation syndrome, and tumor lysis syndrome require careful monitoring and management (*129*). Recent developments are exploring the integration of constitutively active cytokine receptors or precise control mechanisms like the incorporation of STAT3 activation to enhance effector functions or create more nuanced "On/Off" switches for T cell activation (*130-132*).

Another important drawback is exhaustion which occurs as CAR-T cells face overwhelming tumor burden or hostile microenvironmental conditions especially in solid tumors. This state of exhaustion manifests through multiple functional deficits that severely compromise therapeutic efficacy. The exhausted CAR-T cells exhibit markedly reduced proliferative capacity, limiting their ability to expand in response to tumor antigens. Additionally, their cytotoxic functions become impaired, resulting in diminished tumor cell elimination (*133*).

The development of new fourth generation CAR-T cells (also known as TRUCK T cells or armored CARs) are being developed with the ability to produce inflammatory cytokines like IL-12 or IL-18, enhancing their anti-tumor activity and the recruitment of innate immune cells to the tumor microenvironment attempting to act on solid tumors overcoming the challenges that the tumor microenvironment of solid tumors imposes. A first clinical trial for recurrent ovarian cancer has been started (*134*).

Universal "off-the-shelf" allogenic CAR-T cells derived from healthy donors are being developed. Here CRISPR-Cas9 gene editing is being used to remove the endogenous T cell receptor and minimize graft-versus-host disease risk by creating allogeneic CAR-T cells (*135*).

Improved production methods utilizing automated closed systems, like the CliniMACS® prodigy and optimized culture conditions are being developed and are widely used in clinics to reduce manufacturing time and costs while improving product consistency and quality (*136*).

As research in this field continues to evolve, CAR-T cell therapy and related synthetic receptor approaches are poised to revolutionize cancer treatment, potentially offering new hope for patients with previously intractable malignancies and opening doors to novel therapeutic strategies across a broad spectrum of diseases. These advances are supported by growing clinical evidence and an expanding pipeline of CAR-T cell products in development, with over 1000 clinical trials currently registered worldwide (*137*).

2 Aims

This thesis aims to enhance the therapeutic potential of synthetic cytokine receptors (SyCyRs) by addressing key limitations in their current design. Conventional SyCyR^{1st} systems rely on fluorescent proteins, like GFP or mCherry as ligands, which present significant immunogenicity concerns that hinder their clinical application. To overcome these constraints, we developed a novel approach centered on Palivizumab, an FDA-approved antibody targeting respiratory syncytial virus proteins to generate the next generation of SyCyRs called SyCyR^{2nd}.

Palivizumab represents an optimal choice due to its unique combination of properties. The antibody lacks endogenous human targets, effectively preventing off-target effects in therapeutic applications. Furthermore, it possesses a well-established safety profile with minimal immunogenicity, a crucial factor for clinical implementation. Its existing FDA approval status provides an additional advantage for potential therapeutic translation.

Our research strategy focused on comprehensive modifications to the SyCyR platform. The primary innovation involved characterization and integration of a newly generated anti-idiotypic nanobody against Palivizumab into the receptor's extracellular binding domain marking the development of SyCyR^{2nd}. We then conducted systematic modifications of the juxtamembrane region to optimize signal transduction. The antibody itself underwent extensive structural engineering, including conversion to single-chain variable fragments (scFvs), integration of Fc tags with varying lengths, and transformation from IgG1 to IgG2 subtype which eventually led to the generation of SyCyR^{3rd}.

These deliberate structural and functional modifications were systematically investigated to determine the optimal configuration for therapeutic applications, with particular emphasis on signal strength, specificity, and stability. Our comprehensive approach aimed to establish a clinically viable SyCyR platform that combines robust signaling capabilities with favorable immunological properties.

3 Materials and Methods

3.1 Material

3.1.1 Consumables

Consumables used in the study are listed in Table 1 below.

Table 1: Consumables

Name	Manufacturer
15 ml reaction tube	Greiner Bio-one
50 ml reaction tube	Greiner Bio-one
1.5 ml reaction tube (SafeSeal tube)	Sarstedt AG & Co.KG
2 ml reaction tube (SafeSeal tube)	Sarstedt AG & Co.KG
Sterile petri dish (10 cm)	Greiner bio-one
T75 cell culture flask (filter)	Sarstedt AG & Co.KG
T175 cell culture flask (filter)	Sarstedt AG & Co.KG
Countess cell counting chamber slide	Peqlab
1.5 ml cryotube	VWR
Mr. Frosty™ freezing container	Thermo Scientific
6-well plate CytoOne®	Starlab
Microtest Plate 96-well	Sarstedt AG & Co.KG
Nitrile gloves	Ansell
Eppendorf pipette research plus gray (2.5 µl)	Eppendorf
Eppendorf pipette research plus gray (10 µl)	Eppendorf
Eppendorf pipette research plus yellow (20 µl)	Eppendorf
Eppendorf pipette research plus yellow (200 µl)	Eppendorf
Eppendorf pipette blue research plus (1000 µl)	Eppendorf
Pipette tips	Starlab
Serological pipettes	Hirschmann
Rotilabo® syringe filter, PVDF, sterile 0.22 µm	Carl Roth GmbH
Rotilabo® syringe filter, PVDF, sterile 0.45 µm	Carl Roth GmbH
20 ml syringe Omnifix®	Braun
Amicon ultra-15 centrifugal filter unit	Merck
NAP™-25 columns Sephadex™	Cytiva
Strep-Tactin® XT 4 Flow®	IBA Lifsciences GmBH
HiTrap MabSelect PrismA®	Cytiva
Whatman paper	VWR
Nitrocellulose membrane	Cytiva
Sensor chip protein A	Cytiva
Syringes 1ml Ominfix® 100 solo	B. Braun

3.1.2 Chemicals

All chemicals used in this study can be found in table 2.

Table 2: Chemicals

Name	Company
Mili-Q® dest. H2O	Merck
Bovine serum albumin (BSA)	Thermo Fisher Scientific
Ethanol (70%, 99%) (v/v)	Sigma-Aldrich
2-Propanol (Isopropanol)	AppliChem GmbH
Acrylamide	Carl Roth
Agar-agar	Carl Roth
Agarose	Biozym Scientific GmbH
Ammonium peroxodisulfate (APS)	Sigma-Aldrich
GeneRuler Express® (DNA Ladder 100-5000 bp)	Thermo Scientific
Glycerin	Roth
Glycine	Merck
β-Mercaptoethanol	Sigma-Aldrich
Sodium dodecyl sulfate (SDS)	Roth
Tetramethylethylenediamine (TEMED)	Sigma-Aldrich
Tris	Bethesda Research Laboratories
Triton X-100	Sigma-Aldrich
Turbofect™ Transfection Reagent	Thermo Scientific
Tween 20	Sigma-Aldrich
Complete protease inhibitor	Roche
HD-Green®	INTAS
Potassium acetate	Merck
Potassium dihydrogen phosphate (KH2PO4)	Merck
Sodium orthovanadate (Na3VO4)	Merck
Sodium citrate	Sigma-Aldrich
NP-40	Sigma-Aldrich
PageRuler™ prestained protein ladder	Thermo Fisher Scientific

3.1.3 Antibiotics

Antibiotics used for cloning and cell-culture are listed in table 3.

Table 3: Antibiotics

Name and Stock Concentration	Company
Ampicillin, 100 mg/ml	Carl Roth
Hygromycin B, 100 mg/ml	Carl Roth
Penicillin/streptomycin, 10.000 U	Genaxxon
Puromycin, 1 mg/ml	Carl Roth

3.1.4 Material for Cell culture

Solutions, buffers and media used for cell-culture are listed in table 4 below.

Table 4: Material for cellculture

Name	Company
DMEM	Life Technologies
Fetal bovine serum (FBS)	Gibco, Thermo Scientific
Penicillin/streptomycin	Genaxxon Bioscience
Expi293F Medium	Thermo Scientific
ExpiCHO-S Medium	Thermo Scientific
Dimethylsulfoxide (DMSO)	Sigma Aldrich
Trypan Blue Dye, 0.4%	Bio-Rad
Trypsin	Roth

3.1.5 Cell lines

Table 5 lists the different cell lines used in this study.

Table 5: Cell lines

Name	Cell Type/Short Description	Origin
Ba/F3-gp130	Eukaryotic, modified murine pro B-cell line, suspension	AG Scheller, Institute for Biochemistry and Molecular Biology II, Heinrich-Heine-Universität Düsseldorf
Expi293™	Eukaryotic, modified HEK293 cells for increased protein expression, suspension	Gibco, ThermoFisher Scientific, Life Technologies Corporation, Carlsbad
Expi CHO™	Eukaryotic, modified CHO cells for increased protein expression, suspension	Gibco, ThermoFisher Scientific, Life Technologies Corporation, Carlsbad
Bacteria strain Escherichia coli XL1-Blue (endA1 gyrA96(naIR) thi-1 recA1 lac glnV44 F' [: TN10 proAB+ laclqΔ(lacZ)M15] hsdR17(rk-mK+))	Prokaryotic, laboratory safety strain of *E. coli*, suitable for amplification and cloning of plasmid DNA	Agilent Technologies, Waldbronn
Phoenix-Eco	Human embryonic Kidneycells, modified HEK cells as viral packaging cell line	DKFZ, Ursula Klingmüller, Heidelberg, Deutschland

3.1.6 Plasmids

Plasmids used in the present study are listed in table 6.

Table 6: Plasmids

Name	Origin	Resistance
pMOWS-puro-GFP		Ampicilin, Puromycin
pEGFP	AG Scheller, Düsseldorf	Kanamycin
pcDNA3.1	Invitrogen, Darmstadt, Deutschland	Ampicilin
pcDNA3.1 P^{scFv}23Fc	Generated in this work	Ampicilin
pcDNA3.1 P^{scFv}0Fc	Generated in this work	Ampicilin
pcDNA3.1 P^{scFv}4Fc	Generated in this work	Ampicilin
pcDNA3.1 P^{scFv}8Fc	Generated in this work	Ampicilin
pcDNA3.1 PigG2	Generated in this work	Ampicilin
pcDNA3.1 P^{scFv}PigG2	Generated in this work	Ampicilin
pMOWS-puro-AIP1^{VHH}gp130	Generated in this work	Ampicilin, Puromycin
pMOWS-puro-AIP2^{VHH}gp130	Generated in this work	Ampicilin, Puromycin
pMOWS-puro-AIP3^{VHH}gp130	Generated in this work	Ampicilin, Puromycin
pMOWS-puro-AIP4^{VHH}gp130	Generated in this work	Ampicilin, Puromycin
pMOWS-puro-AIP1^{VHH}gp130Dstalk	Generated in this work	Ampicilin, Puromycin
pMOWS-puro-AIP2^{VHH}gp130 Dstalk	Generated in this work	Ampicilin, Puromycin
pMOWS-puro-AIP3^{VHH}gp130 Dstalk	Generated in this work	Ampicilin, Puromycin
pMOWS-puro-AIP4^{VHH}gp130 Dstalk	Generated in this work	Ampicilin, Puromycin

3.1.7 Primers

All the different primers used for cloning, mutagenesis and sequencing are listed in table 7.

Table 7: Primers

Name	Origin 5'-3'
5' pMOWS	AGCCCTTTGTACACCCTAAGC
3' pMOWS	AGCAATAGCATGATACAAAGG
pcDNA3.1 fw	AAATTAATACGACTCACTATAGG
pcDNA3.1 rv	AGGCACAGTCGAGGCTG
deltastalk fw	GCCATCGTGGTGCCT
deltastalk rv	GAATTTAGGGGTGGTGAAGGT
delPCR FC hinge fw	GTCGGCGACGTCTGTAAAAT
delPCR FC hinge rv	GGCGTTGATGTGGATCGACT
EAAAK4 fw	GGCCGCAGAAGCAGCTGCAAAAGAAGCAGCTGCAAAAGAAGCAGCT GCAAAAGAAGCAGCTGCAAAAGC
EAAAK4 rv	GGCCGCTTTTGCAGCTGCTTCTTTTGCAGCTGCTTCTTTTGCAGCTGCT TCTTTTGCAGCTGCTTCTGC
EAAAK8 fw	GGCCGCTGAGGCCGCTGCTAAGGAGGCCGCCGCTAAGGAGGCTGCC GCCAAGGAGGCCGCTGCCAAGGAGGCTGCTGCCAAGGAAGCCGCCG CCAAGGAAGCTGCCGCCAAAGAGGCCGCCGCCAAAGC
EAAAK8 rv	GGCCGCTTTGGCGGCGGCCTCTTTGGCGGCAGCTTCCTTGGCGGCGG CTTCCTTGGCAGCAGCCTCCTTGGCAGCGGCCTCCTTGGCGGCAGCCT CCTTAGCGGCGGCCTCCTTAGCAGCGGCCTCAGC

3.1.8 Cytokines

Hyper IL-6 was used as controls and to keep cells in culture was.

3.1.9 Antibodies

All the antibodies, fluorescently labeled or not, for western blot, cell culture, or FACS staining can be found in table 8.

Table 8: Antibodies

Name	Cat. #	Company
Tocilizumab (monoclonal IL-6R antibody) (ACTEMRA/RoACTEMRA®)	10219525	Roche
Anti-STAT3 (clone 124H6)	9139S	Cell Signaling Technology
Anti-phospho STAT3 (Tyr705) (clone D3A7)	9145S	Cell Signaling Technology
Anti-ERK1/2 (clone L34F12)	4696S	Cell Signaling Technology
Anti-phospho ERK1/2 (Thr202/Tyr204) (clone D13.14.4E)	9106S	Cell Signaling Technology
Anti-human-Fc POD	31423	Invitrogen AG
StrepMAB-Classic HRP	2-1509-001	IBA Lifsciences GmBH
Palivizumab		
BD Phosflow™ Alexa Fluor® 488 Mouse anti-Stat1 (pY701)	612596	BD Biosciences, Franklin Lakes, NJ, USA
PE Mouse anti-Total Stat1 (N-terminal)	558537	BD Biosciences, Franklin Lakes, NJ, USA
BD Phosflow™ Alexa Fluor® 488 anti-Stat3 (Tyr705)	557814	BD Biosciences, Franklin Lakes, NJ, USA
BD Phosflow™ PE anti-Stat3	560391	BD Biosciences, Franklin Lakes, NJ, USA
Anti-Myc	2278	Cell Signaling Technology, Frankfurt, Germany
Anti-Rabbit AlexaFluor™488	A21206	Invitrogen AG

3.1.10 Buffers

Table 9 contains the composition of all the buffers used in this study.

Table 9: Buffer compositions

Buffer Name	Composition
PBS (Phosphate Buffered Saline)	1.5 mM KH_2PO_4, 2.7 mM KCl, 8.1 mM Na_2HPO_4, 137 mM NaCl, pH 7.4
10x Standard Restriction Buffer	Commercial product, specific composition varies by manufacturer (e.g., Thermo Scientific)
10x T4 DNA Ligase Buffer	Commercial product, specific composition varies by manufacturer (e.g., Thermo Scientific)
Ammonium Peroxodisulfate (APS)	10% (w/v) APS solution
TAE Buffer (Tris-Acetate-EDTA)	0.4 M Tris-HCl (pH 8.8), 0.01 M EDTA, 0.2 M acetic acid
Agarose Gel Solution (1%)	4 g agarose in 400 mL TAE buffer
Trypsin/EDTA Solution	1:10 dilution of 10x trypsin/EDTA in PBS
Solution 1 (S1) for DNA Mini-Prep	50 mM glucose, 25 mM Tris-HCl (pH 8.0), 10 mM EDTA (pH 8.0), 1:1000 RNase in H_2O
Solution 2 (S2) for DNA Mini-Prep	200 mM NaOH, 1% SDS
Solution 3 (S3) for DNA Mini-Prep	3 M potassium acetate, 11.5% (v/v) acetic acid
SDS-PAGE Running Buffer	0.4 M Tris-HCl (pH 8.25), 0.1 M glycine, 0.1% SDS
SDS-PAGE Loading Buffer (6x)	375 mM Tris-HCl (pH 6.8), 9% (w/v) SDS, 50% (v/v) glycerol, 9% β-mercaptoethanol, 0.03% (w/v) bromophenol blue

Transfer Buffer	25 mM Tris-HCl (pH 8.0), 192 mM glycine, 20% (v/v) methanol
TBS (10x), Tris-Buffered Saline	5 M NaCl, 200 mM Tris-HCl (pH 7.5)
TBS-T	5 M NaCl, 200 mM Tris-HCl (pH 7.5), 0.05% (v/v) Tween-20
Western Blot Blocking Buffer (Milk-TBST)	5% milk powder in TBS-T
Western Blot Blocking Buffer (BSA-TBST)	5% BSA in TBS-T
Li-Cor Blocking Buffer	Li-Cor Biosciences GmbH
Coomassie Staining Solution	35% (v/v) ethanol, 10% (v/v) acetic acid, 0.3% (w/v) Coomassie G250
Coomassie Destaining Solution	35% (v/v) ethanol, 10% (v/v) acetic acid
Citrate Buffer pH 3.2	7.1 mM sodium citrate dihydrate, 42.9 mM citric acid
Citrate Buffer pH 5.5	35.2 mM sodium citrate dihydrate, 14.8 mM citric acid
Puffer W	100 mM Tris-HCl (pH 8.0), 150 mM NaCl, 1 mM EDTA
Puffer BXT	100 mM Tris-HCl (pH 8.0), 150 mM NaCl, 1 mM EDTA, 50 mM Biotin
Puffer XT-R	3 M $MgCl_2$
PBS p20	PBS with 0.05% (v/v) surfactant P20
NTA Regeneration Buffer	dH_2O, 350 mM EDTA
NTA Wash Buffer	dH_2O, 3 mM EDTA
NTA Nickel Buffer	dH_2O, 0.5 mM NiCl2
JAK2 Lysis Buffer (Cell Culture Lysates)	10 mM Tris-HCl (pH 7.5), 150 mM NaCl, 0.5 mM EDTA, 10 mM $MgCl_2$, 1 mM Na_3VO_4, 0.5% NP-40, 1 tablet protease inhibitor (Roche) per 50 ml buffer
DNA Hybridization Buffer	10 mM Tris, pH 7.5-8.0, 50 mM NaCl, 1 mM EDTA

3.1.11 Kits

Table 10 lists all commercial kits used in this study.

Table 10: Kits

Name	Company/Manufacturer
BCA Protein Assay	Thermo Fisher Scientific, Waltham, USA
CellTiter Blue	Promega GmbH, Mannheim
NucleoSpin Gel and PCR Clean-up	Macherey-Nagel, Düren
NucleoBond® Xtra Midi/Maxi	Macherey-Nagel, Düren, Germany
PE Annexin V Apoptosis Detection Kit I	BD Pharmingen™
Caspase 3/7 Activity Apoptosis Assay Kit	Cell Meter™

3.1.12 Devices

Devices that were used in this study are listed in the table 11 below.

Table 11: Devices

Equipment	Manufacturer	Location
Analytical balance Precisia 100M-300C	Precisia	Hartenstein
Autoclave Laboklav 25	SHP Steriltechnik AG	Detzel Schloss/Satuelle
Automated cell counter TC10	Bio-Rad	München
ÄKTA Start	GE Healthcare	Chicago
BD FACS Canto II	Thermo Scientific	St Leon-Rot
CO_2 incubator HERAcell 150	Thermo Scientific	St. Leon-Rot
Freezer Forma 900	Thermo Scientific	St. Leon-Rot
Gel documentation system Odyssey XF Imager	LI-COR Biosciences GmbH	Lincoln
Gel electrophoresis chamber	Bio-Rad	München
Orbital shaker Multiron HT	INFORS GmbH	Einsbach
Refrigerator	Liebherr GmbH	Rostock
Refrigerated centrifuge 5417 R	Eppendorf	Hamburg
Refrigerated centrifuge 5810 R	Eppendorf	Hamburg
Magnetic stirrer with heating	Heidolph Instr. GmbH	Schwabach
Research micropipettes	Eppendorf	Hamburg
Fluorescencemicroscope, BZ-9000	Keyence	Neu-Isenburg
Microwave Optiquick	Moulinex (Krups)	Offenbach
Mini centrifuge	Axon	Kaiserslautern
NanoDrop ND-1.000	Thermo Scientific	St. Leon-Rot
PCR thermocycler peqSta	Peqlab	Erlangen
pH meter	Sartorius	Ratingen
Battery-powered pipetting aid pipetus®	Hirschmann	Eberstadt
Biological safety cabinet	Thermo Scientific	St. Leon-Rot
Biological safety cabinet pump	HLC BioTech	Bovenden
Tabletop centrifuge 5424	Eppendorf	Hamburg
Trans-Blot TurboTM	Bio-Rad	München
UV table	Bio-Budget Technologies GmbH	Krefeld

3.1.13 Software

Software used in preparation, instrument control, and analysis of this work can be found in table 12.

Table 12: Software

Name	Company/Manufacturer
Microsoft Office 2019	Microsoft
SnapGene® 3.2.1	Dotmatics
Chimera 1.15	Resource for Biocomputing, Visualization, and Informatics (RBVI) at the University of California, San Francisco
Äkta Start / Unicorn™ Start 1.0	Cytiva
Tecan i-Control™ Version 3.9.1.0	Tecan
Image Studio Lite V. 5.2	LI-COR Biosciences
Biacore X100 Control Software	Cytiva
Biacore X100 Evaluation Software	Cytiva
GraphPad Prism 8.0.2	Dotmatics
bioRender	bioRender
Claude AI	Anthropic, 2025

3.2 Methods

3.2.1 Molecular biology techniques

3.2.1.1 DNA gel-electrophoresis

For genotyping, PCR products were applied to a 1% w/v agarose gel in TBE and separated by size via gel electrophoresis. To visualize the DNA under UV light sybr safe DNA gel stain was added (10.000X in DMSO) to the agarose gel before gel polymerization. The samples were prepared in 6X DNA loading dye and were loaded onto the gel. Beside the samples, 1 kb DNA ladder was added for control. Gels were run at 120 V in 1 X TAE buffer for 40 min. The DNA fragments were visualized using a UV based gel analyzing.

3.2.1.2 DNA extraction from agarose gels

DNA fragments were separated by agarose gel electrophoresis, visualized under UV light (365 nm), and excised from the gel. The gel slice containing the desired DNA fragment was transferred to a 2 mL microcentrifuge tube and purified using a NucleoSpin® Gel and PCR Clean-up kit according to the manufacturer's protocol.

3.2.1.3 Nucleic acid and protein concentration measurement

Nucleic acid and protein concentrations were determined spectrophotometrically using a NanoDrop 2000. Nucleic acid purity was assessed by the A260/A280 ratio (DNA > 1.8). Protein concentration was determined at 280 nm, utilizing the absorbance of aromatic amino acids (tryptophan, tyrosine, phenylalanine). Due to variable amino acid compositions, the exact protein concentration was determined using Beer-Lambert Law (Equation 1: Beer-Lambert Law:Equation 1).

Equation 1: Beer-Lambert Law:

$$concentration\ \frac{mg}{ml} = \frac{A280}{\varepsilon(M-1cm-1)} x\ 1(cm) x\ molecular\ weight\ (Da)$$

3.2.1.4 Restriction digest of DNA

The restriction digestion was performed to excise an insert from the plasmid DNA (pDNA) for subsequent cloning. Additionally, the DNA was also hydrolyzed using restriction enzymes (Thermo Fisher Scientific, Waltham) to verify the correct ligation of newly generated plasmids. In this process, the DNA sequence is specifically recognized by the restriction enzymes and hydrolyzed at the phosphodiester bond.

Depending on the restriction enzyme used, DNA double strands with overhangs (sticky ends) or without overhangs (blunt ends) can be generated. The restriction of 10 µg plasmid DNA each was performed with 10 U of the desired restriction enzyme and with the manufacturer-recommended buffer in a total volume of 50 µl for 2 h or overnight at 37°C. For verification of correct cloning, 4 µg pDNA was used, while for cloning purposes at least 30 µg was used. Subsequently, 10 µl TriTrack DNA loading dye was added to each 50 µl reaction mixture and an analytical or preparative gel electrophoresis was performed.

3.2.1.5 Dephosphorylation of DNA

To prevent religation of the linearized vector without insert after restriction digestion, the 5' end was dephosphorylated. For this purpose, the hydrolyzed restriction mixture was purified using NucleoSpin® Gel and PCR Clean-up kit to remove the restriction enzymes and the corresponding buffer. Alternatively, 1 U FastAP was added to the restriction digest mix. Subsequently, the purified DNA was incubated with 1 U FastAP (Thermo Fisher Scientific, Waltham) for 1 h or overnight at 37°C and then purified again. Dephosphorylation was only performed on blunt end hydrolyzed vectors.

3.2.1.6 DNA phosphorylation

If the insert did not originate from a restriction digest but was amplified by PCR, it was phosphorylated for subsequent ligation. PCR amplification products do not possess the 5' phosphate group required for ligation. For this purpose, T4 polynucleotide kinase (PNK) was used, which catalyzes the transfer of a phosphate group from adenosine triphosphate to a 5' hydroxyl group of the nucleic acid. The reaction was set up according to the following composition:

PCR product (entire volume)
5 µl ligase buffer
1 µl PNK
Add ddH_2O to 50 µl

The reaction mixture was incubated for 30 min at 37°C, the PNK was inactivated for 5 min at 75°C, and subsequently ligated.

3.2.1.7 DNA hybridization

Phosphorylized oligos were resuspended in DNA hybridization huffer at a concentration of 50 µM and mixed in equimolar amounts. The primers incorporated NotI overhangs, facilitating

subsequent cloning into the hinge region before the Fc tag after digestion and dephosphorylation of the target plasmid using NotI (see under 3.2.1.4 and 3.2.1.5)

3.2.1.8 Ligation of DNA fragments

Insert and vector were ligated together through the formation of a phosphodiester bond between the 3' hydroxyl end of one fragment and the 5' phosphate end of another fragment. For this purpose, the insert and vector DNA were previously cut with the same restriction enzymes. For the ligation, 100 ng vector and insert were used in a molar excess ratio of 1:5 or 1:7. In addition to insert and vector, 2 µl T4 ligase buffer, 2 µl PEG4000, and 2 µl T4 ligase were added to the ligation mixture in a total volume of 20 µl and incubated for 2 h at RT or overnight at 4°C.

3.2.1.9 Transformation of Plasmid DNA into chemical competent E.coli bacteria

For transformation, chemically competent *E.coli* XL-1 Blue bacteria were used, which were stored in 30 µl aliquots at -80°C. For the transformation, the cells were thawed on ice for 5 min and 0.5 µl pDNA or 10 µl ligation mixture was added. The transformation mixture was incubated on ice for another 5 min before heat shock at 42°C for 50 sec followed. The bacterial suspension was incubated on ice for 5 min before 500 µl antibiotic-free LB medium was added. Subsequently, the cells were regenerated for 30-60 min at 37°C and 1,000 rpm. The entire bacterial suspension was then plated on LB agar plates with corresponding selection medium and incubated overnight at 37°C.

3.2.1.10 Miniprep of plasmid DNA

For analysis of the pDNA with which the *E.coli* were transformed, the pDNA was isolated. For this purpose, one E. coli colony each was incubated in 1.8 ml LBamp or LBkan medium overnight at 37°C and 1,000 rpm. The pDNA was then isolated by mini-preparation according to the principle of alkaline lysis. For this, the bacterial culture was centrifuged (15,000 g, 1 min, RT) and the cell pellet was resuspended in 100 µl cold S1 buffer. Subsequently, 200 µl S2 buffer was added and incubated on ice for 5 min. This was followed by the addition of 200 µl cold S3 buffer, which neutralized the lysis through the potassium acetate contained in the S3 buffer. After subsequent centrifugation (17,000 g, 10 min, 4°C), the supernatant was transferred to a new reaction vessel, 500 µl cold isopropanol was added and centrifuged again (17,000 g, 15 min, 4°C). The precipitated pDNA was washed with 500 µl ethanol 70% (v/v) and centrifuged again (17,000 g, 5 min, 4°C), and after slight air-drying, the DNA precipitate was dissolved in 50 µl ddH_2O.

3.2.1.11 Midiprep of plasmid DNA

A midi preparation was performed to isolate larger quantities of pDNA. 150 ml of LB medium containing antibiotics were inoculated with bacteria and grown overnight. Bacteria were harvested by centrifugation at 5.000 rpm for 10 min at 4 °C. The supernatant was discarded. Plasmid DNA was purified using the silica column based, endotoxin free, NucleoBond Xtra Midi kit (Macherey-Nagel, Düren, Germany), all the components are listed in Table 11. The bacteria pellet was in resuspended in resuspension buffer at 4°C. Cells were treated with lysis buffer and incubated for five min at room temperature. In the meanwhile, the column together with the inserted column filter was equilibrated with equilibration buffer. The cell lysate was treated with neutralization buffer and the tubes were inverted several times and then incubated on ice for 5 min. The column filter was then loaded with the lysate and flow-through was discarded. The column filter was washed with filter wash buffer and subsequently the column filter was removed. The plasmid DNA is bound to the silica column. The column was washed with both washing solutions. Now plasmid DNA was eluted in a clean falcon in elution solution. DNA was precipitated with isopropanol and centrifuged at 5.000 rpm for 45 min at 4°C. The supernatant was discarded. The pellet was washed with 70% endotoxin-free ethanol and supernatant again discarded after 10 min of centrifugation at 4°C. The isolated pDNA was dissolved in 200 µl ddH_2O and the concentration was measured as described in 3.2.1.3.

Table 11 Solutions used in the plasmid DNA purification kit

Step	Name	Composition	Amount used
Cell resuspension	BUFFER-RES-EF	10 mM EDTA, 50 mM Tris-HCl, 100 µg/ µl RNase, pH 8.0	8 ml
Cell lysis	BUFFER-LYS-EF	200 mM NaOH, 1% SDS	8 ml
Equilibration of Filter	BUFFER-EQU-EF	100 mM Tris, 15% EtOH, 900 mM KCl, 0.15% Triton X-100, pH 6.3	15 ml
Neutralization	BUFFER-NEU-EF	2.8 M K acetate, pH5.1	8 ml
First wash step	BUFFER-FIL-EF	100 mM Tris, 5-20% EtOH, 1.15 M KCl, pH 6.3	5 ml
Second wash step	BUFFER-ENDO-EF	100 mM Tris, 5-20% EtOH, 1.15 M KCl, pH 6.3	35 ml
Third wash step	BUFFER-WASH-EF	100 mM Tris, 5-20% EtOH, 1.15 M KCl, pH 6.3	15 ml
Elution of DNA	BUFFER-ELU-EF	100 mM Tris, 15% EtOH, 1 M KCl, adjusted to pH 8.5	2 ml
DNA precipitation	Isopropanol		3.5 ml
DNA cleaning	70% EtOH-EF		2 ml
Dissolving of DNA	H_2O-EF		50 µl

3.2.1.12 Polymerrase chain reaction (PCR)

The amplification of specific regions of plasmid DNA was performed via PCR. For the reaction, a thermostable DNA polymerase, the starting plasmid DNA (template), polymerase buffer, specific oligonucleotides (primers), and free deoxynucleotides (dNTP) were combined in a PCR mixture.

PCR for DNA fragment amplification: For the amplification of specific DNA fragments for subsequent cloning, Phusion High-Fidelity polymerase (Thermo Fisher Scientific, Waltham) was used, as it possesses 3'→5' exonuclease activity (proof reading) and removes incorrectly incorporated nucleotides from the amplified DNA.

Table 13 lists a reaction mixture for the amplification of DNA fragments:

Table 13: Reaction mixture for PCR with Phusion DNA Polymerase

Component	Volume
Final concentration template DNA	20 ng
5x Phusion HF	5 µl
1x dNTPs	1 µl
200 µM forward primer	2.5 µl
200 µM Reverse Primer	2.5 µl
Phusion DNA polymerase	0.5 µl
ddH_2O	Ad 50 µl

The reaction was carried out with the following PCR program, which can be found in Table 14.

Table 14: PCR program for amplification of specific DNA regions with Phusion DNA

Step		Temperature	Time
Initial denaturation		98°C	30 sec
	Denaturation	98°C	10 sec
30 cycles	Annealing	~60°C	20 sec
	Elongation	72°C	20 sec/kb
Final elongation		72°C	5 min
Cooling		4°C	∞

Successful amplification was analyzed using agarose gel (3.2.1.1). Upon successful amplification, the PCR products were purified using NucleoSpin® Gel and PCR Clean-up, phosphorylated (3.2.1.6), and ligated into the corresponding vectors (3.2.1.7).

Colony PCR (cPCR): To verify correct cloning, a cPCR was performed. Here, the PCR was carried out without prior isolation of pDNA. The pDNA in the bacterial suspension served as the template. The bacterial colony to be analyzed was suspended in 20 µl ddH_2O and subsequently used for PCR. For the analysis, DreamTaq Green PCR Master Mix 2x was used, as proof reading was not necessary here. Furthermore, forward and reverse primers were used, where one primer hybridized specifically to the vector and the other to the insert. The reaction mixture and PCR program for cPCR can be found in Table 15 and Table 16, respectively.

Table 15:Reaction mixture for cPCR

Component	Volume
DreamTaq PCR master mix 2x	10 µl
Forward primer	1 µl
Reverse primer	1 µl
pDNA in *E. coli* suspension	5 µl
ddH_2O	to 20 µl

Table 16: PCR program for colony PCR

Step		Temperature	Time
Initial denaturation		95°C	5 min
	Denaturation	95°C	30 sec
30 cycles	Annealing	~55°C	30 sec
	Elongation	72°C	1 min/kb
Final elongation		72°C	5 min
Cooling		4°C	∞

To analyze the correct cloning, the PCR product was directly analyzed using agarose gel (3.2.1.1).

3.2.1.13 Sequencing

For sequence verification, the pDNA was externally sequenced by Microsynth Seqlab (Göttingen, Germany). For this purpose, the samples were submitted along with the desired oligonucleotides. The results were downloaded online, and .ab1 files aligned with the template sequence in SnapGene.

3.2.2 Protein biochemical methods

3.2.2.1 Lysis of Ba/F3 cells

For protein extraction from Ba/F3 or other suspension cells, cells were pelleted by centrifugation (1000 rcf, 1 min, room temperature) and the supernatant was discarded. Cell pellets were flash-frozen in liquid nitrogen and either processed immediately or stored at -20°C until lysis.

Depending on pellet size, cells were resuspended in 60-200 µl JAK/JAK2 lysis buffer. Cell lysis was performed under rotation at 4°C for 60 min. Following lysis, samples were centrifuged (10,000-15,000 g, 15 min, 4°C) to remove cellular debris. The supernatant containing the protein lysate was transferred to a new 1.5 ml reaction tube, and protein concentration was determined using the BCA assay.

3.2.2.2 Determination of protein concentration using bicinchoninicacid (BCA)

Protein concentrations in cell lysates were determined using the BCA protein assay kit (Thermo Fisher Scientific, Waltham, USA) according to manufacturer's instructions. The assay operates in two steps: first, Cu^{2+} is reduced to Cu^{+} in an alkaline environment in the presence of proteins. Subsequently, bicinchoninic acid reacts with Cu^{+} to form a purple-colored complex. This BCA/Cu complex forms proportionally to protein concentration within the linear range, and absorption was measured at 562 nm using a fluorometer.

For protein concentration determination, a standard curve was generated using defined concentrations of BSA. Cell lysates were diluted 1:10 or 1:20 in H_2O, and 25 µl of each sample was measured in duplicate. Protein concentrations of the samples were calculated using the BSA standard curve.

3.2.2.3 Sodium dodecyl sulfate polyacrylamide gel electrophoresis (SDS-PAGE)

Proteins were separated according to their molecular weight using discontinuous sodium dodecyl sulfate polyacrylamide gel electrophoresis (SDS-PAGE). Protein concentrations in cell lysates were determined using the BCA assay section (under 3.2.2.2). Prior to loading, samples were denatured in Laemmli buffer containing β-mercaptoethanol at 95°C for 10 min, which disrupted protein structure by reducing disulfide bonds and other interactions. The SDS in the buffer bound proportionally to protein size, conferring a uniform negative charge relative to molecular weight.

Polyacrylamide gels (1.5 mm thick) with 10% acrylamide concentration were used. Samples were loaded as either 50 µg total protein for cell lysates, according to concentration of the purified protein to reach the target amount. Electrophoresis was initially performed at 100 V until proteins entered the separating gel, then increased to 130 V. The polyacrylamide matrix acted as a molecular sieve, allowing smaller proteins to migrate faster toward the anode than larger ones.

Separated proteins were subsequently used for immunoblotting analysis. All electrophoresis was carried out in Bio-Rad electrophoresis chambers filled with 1X running buffer.

3.2.2.4 Western blot

To specifically detect the proteins, they were transferred from the previously separated SDS-PAGE gel onto a nitrocellulose (NC) membrane. For this purpose, the Trans-Blot Turbo semi-

dry transfer system from Bio-Rad (Munich, Germany) was used. This was achieved by applying a voltage, in which the negatively charged proteins were transferred onto the membrane. The NC membrane was equilibrated together with Whatman paper and the SDS-polyacrylamide gel in transfer buffer for 1 min. The SDS-polyacrylamide gel was placed on the NC membrane and covered on both sides with two additional Whatman papers. Protein transfer onto the NC membrane then followed for 30 min at a constant voltage of 25 V and a constant current of 1 A. The membrane was incubated in a 1:3 dilution of Intercept blocking solution (LI-COR Biosciences GmbH) in TBS for at least 1 h at RT. The NC membrane was incubated with the primary antibody either for 2 h at RT or overnight at 4°C. The membrane was washed 3 times for 3 min each with TBS-T before the NC membrane was incubated with the secondary antibody for 1 h at RT. Both the primary and secondary antibodies were prepared in a 1:3 dilution of blocking solution with the addition of 0.1% Tween20. Finally, the secondary antibody was washed off by washing 2 times for 3 min each with TBS-T and 1 time for 3 min with TBS before the proteins were detected. Detection was performed using the Odyssey XF Imager (LI-COR Biosciences GmbH, Lincoln, USA) gel documentation system.

3.2.2.5 Comassie staining of SDS polyacrylamide gels

To assess the overall protein composition and purity of purified proteins, Coomassie brilliant blue staining was employed. Following SDS-PAGE, gels were immersed in Coomassie staining solution and heated in a microwave for 60 sec at 600 W, followed by incubation on a rocking platform for at least 1 h. Coomassie brilliant blue (250R) binds to basic amino acids within polypeptides, rendering them visible as blue bands. Subsequent destaining with multiple changes of destaining solution removed background dye. A highly purified protein exhibited a single, intense band corresponding to its expected molecular weight in the eluate and purified fractions. Minor, faint bands could indicate potential protein fragmentation (e.g., at the expected size of an Fc tag), although these were typically insignificant for this study. Notably, low protein concentrations (< 5 µg) resulted in lightly stained bands, emphasizing the sensitivity limitations of the method.

3.2.2.6 Protein A affinity chromatography

Fc-tagged recombinant proteins as well as IgG2 antibodies expressed in Expi293 or ExpiCho cell culture supernatants were purified using Protein A affinity chromatography. Protein A, derived from the cell wall of *Staphylococcus aureus*, exhibits specific and pH-dependent binding to the IgG Fc region. A HiTrap MabSelect PrismA column (Cytiva, USA) was employed for this purpose. Following equilibration with PBS, the cell culture supernatant (30-

150 ml) was loaded onto the column at a flow rate of 1 ml/min, allowing for the capture of Fc-tagged proteins. Subsequently, the column was washed with 20 column volumes of PBS to remove unbound proteins.

Elution was achieved by a two-step pH reduction using citrate buffers (pH 5.5 followed by pH 3.2). This disrupted the Fc-protein A interaction, releasing the bound protein, which was collected in fractions. Elution fractions containing protein were pooled, and the protein concentration was determined as described in section 3.2.2.2.

The protein pool was concentrated using an Amicon ultra membrane (Merck, Darmstadt, Germany) to a volume of approximately 1.5 ml. Subsequently, buffer exchange to PBS was performed using a NAP-25 column (GE Healthcare, Chicago, USA). Protein concentration was determined again, and further analyses, including SDS-PAGE, Coomassie staining, and Western blotting, were conducted.

The column was regenerated with 30 column volumes of 0.5 M NaOH. Purified proteins were aliquoted and stored at -80°C.

3.2.2.7 StrepTactinXT affinity chromatography

For the purification of proteins with a C-terminal Twin-Strep-tag, Strep-Tactin affinity chromatography was employed. The Twin-Strep-tag specifically binds to Strep-Tactin, enabling the capture of the target protein. After binding, the column was washed to remove unbound proteins, and the target protein was eluted by competitive binding with biotin. The eluted protein was then buffer-exchanged into PBS.

The purification procedure utilized a Strep-Tactin® XP Flow® column (IBA-Lifesciences, Göttingen), which exploits the high-affinity interaction between the Twin-Strep-Tag® (SA-WSHPQFEK-(GGGS)2-GGSA-WSHPQFEK) and the Strep-Tactin matrix, analogous to the biotin-streptavidin interaction. Following column equilibration with running buffer (W), the culture supernatant was loaded. Subsequent washing with buffer W removed non-specifically bound proteins. Elution was achieved using biotin-containing buffer (BXT), which outcompetes the Twin-Strep-Tag® for binding to the Strep-Tactin matrix. Unlike protein A purification, acidic conditions were not required, eliminating the need for Tris neutralization.

After use, the column was regenerated with regeneration buffer (XTR), washed with buffer W, and stored in 20% ethanol at 4°C. Protein concentration was determined using NanoDrop. The protein was then concentrated and buffer-exchanged into PBS as described previously. Finally,

the purified protein was aliquoted, shock-frozen in liquid nitrogen, and stored at -80°C or used for further experiments.

3.2.2.8 Size exclusion chromatography

Size-exclusion chromatography (SEC) was employed to further purify proteins after affinity chromatography. This technique utilizes a porous matrix that interacts with proteins based on their size. Smaller proteins interact more extensively with the matrix pores, resulting in longer retention times. Larger proteins interact less effectively and elute more rapidly.

Either a Superdex 75 Increase or a Superdex 200 Increase column from GE Healthcare (Chicago, USA) was used. The column was equilibrated with degassed PBS for one h prior to use.

Protein samples (500 µL) were loaded onto the column, and the eluate was collected in fractions. Fractions containing the target protein were pooled.

To maintain consistent buffer conditions and avoid subsequent buffer exchange steps, PBS was used exclusively as the running buffer. Further concentration of the pooled fractions was not performed.

SEC can also be used to estimate the molecular weight of proteins. By comparing the elution volumes of the unknown protein to those of known protein standards, an approximate molecular weight of the target protein can be determined.

3.2.2.9 Surface plasmon resonance

Surface plasmon resonance (SPR) experiments were performed using a Biacore X100 instrument and Protein A sensor chips. Experiments were conducted at 25°C in PBS with 0.05% (v/v) surfactant P20 (GE Healthcare) added. For experiments involving protein interactions with immobilized receptors, the receptor was immobilized on the sensor chip, and different concentrations of the interacting protein were injected. Association and dissociation kinetics were measured, and the data was analyzed using a suitable binding model, such as a two-step reaction binding model. For experiments involving protein interactions with immobilized antibodies, the antibody or antibody fragment was captured on the sensor chip at a level of approximately 500-1000 response units (RUs). Different concentrations of the interacting protein were injected, and association and dissociation kinetics were measured. The data was analyzed using a 1:1 binding model.

3.2.2.10 Size-Exclusion Chromatography coupled with Small-Angle X-ray Scattering (SEC-SAXS)

SEC-SAXS was employed to determine the solution structure, molecular weight, shape, and flexibility of biomolecules and their complexes. Samples obtained from preparative SEC (under 3.2.2.8) were used for analysis to ensure proper buffer matching and background subtraction.

For complex analysis, proteins in identical buffer conditions were pre-incubated for 10 min prior to SEC-SAXS. Samples were then separated on a Superdex 200 increase 10/300 GL column. During elution, molecules were continuously exposed to an X-ray beam, with scattered X-rays detected to generate scattering patterns revealing molecular structure and conformation. Flow rates were optimized to ensure optimal separation during X-ray data collection across the q-range.

Data processing involved correction for background scattering and detector sensitivity, followed by Guinier analysis to determine the radius of gyration (Rg). The pair distance distribution function (PDDF) was calculated to provide information about molecular shape and size distribution in solution.

Structural modeling incorporated multiple computational approaches. Initial structure predictions were generated using Alpha-fold, while complex formation was modeled using computational docking methods such as CORAL. Final models were iteratively refined and selected based on their agreement with the experimental data.

3.2.3 Cell biological methods

3.2.3.1 Cultivation of adherent eukaryotic cells

Ba/F3 suspension cells were cultured in 10 cm petri dishes containing 10 ml DMEM+/+ supplemented with Hyper-IL-6 (10 ng/ml). Cells were passaged at a 1:10,000 ratio every seven d. Puromycin as a selection antibiotic was added every two weeks as appropriate.

Adherent cells (HEK293 and Phoenix-Eco) were cultured in 10 cm culture dishes containing 10 ml DMEM+/+. For passaging every 3-4 d, the supernatant was removed, and cells were resuspended in 1 ml PBS, of which 50 µl was transferred to a new culture dish. Depending on the cell line, selection antibiotics were continuously maintained at a 1:1,000 ratio.

Expi293 cells and ExpiCho cells were cultured in flasks containing 30 ml Expi293™ or ExpiCHO-S™ expression medium without antibiotics. Cell density was determined using an automatic cell counter every 3-4 d, and cells were seeded at a concentration of 300,000 cells/ml.

Culture conditions were maintained at 37°C and 5% CO_2 in a humidified atmosphere for Ba/F3 gp130 and Phoenix-HEK cells. Expi293 and ExpiCho cells were maintained at 37°C and 8% CO_2 on an orbital shaker (120 rpm). The cells were also cultured in a humidified atmosphere.

3.2.3.2 Transfection of HEK293 phoenix cells

$5x10^5$ HEK phoenix cells were seeded per well in 6-well plates culture dish. After 24 h, 2 µg pMOWS expression plasmid DNA, which also expresses some of the viral proteins, was mixed with 4 µl Turbofect (Thermo Fisher Scientific, Waltham, USA) in 200 µl DMEM -/- and incubated for 15 min at room temperature. The mixture was then added dropwise to the cells. After 6 h, the medium was replaced with DMEM +/+ containing 30% FCS, and cells were cultured overnight. Transfection efficiency was evaluated the next day by fluorescence of the control plasmid expressing GFP. Virus-containing cell culture supernatant was collected from Phoenix-Eco cells and centrifuged (350 g, 5 min, room temperature) to remove residual cells. The supernatant contains the viral particles and can be used for retroviral transduction see section 3.2.3.4.

3.2.3.3 Transfection of ExpiCHO cell lines for protein expression

Recombinant proteins were expressed using modified suspension-adapted HEK293 (Expi293F™) and CHO (ExpiCHO-S™) cell lines (ThermoFisher Scientific). These cell lines are optimized for high-density culture in shake flasks and enhanced protein expression following transient transfection.

Transfections were performed using the corresponding ExpiFectamine™ transfection kits and OptiPRO™ SFM complexation medium following the manufacturer's protocols.

Protein expression was carried out for 7-10 d post-transfection. The secreted proteins were harvested from the culture medium through a two-step centrifugation process: first at 450 x g for 5 min to remove cells, followed by 4,000 x g for 20 min to remove remaining cellular debris. The supernatant was further clarified by filtration through a 0.45 µm syringe filter. The filtered supernatant was either processed immediately for protein purification by affinity chromatography or stored at -80°C for later use.

3.2.3.4 Retroviral transduction of Ba/F3 gp130 cells

To stably express the synthetic cytokine receptors in Ba/F3-gp130 cells, a retroviral transduction approach was employed. Ba/F3/gp130 cells were retrovirally transduced using supernatants from transfected Phoenix-Eco cells containing retroviruses. For this purpose, 250 µl Phoenix-Eco cell culture supernatant was mixed with $1x10^5$ target cells in 50 µl and 30 µg

polybrene (Sigma-Aldrich, Sternheim, Germany) and centrifuged (2 h, 300 g, room temperature). The cell pellet was resuspended in 5 ml DMEM +/+ supplemented Hyper-IL-6 (10 ng/ml) to maintain cell viability and cultured in a 6-well cell culture plate. Transduced cells were selected over 2-3 weeks through antibiotic selection using 1.5 µg/ml Puromycin (48 h after transduction). Successful transduction was verified after selection by flow cytometry (3.2.3.4) and Western blotting.

3.2.3.5 Flow cytometry analysis for surface expression of receptors

Surface expression of synthetic receptors following retroviral transduction was analyzed by flow cytometry, based on antigen-antibody interactions using fluorescently labeled antibodies. The cells are not permeabilized, hence antibodies only stain proteins exposed on the cell surface. For analysis, $5x10^5$ Ba/F3 cells were centrifuged (350 g, 5 min, RT), and the cell pellet was washed in 1 ml FACS buffer. Cells were then resuspended in 50 µl FACS buffer containing the appropriate primary antibody specific for the myc tag fused to the synthetic receptor. After 1 h incubation at RT, cells were washed with 1 ml FACS buffer, and the cell pellet was resuspended in 50 µl FACS buffer containing the corresponding fluorescently labeled secondary antibody. Cells were incubated for 50 min at RT in the dark, followed by a final wash step. The cells were then resuspended in 500 µl FACS buffer and analyzed using a FACSCanto II flow cytometer. Data analysis was performed using FlowJo_V10 software to determine the shift of receptor-expressing cells based on fluorescence intensity compared to untransfected cells.

3.2.3.6 Proliferation assay in Ba/F3 gp130 cells

To assess the proliferative response of Ba/F3-gp130 cells to synthetic ligands, cell viability assays were performed. Ba/F3-gp130 cells were seeded at a density of 1×10^4 cells per well in 96-well plates and incubated for 72 h with various concentrations of the synthetic ligands.

To determine the effective concentration 50% (EC50), concentration-dependent proliferation was performed. The proliferation of Ba/F3 cells with the corresponding receptors was investigated as a function of cytokine concentration. A high initial cytokine concentration was chosen, followed by serial 1:2 dilutions.

CellTiter-Blue reagent, which contains a redox dye that is cleaved by metabolically active cells, was added to each well. The resulting fluorescence, directly proportional to cell viability, was measured at 560 nm excitation and 590 nm emission using an Infinite M200 PRO plate reader.

Fluorescence measurements were taken immediately after adding the reagent (time point 0) and at regular intervals up to 120 min. Background fluorescence at time point 0 was subtracted from subsequent readings to obtain normalized values.

The obtained proliferation curves were analyzed using non-linear regression with GraphPad Prism 8 software to determine the EC50 values.

3.2.3.7 Stimulation assay of Ba/F3-gp130 cells

To evaluate signal transduction in Ba/F3 cells and the accompanying phosphorylation of STAT3 or Erk1/2, stimulation assays were performed. Ba/F3 cells expressing the relevant receptors were washed with PBS and resuspended in serum-free DMEM and starved for for 3-4 h. This is done to minimize serum-induced signal transduction. When using the inhibitor P6, it was added to the cells 30 min prior to stimulation. Subsequently, the cells were stimulated with the appropriate cytokines for indicated times ranging from 15 to 120 min at 37°C. Following stimulation, the cells were centrifuged, and the reaction was stopped by snap-freezing the cell pellets in liquid nitrogen. Subsequent lysis was performed as described under 3.2.2.1.

3.2.3.8 Phosphorylation measurement by flow cytometry analysis

To assess the activation of the STAT3 signaling pathway, Ba/F3-gp130 cells were stimulated with specific ligands or antibodies. Before stimulation, cells were washed three times with phosphate-buffered saline (PBS) and starved in serum-free medium for 3 h to minimize background signaling. Cells were then stimulated with the indicated factors for 45 min at 37°C.

To analyze STAT3 phosphorylation by flow cytometry, cells were fixed with paraformaldehyde to preserve protein structure and permeabilized with methanol to allow antibody access to intracellular epitopes. Fixed and permeabilized cells were then incubated with fluorophore-conjugated primary antibodies specific for total STAT3 and phosphorylated STAT3 (pSTAT3, Tyr705).

After washing, cells were analyzed by flow cytometry using a FACSCanto II instrument. The fluorescence intensity of the labeled antibodies was measured, allowing for the quantification of total STAT3 and pSTAT3 levels within the cell population. FlowJo software was used to analyze the flow cytometry data and determine the percentage of cells with activated STAT3 signaling.

3.2.3.9 Annexin-V staining

To assess cell viability and apoptosis, Annexin V/7-aminoactinomycin D (7-AAD) staining was performed. Ba/F3-gp130 cells were washed three times with phosphate-buffered saline (PBS) and 1.25 x 10^5 cells were seeded per well. Cells were then incubated with the indicated cytokines for 24 h. As a positive control for apoptosis, some cells were treated with ethanol, which induces cell death.

Following incubation, cells were washed twice with ice-cold PBS and, if necessary, fixed with 70% ethanol. Cells were then resuspended in Annexin V binding buffer and stained with Annexin V-PE and 7-AAD. Annexin V binds to phosphatidylserine, a phospholipid that is translocated from the inner to the outer leaflet of the plasma membrane during early apoptosis. 7-AAD is a DNA-binding dye that cannot penetrate viable cells but can enter cells with compromised membrane integrity, indicating late-stage apoptosis or necrosis.

Flow cytometry was used to analyze the stained cells, and 20,000 events were recorded. By measuring the fluorescence intensity of Annexin V and 7-AAD, it was possible to distinguish between viable cells, early apoptotic cells, late apoptotic cells, and necrotic cells.

3.2.3.10 Caspase 3/7 measurement

To assess the induction of apoptosis, a fluorimetric caspase-3/7 assay was performed. Ba/F3-gp130 cells were washed three times with phosphate-buffered saline (PBS) and 1.25x10^5 cells were seeded per well in a 96-well plate. Cells were then incubated with the indicated cytokines for 6 h to induce apoptosis.

Subsequently, the Amplite Fluorimetric Caspase-3/7 Assay Kit (AAT Bioquest) was used to detect caspase activity. A specific caspase-3/7 substrate was added to the cells and incubated for 2 h at room temperature. This substrate is cleaved by active caspase-3 and -7, releasing a fluorescent product.

The fluorescence intensity of the cleaved substrate was measured using an Infinite M200 PRO plate reader (Tecan) with excitation at 350 nm and emission at 450 nm. Increased fluorescence intensity indicates higher levels of caspase activity and, consequently, a greater extent of apoptosis.

4 Results

To create therapeutically viable SyCyRs, Palivizumab was selected as the prototype ligand of choice. The initial development encompassed several steps: the generation of anti-idiotypic nanobodies, their subsequent incorporation into the SyCyR system, and the engineering and validation of Palivizumab as an agonist to trigger cellular responses.

4.1 Development and Characterization of Anti-Idiotypic Nanobodies Against Palivizumab

To generate anti-idiotypic nanobodies against Palivizumab, we implemented a systematic immunization strategy utilizing a llama model system. We selected this camelid species due to its unique capacity to produce heavy-chain-only antibodies, from which nanobodies can be derived. Following the immunization with Palivizumab, a humanized monoclonal antibody employed in respiratory syncytial virus prophylaxis, we isolated peripheral B cells from blood samples. These cells, representing the mounted immune response against Palivizumab, served as the source for genetic material encoding the nanobody repertoire.

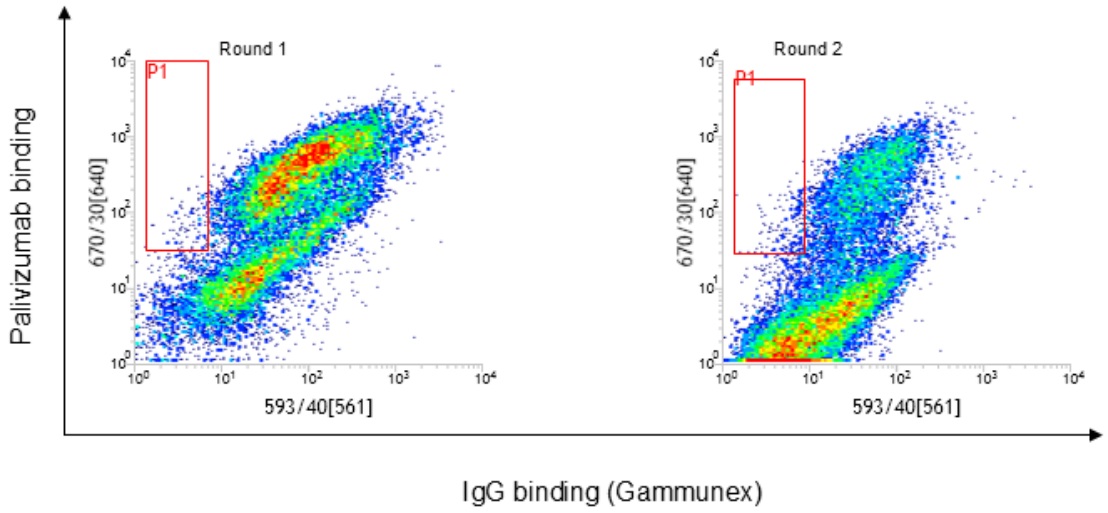

Figure 6: *Yeast Display FACS sort.*
Yeast cells underwent a sequential staining procedure. Initially, cells were pre-blocked with Gammunex® (1 mg/ml) and subsequently labeled with anti-human Fc-PE conjugate. These pre-stained cells were then incubated with Palivizumab at a concentration of 60 nM, followed by detection using an anti-Fab (κ-chain)-APC conjugate. The selection process comprised two sequential rounds of fluorescence-activated cell sorting to ensure isolation of high-affinity binders. This dual-color labeling strategy enabled discrimination between specific and non-specific binding events.

Subsequently, we amplified VHH-encoding cDNAs via PCR and introduced them into the PCT yeast display vector through gap repair cloning, utilizing the EBY100 yeast strain. The resulting

yeast surface display library underwent a stringent selection process employing fluorescence-activated cell sorting (FACS). To ensure specificity, we first implemented a negative selection step using Gammunex® 10% (1 mg/ml), effectively eliminating clones exhibiting non-specific binding to human immunoglobulin structures. Clones binding to epitopes on the IgG framework of Palivizumab would bind to the IgG in Gammunex® while those specifically binding the hypervariable region of Palivizumab would not bind to Gammunex®. The selection protocol continued with sequential incubation steps: first with fluorescent-labeled anti-human-Fc-PE conjugate, followed by Palivizumab (60 nM) and anti-Fab(κ-chain)-APC conjugate (Figure 6).

Through this sophisticated dual-color labeling strategy, we specifically isolated yeast cells displaying exclusive APC fluorescence, indicating Palivizumab-specific binding. After two consecutive rounds of sorting, we successfully identified four distinct anti-idiotypic nanobodies, designated AIP1-4VHH. These candidates were subsequently cloned into pcDNA vectors to add a twin-strep-tag. The proteins were expressed in the Expi-293F™ expression system and purified to homogeneity via affinity chromatography. The sequences are attached in the supplemental information section.

This part of the study was done with our collaboration partners in Prof. Harald Kollmars lab at the university of Darmstadt (*138*).

4.2 Binding kinetics and characterization of AIPs

Surface plasmon resonance (SPR) analysis revealed distinct binding characteristics among the purified anti-idiotypic nanobodies. Most notably, AIP1^{VHH} exhibited exceptional binding properties with a very low dissociation constant (KD) of 25.97 picomolar (Figure 7 A). This high affinity resulted from the combination of fast association kinetics (ka = 2.3 x 106 1/Ms) and extremly slow dissociation kinetics (kd = 5.9 x 10-5 1/s). The remaining candidates demonstrated good affinities, with KD values of 2.16 nM (AIP2^{VHH}) (Figure 7 B), 1.11 nM (AIP3^{VHH}) (Figure 7 C), and 3.14 nM (AIP4^{VHH}). Noticeable was that AIP4^{VHH} exhibited a substantially higher dissociation rate compared to the other nanobody variants (Figure 7 D).

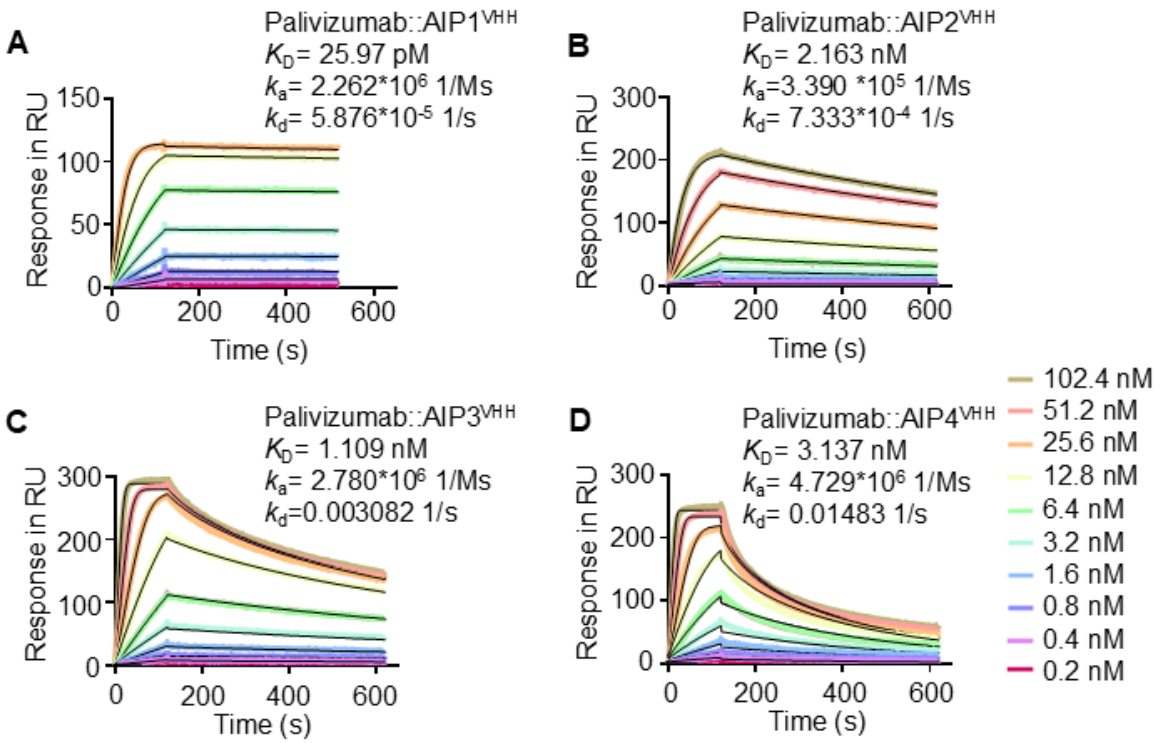

Figure 7: Characterization of Anti-idiotypic Nanobodies Binding to Palivizumab.
Surface plasmon resonance analysis of nanobody-Palivizumab interactions. Sensorgrams show binding kinetics for (B) AIP1^{VHH}, (C) AIP2^{VHH}, (D) AIP3^{VHH}, and (E) AIP4^{VHH} to immobilized Palivizumab. Each nanobody was tested across a twelve-point concentration series (0.05-102.4 nM) with 1:2 dilution steps. Association was measured during a 120-second injection phase, followed by a 500-second dissociation phase. Colored lines represent experimental data in response units (RU), while black lines indicate the global kinetic fit. The analysis was performed at 25°C using a constant flow rate, with Palivizumab immobilized on the sensor surface.

Competition studies utilizing the commercial anti-idiotypic antibody AbD23967 (aiPalivizumab) provided insights into binding epitopes. AIP1^{VHH}, AIP2^{VHH}, and AIP3^{VHH} demonstrated clear dose-dependent displacement of aiPalivizumab with IC50 values of 1.76 nM, 4.40 nM, and 48.55 nM respectively (Figure 8). Suggesting binding to the same epitope as aiPalivizumab. In contrast, AIP4^{VHH} showed no displacement of aiPalivizumab, suggesting either kinetic limitations or recognition of an alternative epitope.

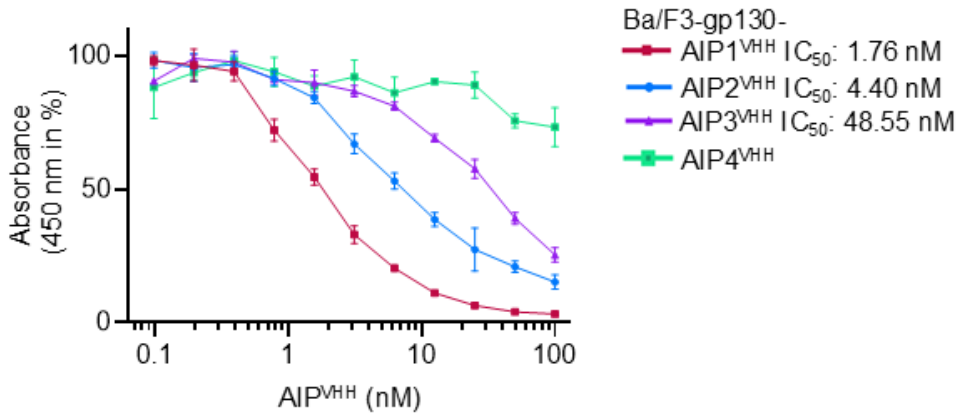

Figure 8: Competitive ELISA Analysis of Anti-idiotypic Nanobodies Against Palivizumab. Competition binding assay using anti-idiotypic Palivizumab IgG antibody (AbD23967) at a fixed concentration (1 nM) as detection reagent, challenged with increasing concentrations of soluble AIP1-4VHH nanobodies (concentration range: 0.1-100 nM). Data points represent mean values from three biological replicates (n=3) with error bars indicating standard deviation (S.D.). The graph shows one representative experiment demonstrating competitive binding behavior between the anti-idiotypic antibody and the nanobody variants.

4.4 Structural Analysis of AIP1^{VHH} and Its Complex with Palivizumab

To elucidate the molecular basis of the anti-idiotypic interaction between AIP1^{VHH} and Palivizumab, we employed small angle X-ray scattering (SAXS), a powerful technique for analyzing protein structures in solution.

As a first step we isolated both proteins and brought them in the exact same buffer to prevent any influence of the salt concentration on the SAXS results. For AIP1-ts we first isolated the protein using affinity chromatography (Figure 9 A) and immediately afterward applied it to the superdex100 SEC column to isolate the peak at 98 ml (Figure 9 B).

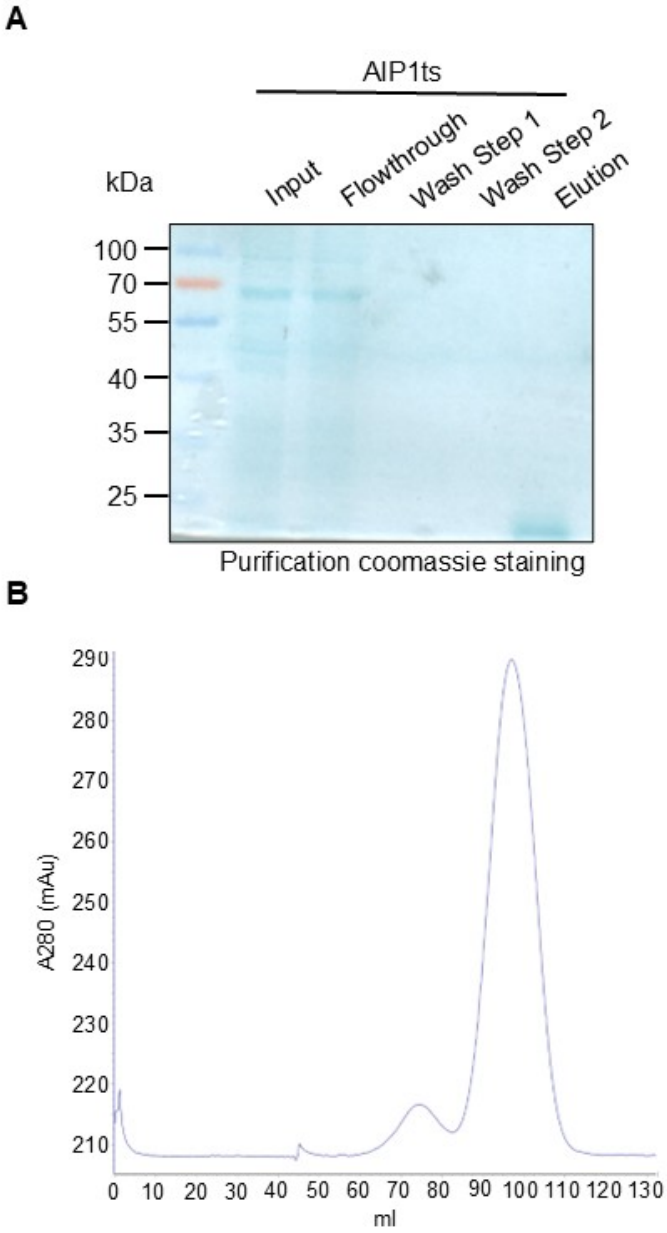

Figure 9:AIP1 is pure and monomeric in solution.

(A) Purification of AIP1ts showing Input, Flowthrough (FT), first and second washing step (Wash 1 and 2) as well as the final elution after Commassie staining. (B) SEC run of AIP1ts shows a well resolved peak as well as some contamination or dimer in a much smaller separate peak at A280.

As a next step the SAXS profile of AIP^{VHH}ts was collected showing a good agreement between the predicted CORAL model and the actually measured values. The estimated D_{max} also corresponds to other, previously published, nanobodies (Figure 10).

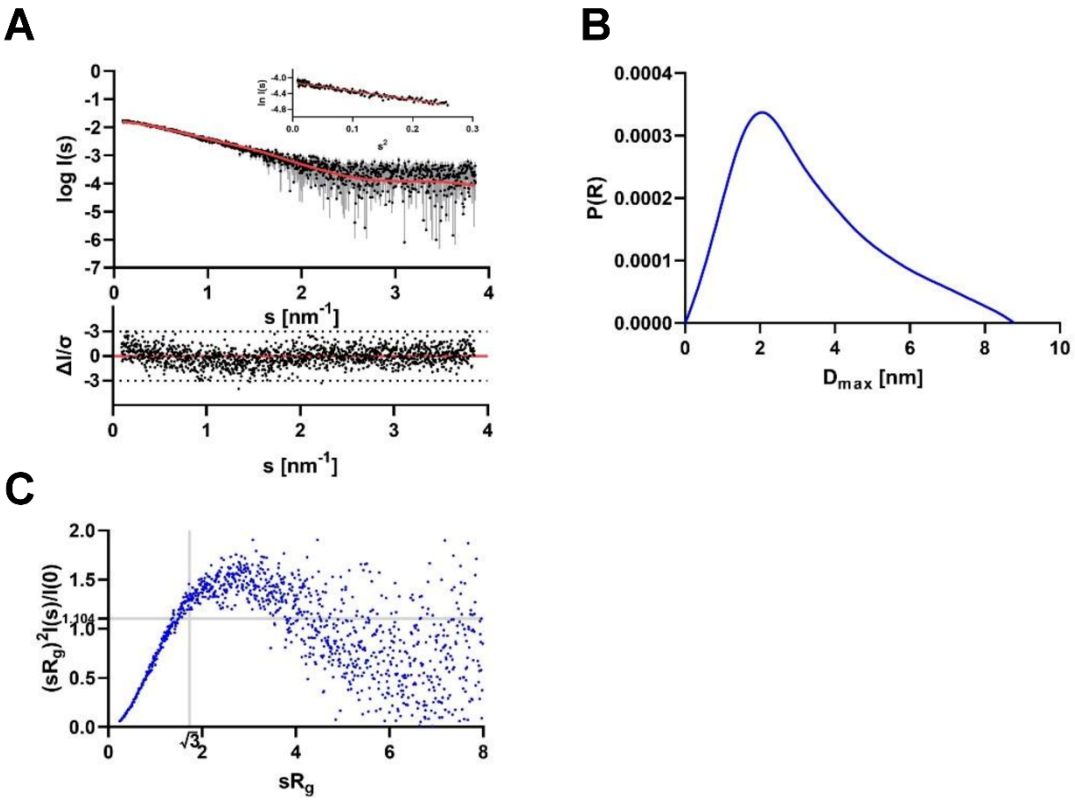

Figure 10: Small-angle X-ray Scattering Analysis of Apo AIP1^{VHH}.
(A) Experimental SAXS profile of apo AIP1^{VHH} nanobody. Black dots with grey error bars represent experimental data points. Red line shows the theoretical fit generated by CORAL modeling. The residual plot below demonstrates the quality of fit. Inset: Guinier plot showing linearity at low q values, indicating sample monodispersity. (B) Pair-distance distribution function p(r) for AIP1^{VHH}, representing the distribution of intramolecular distances within the molecule and providing information about the overall particle shape and maximum dimension. (C) Dimensionless Kratky plot for apo AIP1^{VHH}, indicating the degree of protein folding and conformational flexibility in solution.

For Palivizumab we first validated the purity of the commercially available antibody on Westernblot (Figure 11 A) and Coomassie staining (Figure 11 B). We then applied the commercial antibody directly to a preparative superdex SEC column and isolated the peak at retention time 90 ml (Figure 11 C).

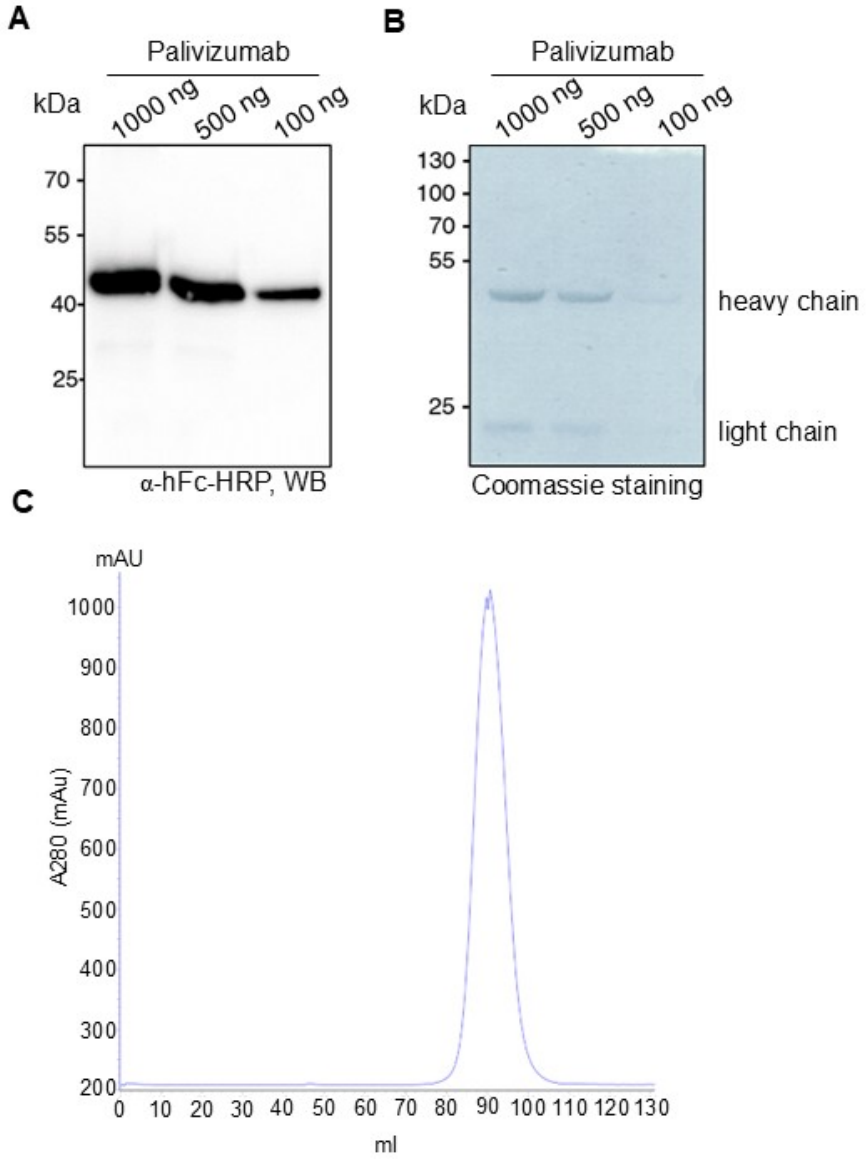

Figure 11: Palivizumab is pure and monomeric in solution.
(A) Different amounts of Palivizumab (100-1000 ng) in Western blotting using anti Fc antibody coupled to HRP. (B) Different amounts of Palivizumab (100-1000 ng) after Commassie staining. (C) SEC run of Palivizumab shows a single well resolved peak at A280.

We subsequently measured the SAXS profile of Palivizumab alone (Figure 12 A) and then incubated Palivizumab with AIP^{VHH}ts to measure the SAXS profile of the resulting complex (Figure 12 B). It can be observed in the overlay plots that Palivizumab is smaller than the complex (Figure 12 C-E, black line and green line respectively).

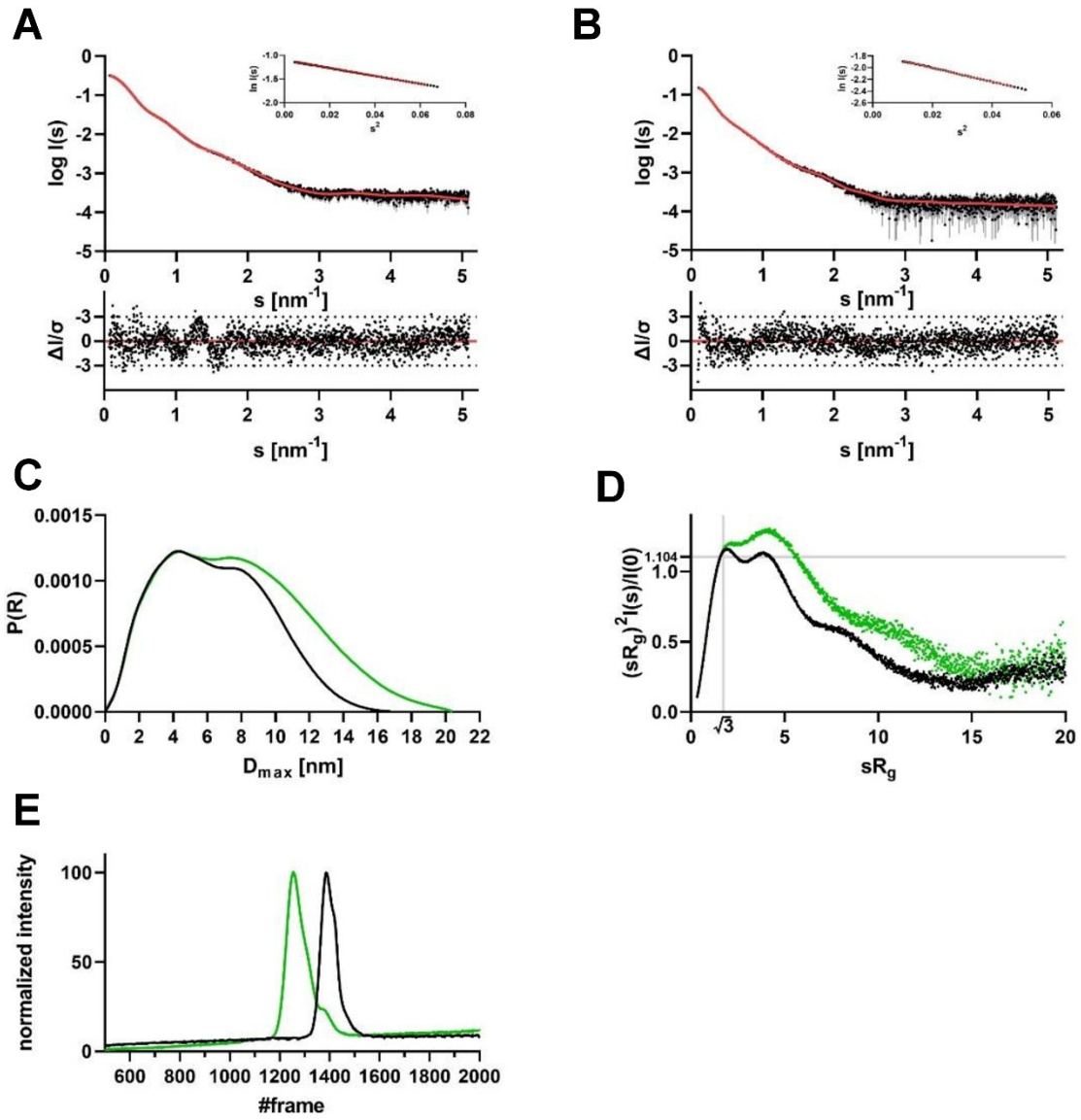

Figure 12: Small-angle X-ray Scattering Analysis of Palivizumab and its Complex with AIP1^{VHH}.

(A) SAXS profile of apo Palivizumab. Experimental scattering intensities are represented by black dots with associated grey error bars. The theoretical fit generated by CORAL modeling is shown as a red line, with the corresponding residual plot displayed below. Inset: Guinier plot demonstrating sample quality and monodispersity at low q values. (B) SAXS profile of the Palivizumab-AIP1^{VHH} complex. Experimental data points are shown in green with grey error bars. The CORAL model fit (red line) and residual plot are displayed analogously to panel A. Inset: Guinier analysis of the complex. (C) Comparison of pair-distance distribution functions p(r) between apo Palivizumab (black line) and the Palivizumab-AIP1^{VHH} complex (green line), illustrating changes in molecular dimensions and shape upon complex formation. (D) Dimensionless Kratky plots comparing the conformational properties of apo Palivizumab (black dots) and the Palivizumab-AIP1^{VHH} complex (green dots), providing insights into structural flexibility and compactness. (E) Normalized SEC-SAXS elution profiles obtained using Chromixs analysis for apo Palivizumab (black line) and the Palivizumab-AIP1^{VHH} complex (green line), demonstrating sample homogeneity and complex stability during measurement.

To interpret the SAXS data, we utilized structures of Fc and Fab fragments as initial structural templates for an initial AlphaFold2-generated model of Palivizumab. These models underwent iterative refinement using the CORAL algorithm until achieving optimal agreement between the predicted and experimental SAXS profiles, resulting in high quality tertiary protein structure.

The analysis established that both proteins maintain their expected conformational states in solution. AIP1^{VHH} (Figure 13 A) exists as a well-folded monomer, while Palivizumab maintains its characteristic dimeric configuration, consistent with typical Y-shaped IgG architecture (Figure 13 B). Upon complex formation, the stoichiometry revealed a precise 2:1 binding ratio, where each Palivizumab monomer engages two AIP1^{VHH} molecules. The binding interface analysis revealed that AIP1^{VHH} specifically targets the hypervariable antigen-binding loops of Palivizumab, effectively masking the complementarity-determining regions (CDRs) on both heavy and light chains (Figure 13 C). Upon detailed examination of the binding interface, it was revealed several critical molecular interactions. Two key arginine residues in AIP1^{VHH} (R31 and R54) form specific interactions with aspartate residues (D56 and D60) in the Palivizumab light chain. Additionally, tyrosine residues Y101 and Y32 of AIP1^{VHH} establish important contacts with K58 on the Palivizumab light chain. Of particular interest is the identification of probable hydrophobic interactions between R54 of AIP1^{VHH} and aromatic residues W105 and F95 of Palivizumab via cation-π(*139*). These interactions likely contribute significantly to the complex's stability and specificity. Through SAXS-based tertiary structure modeling, we calculated that the maximum distance between the two antigen-binding epitopes of Palivizumab and AIP1^{VHH} spans approximately 150 Ångström.

This part of the study was done in collaboration with Prof. Sander Smits of the center for structural studies of the Heinrich Heine University Düsseldorf.

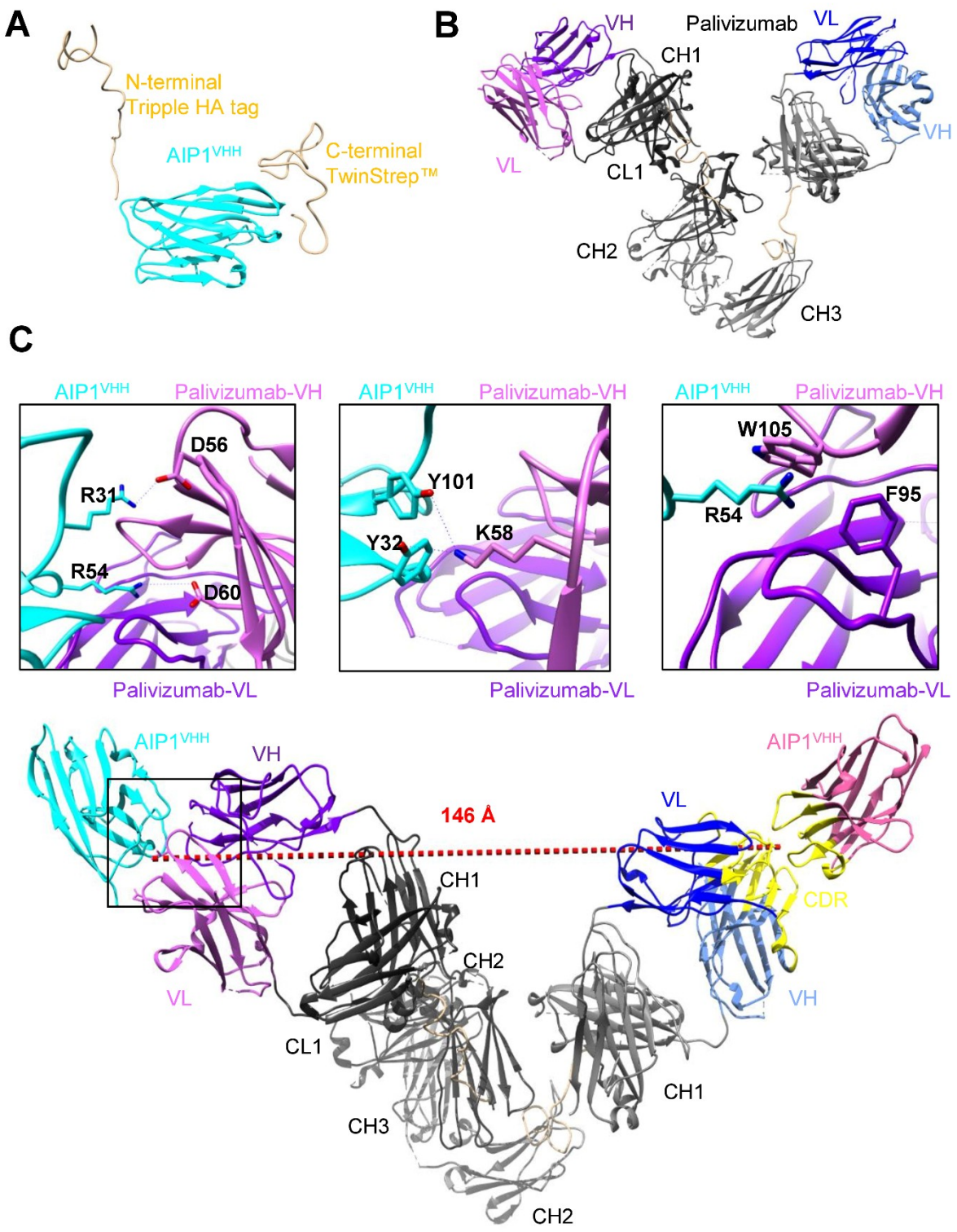

Figure legend on next page.

Figure 13: Structural Characterization of the AIP1^{VHH}-Palivizumab Complex by Small-angle X-ray Scattering**.**
(A) AlphaFold-based rigid body model of AIP1^{VHH} derived from SAXS analysis, highlighting flexible N- and C-terminal regions. (B) Rigid body model of Palivizumab IgG showing flexible linker regions (beige) connecting the Fc and Fab domains. (C) Molecular docking analysis of the AIP1^{VHH}-Palivizumab complex. The spatial arrangement reveals a 146 Å distance between paratopes (indicated by red dotted line). Right panel: Interface analysis showing CDR regions of both AIP1^{VHH} and Palivizumab (yellow). Detailed insets demonstrate key interaction interfaces with critical amino acid residues and their distances (blue dotted lines). Color coding: Heavy chains (purple/dark blue), light chains (pink/light blue), constant regions (black/coal), and AIP1^{VHH} (cyan/magenta).

4.5 Functional Analysis of SyCyRs using Palivizumab

It was then proceeded to genetically fuse AIP1-4^{VHH} to the transmembrane and intracellular domain of gp130, resulting in anti-idiotypic SyCyRs. An exemplary sequence is attached in the supplemental information section. The resulting chimeric receptors were designated as AIP1^{VHH}gp130, AIP2^{VHH}gp130, AIP3^{VHH}gp130, and AIP4^{VHH}gp130, respective to the nanobody they were fused to. In westernblotting total protein expression was oberserved for all 4 constructs. AIP4^{VHH}gp130 had the highest, followed by AIP2^{VHH}gp130 and AIP3^{VHH}gp130 while AIP1^{VHH}gp130 showed the lowest expression level (Figure 14 A). Expression analysis in Ba/F3-gp130 cells revealed varying levels of surface expression, with AIP1^{VHH}gp130 showing the highest expression, followed by AIP2^{VHH}gp130 and AIP3^{VHH}gp130, while AIP4^{VHH}gp130 demonstrated the lowest surface presence (Figure 14 B). These conflicting results can be explained by higher retention of AIP4^{VHH}gp130 in the endomembrane system and less transport to the cell membrane.

To evaluate the functionality of the engineered receptor constructs, we employed the Ba/F3-gp130 cell system, which is characterized by its responsiveness to Hyper IL-6 (HIL-6) through JAK/STAT signaling and cellular proliferation (*140*). Upon stimulation with Palivizumab (Figure 15 A), none of the AIP^{VHH}gp130 receptor variants were able to induce STAT3 phosphorylation in response to Palivizumab stimulation (Figure 15 B).

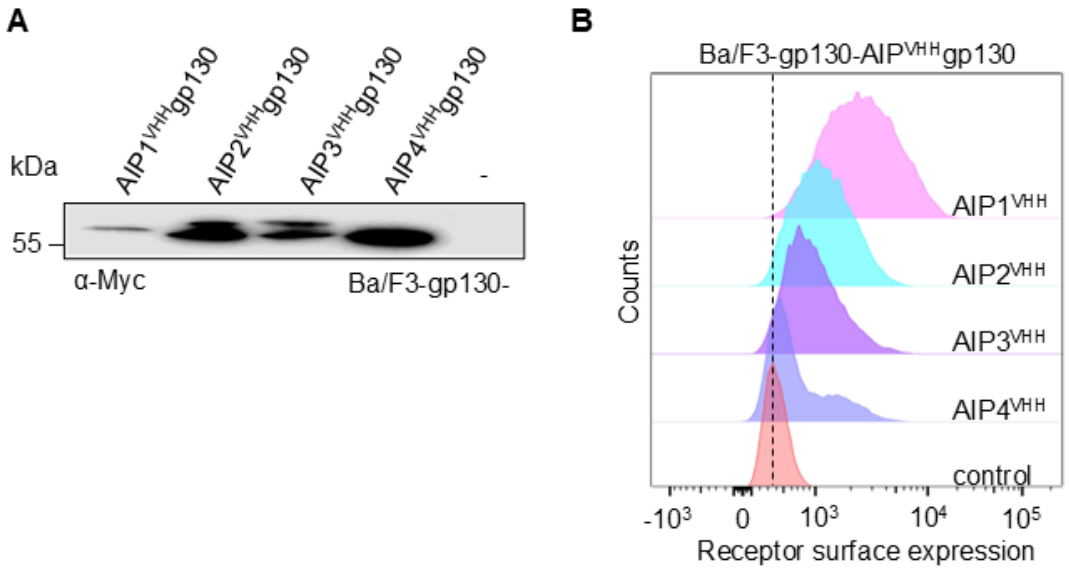

Figure 14: Analysis of AIP1-4VHHgp130 Synthetic Cytokine Receptor Expression.
(A) Western blot analysis demonstrating expression of myc-tagged synthetic cytokine receptors in Ba/F3-gp130 cell lysates. Protein expression was detected using anti-myc antibodies in stably transduced cell lines expressing AIP1-4VHHgp130 variants. (B) Flow cytometric characterization of surface-expressed myc-tagged synthetic receptors in Ba/F3-gp130 cells. Cell surface expression of AIP1-4VHHgp130 variants was detected using anti-myc antibodies followed by fluorophore-conjugated secondary antibodies. Histograms show receptor expression levels in stably transduced cell populations.

Furthermore, cells expressing the AIP3^{VHH}gp130 variant exhibited limited proliferative capacity, achieving only 20% of the maximum proliferation observed with 140 pM HIL-6 (Figure 15 C). In contrast, cells expressing the remaining receptor variants showed no detectable proliferative response under identical conditions. This suggests a fundamental limitation in the ability of these engineered receptors to activate downstream signaling cascades, despite their structural design incorporating key signaling domains. This led to the hypothesis that the distance between the two antigen binding sites, measured in the SAXS model, might exceed the optimal range for effective activation of two synthetic gp130 receptors (Figure 13).

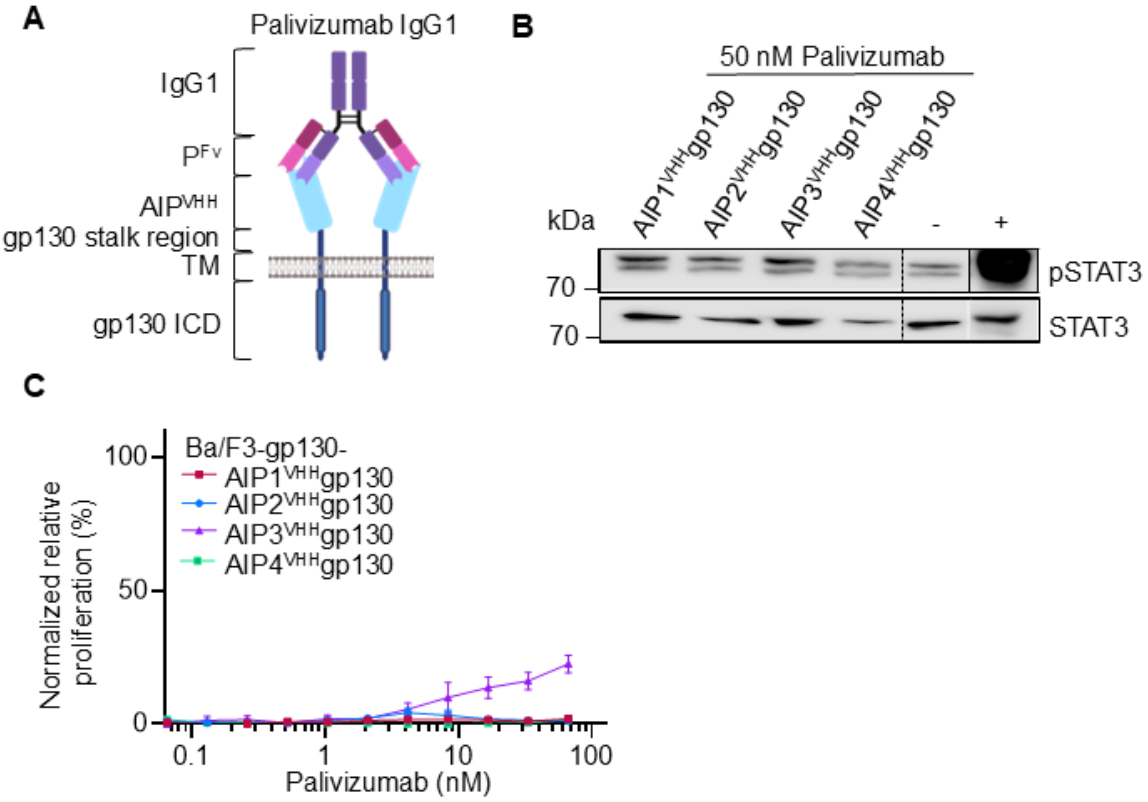

Figure 15: STAT3 Activation and Proliferative Response in AIP1-4VHHgp130-expressing Ba/F3-gp130 Cells.
(A) Schematic depiction of Palivizumab binding to AIP^{VHH}gp130. (B) Analysis of STAT3 phosphorylation in Ba/F3-gp130 cells expressing AIP1-4VHHgp130 variants. Cells were treated for 90 min with either Palivizumab (50 nM), Hyper-IL-6 (HIL-6, 10 ng/ml), or left untreated. Cell lysates (50 µg protein/lane) were analyzed by Western blotting using antibodies specific for phosphorylated STAT3 and total STAT3. Data shown are representative of three independent experiments. (C) Dose-dependent proliferation analysis of Ba/F3-gp130 cells expressing AIP1-4VHHgp130 variants in response to increasing Palivizumab concentrations (0.033-66 nM). Proliferation rates were normalized to the maximal response induced by HIL-6 (10 ng/ml) for each cell line. Data points represent mean values from three biological replicates with error bars indicating standard deviation (S.D.). Results shown are representative of three independent experiments.

4.6 Enhancement of Receptor Activation through Antibody Cross-linking

To overcome the spatial limitations, higher-order multimerization was employed to enhance receptor activation. A strategy utilizing a human Fc-directed monoclonal antibody (hFc-mAb) as a cross-linking agent for Palivizumab was followed. Initial experiments employed a 6:1 molar ratio of cross-linking hFc-mAb to Palivizumab (Figure 16 A). This approach yielded significant results, with Ba/F3-gp130 cells expressing AIP1^{VHH}gp130, AIP2^{VHH}gp130, and AIP3^{VHH}gp130 demonstrated concentration-dependent proliferation with EC50 values of 215

nM, 48.78 nM, and 2.71 nM, respectively. In contrast, Ba/F3-gp130-AIP4^{VHH}gp130 cells showed no proliferative response even at maximum stimulation conditions (Figure 16 B).

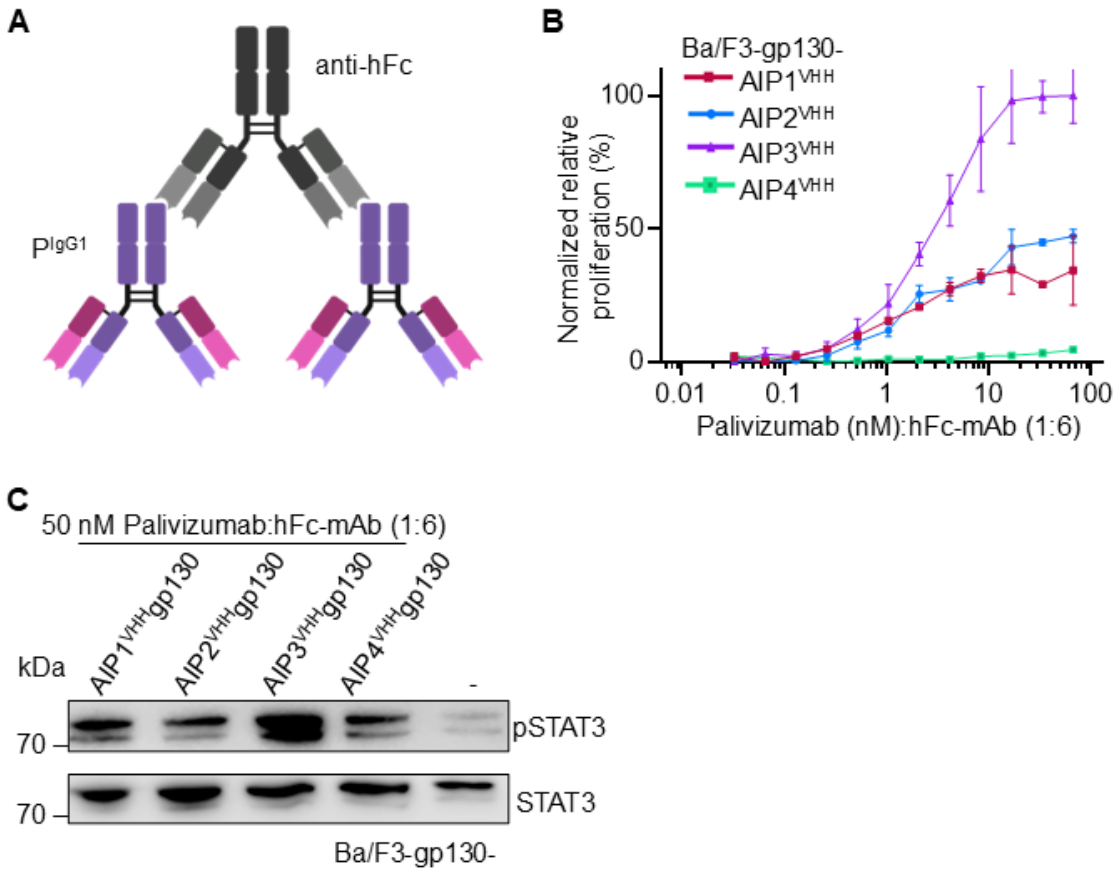

Figure 16: Cross-linked Palivizumab Activates AIP1-3VHHgp130 Synthetic Receptor Signaling.
(A) Schematic depiction of crosslinking of Palivizumab with anti-hFc antibody, showing that the distance between the antigen binding domains of two different antibodies becomes smaller compared to those on the same antibody. (B) Dose-dependent proliferation analysis of Ba/F 3 gp130 cells expressing AIP1-4VHHgp130 variants. Cells were treated with increasing concentrations of Palivizumab (0.033-66 nM) in combination with anti-human Fc antibody (6-fold molar excess). Proliferation rates were normalized to maximal response induced by Hyper-IL-6 (HIL-6, 10 ng/ml) for each cell line. Data points represent mean values from three biological replicates with error bars indicating standard deviation (S.D.). Results shown are representative of three independent experiments. (C) Analysis of STAT3 phosphorylation in Ba/F3-gp130 cells expressing AIP1-4VHHgp130 variants. Cells were treated for 90 min with either Palivizumab (50 nM) plus anti-human Fc antibody (6-fold molar excess), Hyper-IL-6 (HIL-6, 10 ng/ml), or left untreated. Cell lysates (50 µg protein/lane) were analyzed by Western blotting using antibodies specific for phosphorylated STAT3 and total STAT3. Data shown are representative of three independent experiments.

The functional significance of this cross-linking approach was further validated through analysis of STAT3 phosphorylation. Stimulation with 50 nM Palivizumab/hFc-mAb (1:6) induced robust STAT3 phosphorylation in all four Ba/F3-gp130-AIP^{VHH}gp130 cell lines, with particularly strong responses observed in cells expressing AIP1^{VHH}gp130 and AIP3^{VHH}gp130 (Figure 16 C).

4.7 Optimization of Cross-linking Ratios

To determine the optimal conditions for receptor activation, we conducted a systematic analysis of varying Palivizumab:hFc-mAb ratios (1:0, 1:3, 1:6, and 1:12) on AIP1^{VHH}gp130 (Figure 17 A) and AIP3^{VHH}gp130 (Figure 17 B). It was shown that receptor activation was achieved with ratios as low as 1:3 for both cell lines. A ratio of 1:12 ratio proved most effective in inducing cellular proliferation for both tested receptors as well. Furthermore, all tested ratios from 1:3 to 1:12 resulted in sustained STAT3 phosphorylation in Ba/F3-gp130-AIP1/3VHHgp130 cells, indicating robust pathway activation across a range of cross-linking conditions (Figure 17).

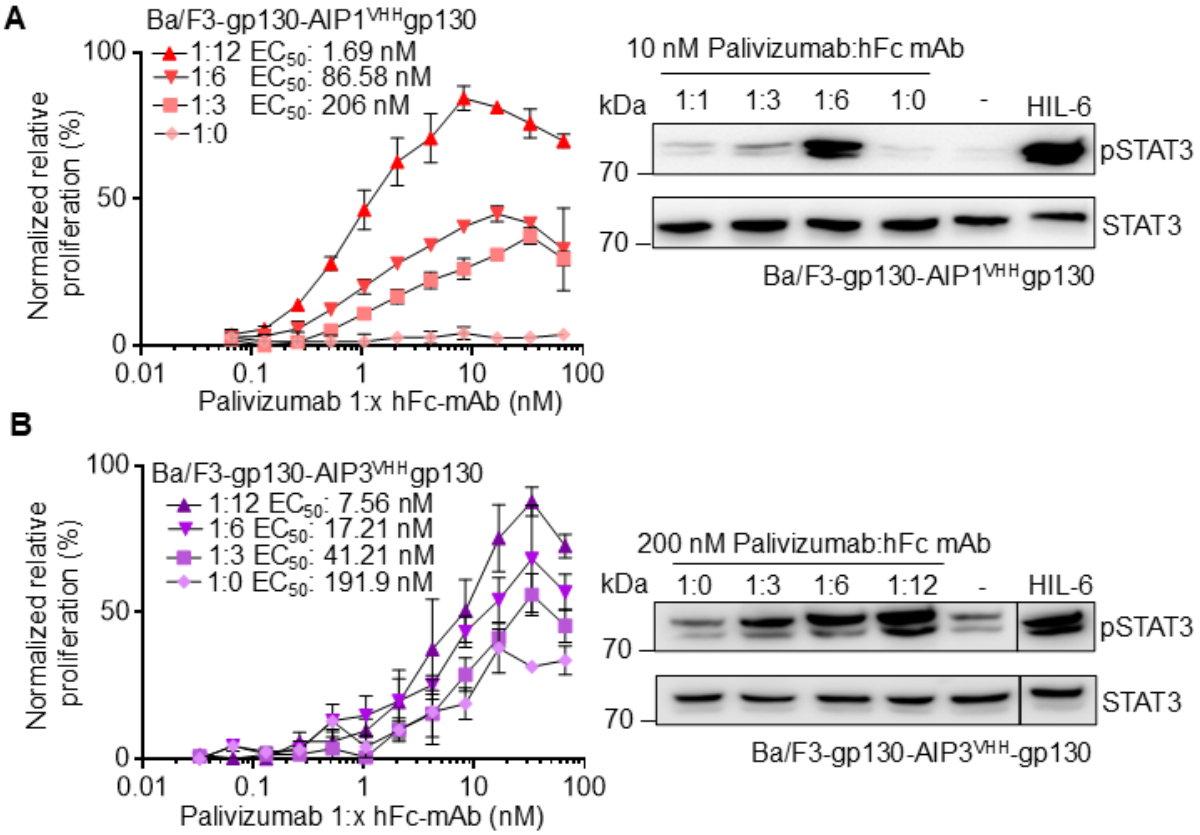

Figure 17: Dose-dependent Effects of Cross-linked Palivizumab on AIP1^{VHH} and AIP3^{VHH} Receptor Variants.
(A, left) Proliferation analysis of Ba/F3-gp130 cells expressing AIP1^{VHH}gp130 in response to varying cross-linking conditions. Cells were treated with increasing Palivizumab concentrations (0.033-66 nM) combined with anti-human Fc antibody at different molar ratios (3-, 6-, and 12-fold excess). Proliferation rates were normalized to Hyper-IL-6 (HIL-6, 10 ng/ml) response. Data represent mean values from three biological replicates with standard deviation (S.D.), shown as one representative experiment from three independent experiments. (A, right) STAT3 phosphorylation analysis in AIP1^{VHH}gp130-expressing Ba/F3-gp130 cells. Cells were stimulated for 90 min with Palivizumab (10 nM) in combination with increasing molar ratios of anti-human Fc antibody (1-, 3-, 6-, and 6-fold excess). Controls included HIL-6 (10 ng/ml) stimulation and untreated cells. Western blotting (50 µg protein/lane) was

performed using phospho-STAT3- and total STAT3-specific antibodies. Results are representative of three independent experiments. (B, left) Proliferation analysis of Ba/F3-gp130 cells expressing AIP3^{VHH}gp130, performed under identical conditions as described in (A). Cells were treated with Palivizumab (0.033-66 nM) and varying concentrations of cross-linking antibody (3-, 6-, and 12-fold molar excess). (B, right) STAT3 phosphorylation analysis in AIP3^{VHH}gp130-expressing Ba/F3-gp130 cells. Experimental conditions matched those in (A), except for higher Palivizumab concentration (200 nM) and different molar ratios of cross-linking antibody (3-, 6-, and 12-fold excess). Western blotting was performed as described above.

This comprehensive structural and functional analysis provides important insights into spatial considerations in designing synthetic receptor systems elucidating synthetic receptor activation mechanisms which are invaluable for future designs and engineering approaches.

4.8 Reformatting Palivizumab into Single-chain Fv Fragments

Palivizumab alone proved to be a poor activator of these synthetic receptors. However, Cross-linking Palivizumab was able to efficiently activate the synthetic AIP1-3VHHgp130 SyCyRs. To reduce the distance between the two epitopes in a more stable way Palivizumab was reformatted into single-chain Fv (scFv) fragment. To be precise, the variable domains of the light and heavy chains were fused via a flexible peptide linker, resulting in two distinct constructs: P^{scFv}LH where the light chain (L) is N-terminal of the heavy chain (H) and P^{scFv}HL where the chains are ordered the opposite way (Figure 18). The sequences can be found in the supplemental information section.

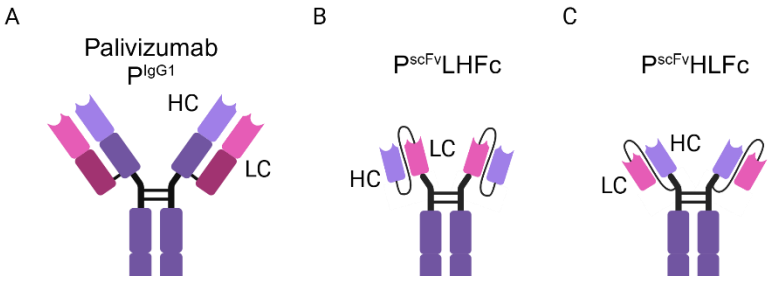

Figure 18:Schematic depiction of reformatted Palivizumab variants.
(A) The original antibody Palivizumab. The fab fragments of the original antibody were transferred to the Fc fused versions using scFv linked by a short GS linker. (B) The scFv is ordered with the light chain (LC) first, followed by a GS linker, followed by the heavy chain (HC) resulting in P^{scFv}LHFc. (C) The scFv is ordered with the HC first, followed by a GS linker, followed by the LC resulting in P^{scFv}HLFc.

The resulting scFvs were fused to Fc-tags in pcDNA vectors resulting in a bivalent ligand, in structure very similar to an antibody. The distance between the variable domains and the first

cysteine of the Fc hinge region was engineered to be 23 and 15 amino acids for $P^{scFv}LH$ and $P^{scFv}HL$, respectively. Molecular modeling analyses predicted that these linker lengths would ensure a maximal distance between the variable domains of approximately 90 and 114 Ångström, respectively, shorter than that of Palivizumab. This strategic design aimed to optimize the spatial distance to emulate that of cross linked Palivizumab in a single synthetic ligand for $AIP^{VHH}gp130$ receptors.

The $P^{scFv}LHFc$ and $P^{scFv}HLFc$ fusion proteins, containing the scFv fragments and an IgG1 Fc domain, were expressed in transiently transfected Expi293F™ cells. The dimeric constructs were then purified from the cell culture supernatants via Protein A affinity chromatography (Figure 19 and Figure 20, respectively). Purification yields for both proteins were good and a small batch of 30 ml supernatant was sufficient.

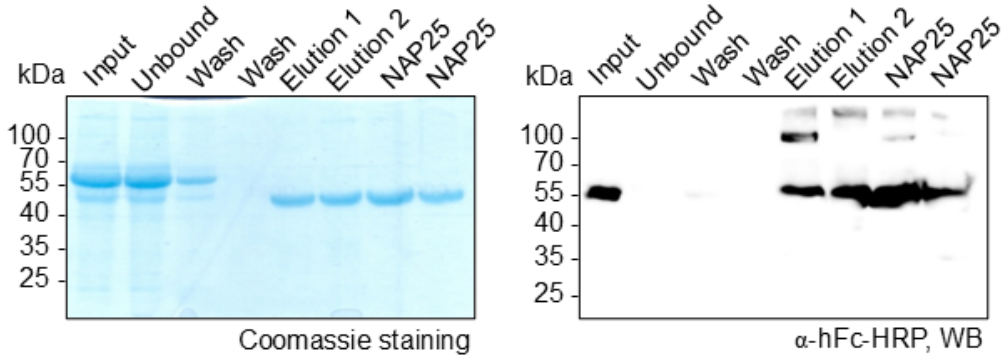

Figure 19: Purification of PscFvLHFc
On the left a Coomassie gel of the purification showing single bands after elution, indicating high purity. On the right is the same sample after Western blotting with an a-hFc-HRP antibody, showing only a single band after purification, indicating little or no degradation.

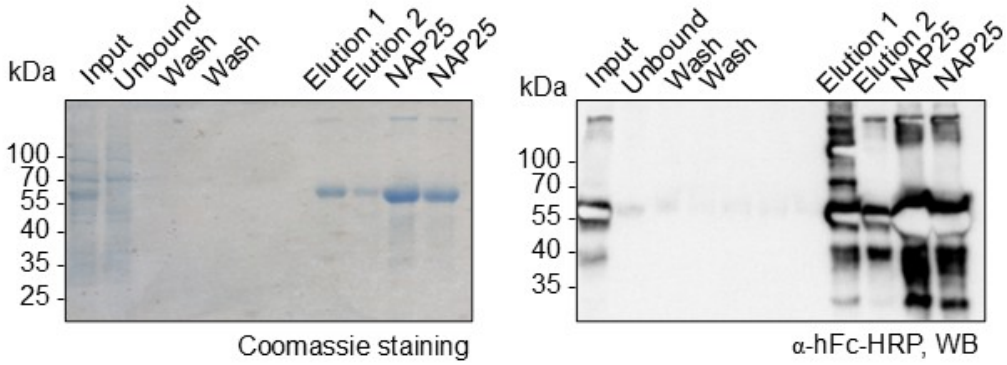

Figure 20: Purification of PscFvHLFc
On the left a Coomassie gel of the purification showing single bands after elution, indicating high purity. On the right is the same sample after Western blotting with an a-hFc-HRP antibody, showing only a single band after purification, indicating little or no degradation

4.9 Binding Affinity of the Palivizumab scFv-Fc fusion proteins to AIP1^{VHH}

To validate the successful reformatting of Palivizumab, we determined the binding affinities of the P^{scFv}LHFc and P^{scFv}HLFc proteins to the high-affinity anti-idiotypic nanobody AIP1^{VHH} using surface plasmon resonance. Interestingly, AIP1^{VHH} exhibited comparable binding affinities to the P^{scFv}LHFc (KD = 9.80 pM) (Figure 21 A), and P^{scFv}HLFc (KD = 27.18 pM) (Figure 21 B), when compared to the parental Palivizumab antibody (KD = 25.97 pM). Confirming successful reformatting of Palivizumab into scFv fragments without compromising the high-affinity interaction with AIP1^{VHH}.

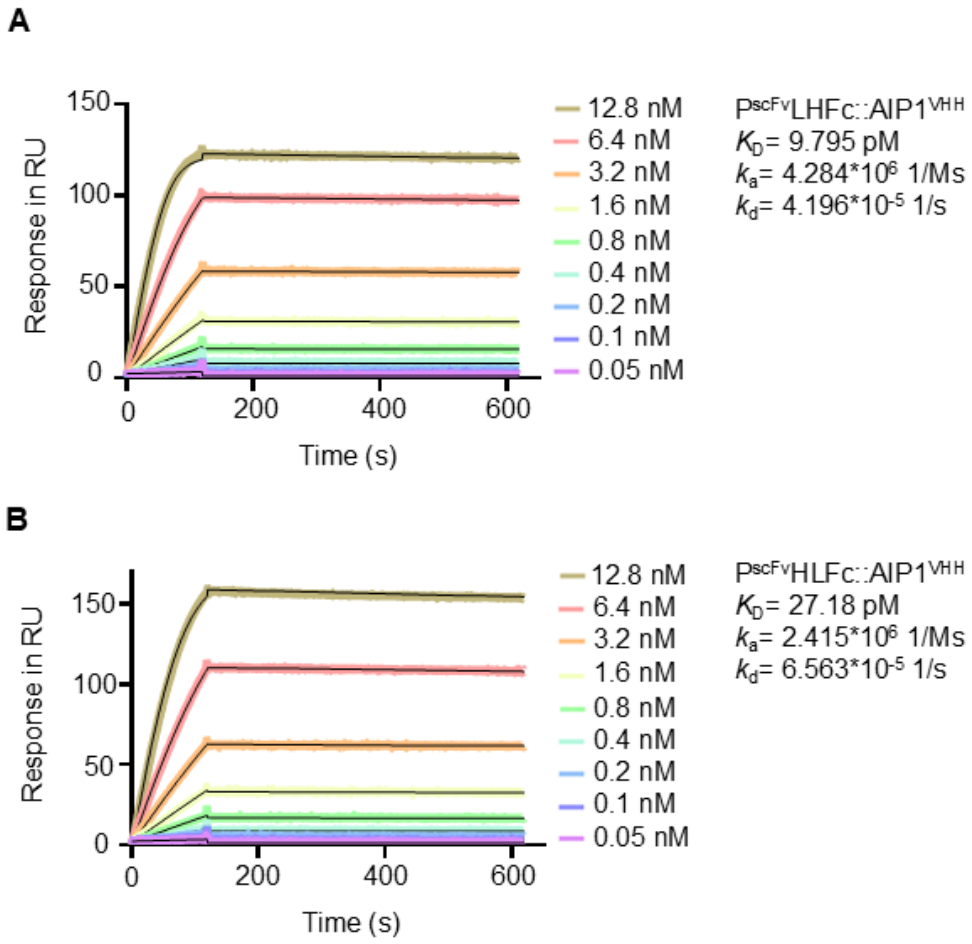

Figure 21: Binding Analysis of Reformatted Palivizumab scFv Variants to AIP1^{VHH}.
(A-B) Surface plasmon resonance analysis of the P^{scFv}LHFc fusion protein (light chain-heavy chain orientation). Schematic representation of the protein architecture and corresponding binding kinetics. SPR sensorgrams show binding of soluble AIP1^{VHH} at nine concentrations (0.05-12.8 nM) to P^{scFv}LHFc captured on a Protein A chip. (C-D) Analogous analysis of the P^{scFv}HLFc fusion protein (heavy chain-light chain orientation) under identical experimental conditions. For all measurements, colored lines represent experimental data in response units (RU), while black lines indicate the global kinetic fit. Association kinetics were recorded during 120-second analyte injection, followed by a 500-second dissociation phase. Concentration series were prepared using two-fold dilutions.

4.10 Activation of AIP1^{VHH}gp130 Receptor by Palivizumab scFv Fc fusion proteins

Both dimeric P^{scFv}LHFc and P^{scFv}HLFc proteins were tested on Ba/F3-gp130-AIP^{VHH}gp130 cells (Figure 22 A). Both were able to activate the SyCyR in a dose dependent manner (Figure 22 B) with an EC_{50} of 0.38 nM and 0.50 nM respectively, being in a very similar range.

Both P^{scFv}Fc variants were highly effective in inducing sustained proliferation and STAT3 phosphorylation of Ba/F3-gp130-AIP1^{VHH}gp130 cells at a range from 1.5-6 nM for P^{scFv}LHFc and as low as 0.19-6 nM for P^{scFv}HLFc, indicating robust receptor activation (Figure 22 C).

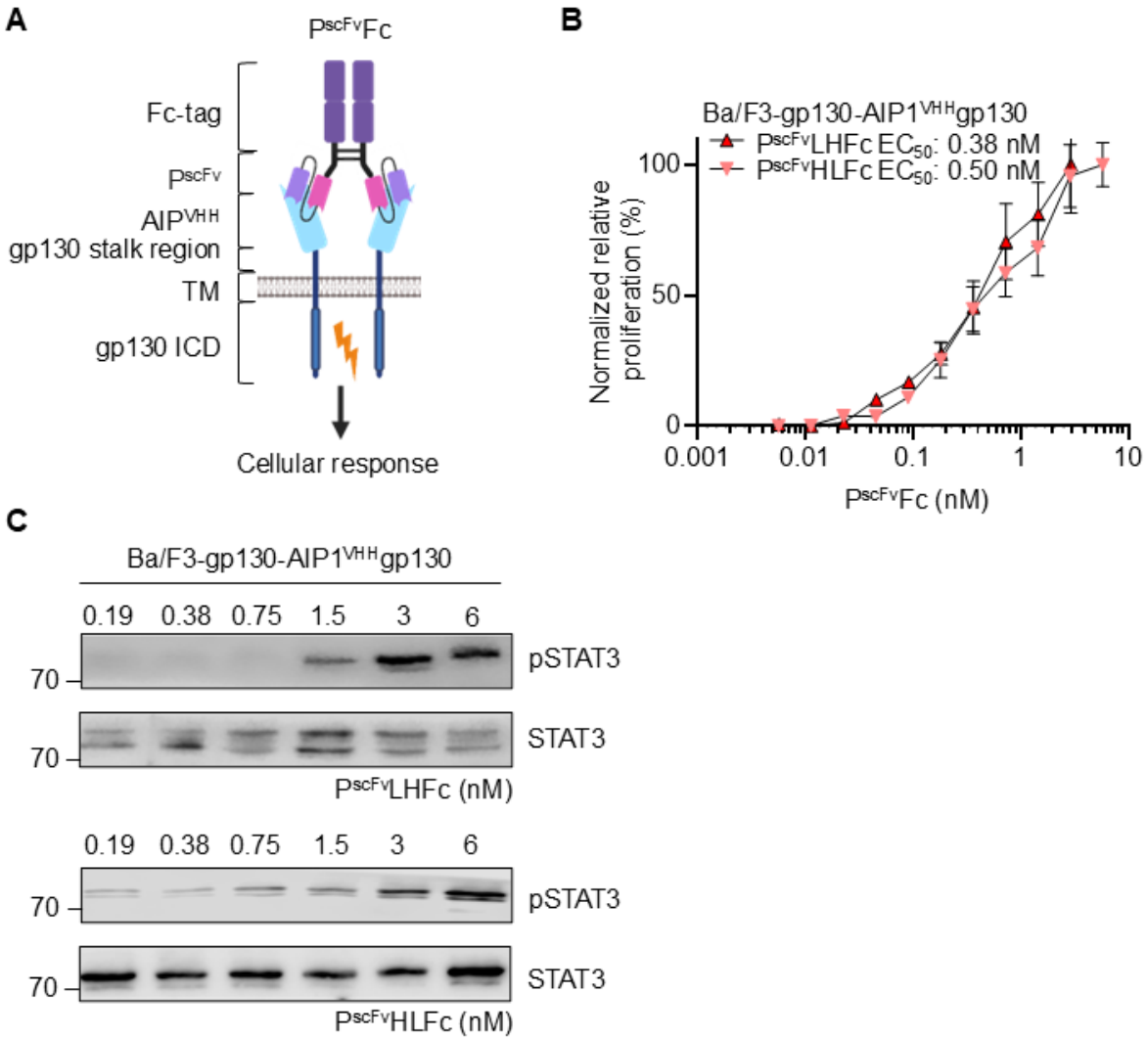

Figure 22: Analysis of P^{scFv}Fc Variants as Synthetic AIP^{VHH}gp130 Receptor Activators
(A) Schematic depiction of P^{scFv}LHFc bound to AIP^{VHH}gp130. (B) Dose-dependent proliferation of Ba/F3-gp130 cells expressing AIP1^{VHH}gp130. Cells were treated with increasing concentrations (0.00563-5.77 nM) of either P^{scFv}LHFc or P^{scFv}HLFc. Proliferation rates were normalized to maximal response induced by Hyper-IL-6 (HIL-6, 10 ng/ml). Data points represent mean values from three biological replicates with error bars indicating standard deviation (S.D.). Results shown are representatives of three independent experiments. (C) Analysis of STAT3 phosphorylation in Ba/F3-gp130-AIP1^{VHH}gp130 cells induced with increasing concentrations of P^{scFv}LHFc or P^{scFv}HLFc (0.19-6 nM) for 90 min. Cell lysates (50 µg protein/lane) were analyzed by Western blotting using antibodies specific for phosphorylated STAT3 and total STAT3. Data shown are representative of three independent experiments.

4.11 Activation of AIP^{VHH}gp130 Receptors by P^{scFv}LHFc

P^{scFv}LHFc was then tested on the Ba/F3-gp130 cells expressing the 4 different AIP^{VHH}gp130 variants. The ligand induced both cellular proliferation and STAT3 phosphorylation at a concentration of 10 nM showing the strongest activation in the AIP1^{VHH}gp130, followed by AIP3^{VHH}gp130 expressing cells (Figure 23). Dose-response analysis revealed an EC_{50} of 0.21 nM for the AIP1^{VHH}gp130 SyCyR, and 6.61 nM for the AIP3^{VHH}gp130 SyCyR (Figure 23 A). In contrast, Ba/F3-gp130/AIP2^{VHH}gp130 cells were barely activated by P^{scFv}LHFc, while cells expressing AIP4^{VHH}gp130 failed to proliferate with any ligand. Ba/F3-gp130 expressing either AIP2^{VHH}gp130 or AIP4^{VHH}gp130 did not show any phosphorylation after stimulation (Figure 23 B).

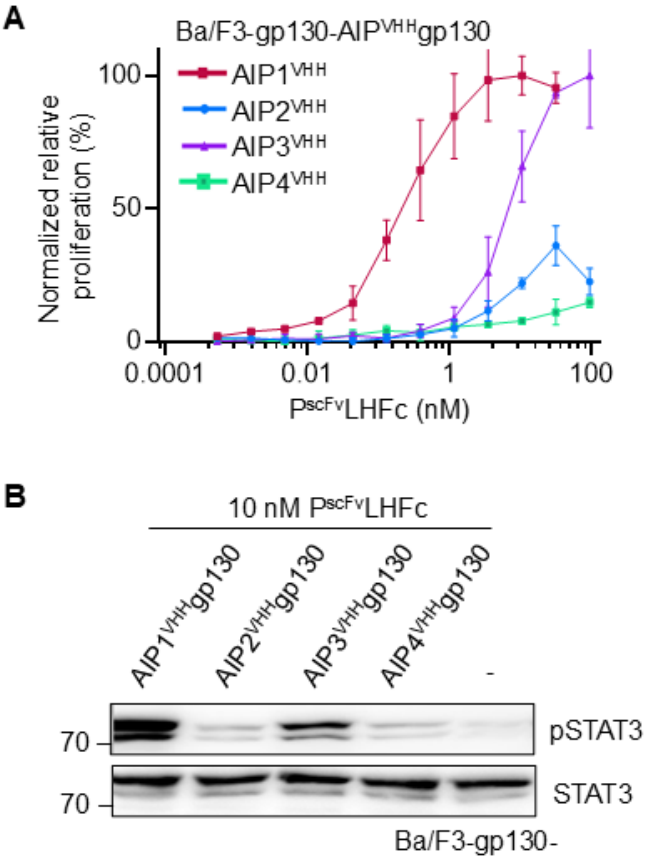

Figure 23: P^{scFv}Fc are effective activators of synthetic AIP^{VHH}gp130 receptors.
(A) Dose-dependent proliferation of Ba/F3-gp130 cells expressing AIP1-4VHHgp130 in response to P^{scFv}LHFc treatment (concentration range: 0.00053-93.5 nM). Proliferation rates were normalized to maximal response induced by HIL-6 (10 ng/ml) for each stable cell line. Data represent mean ± SD from three biological replicates of one representative experiment out of three independent experiments. **(B)** Western blotting analysis of STAT3 phosphorylation in Ba/F3-gp130 cells expressing AIP1-4VHHgp130 following a 90-min treatment with 10 nM P^{scFv}LHFc or vehicle control.

Activation of AIP^{VHH}gp130 Receptors by P^{scFv}HLFc

The alternative heavy/light chain ordered protein, P^{scFv}HLFc was also evaluated for its ability to activate the synthetic AIP^{VHH}gp130 receptors.

Interestingly, the P^{scFv}HLFc fusion protein demonstrated distinct activation profiles compared to P^{scFv}LHFc. For the AIP1^{VHH}gp130 and AIP3^{VHH}gp130 variants, P^{scFv}HLFc induced proliferation with EC_{50} values of 0.4 nM and 9.1 nM, respectively (Figure 24 A). Notably, Ba/F3-gp130 cells expressing AIP2^{VHH}gp130 exhibited a higher proliferative response to P^{scFv}HLFc with an EC50 of 0.7 nM, in stark contrast to P^{scFv}LHFc which was not responsive (Figure 23 A). The STAT3 phosphorylation analysis further corroborated these findings. Stimulation with 10 nM P^{scFv}HLFc resulted in the strongest activation of the AIP2^{VHH}gp130 cells, followed by the AIP1^{VHH}gp130 and AIP3^{VHH}gp130 variants (Figure 24 B).

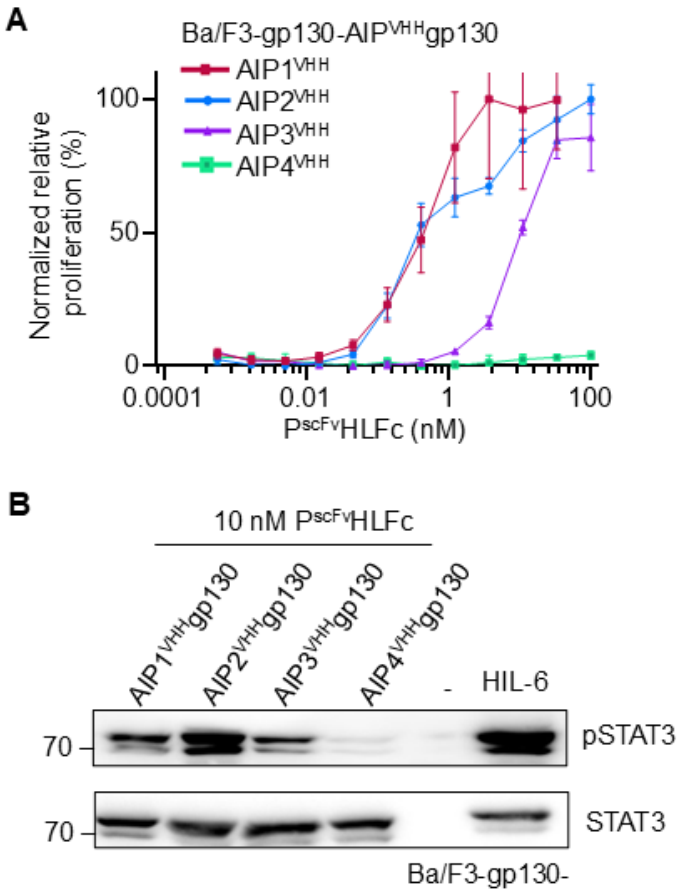

Figure 24: P^{scFv}Fc are effective activators of synthetic AIP^{VHH}gp130 receptors.
(A) Dose-dependent proliferation analysis of Ba/F3-gp130 cells expressing AIP1-4^{VHH}gp130 in response to P^{scFv}HLFc treatment (concentration range: 0.00056-100 nM). Proliferation rates were normalized to maximal response induced by HIL-6 (10 ng/ml) for each stable cell line. **(B)** Western blotting of STAT3 phosphorylation in Ba/F3-gp130 cells expressing AIP1-4^{VHH}gp130 following a 90-min treatment with either 10 nM P^{scFv}HLFc or HIL-6 (10 ng/ml).

4.12 Influence of crosslinking PscFvLHFc on Activation

AIP1^{VHH}gp130 and AIP3^{VHH}gp130 variants were proliferative under P^{scFv}LHFc and were chosen to further analyse the effect of cross-linking in varying P^{scFv}LHFc:hFc-mAb ratios (1:0, 1:3, 1:6, and 1:12). The proliferation assays revealed that P^{scFv}LHFc induced an EC50 of 0.24-0.42 nM in the Ba/F3-gp130-AIP1^{VHH}gp130 cells independent of cross-linking ratio (Figure 25 A), which is also shown in STAT3 phosphorylation analysis, showing no increase in phosphorylation (Figure 25 B). These finding were similar to the EC_{50} of 1.24-3.16 nM observed for Ba/F3-gp130-AIP3^{VHH}gp130 cells (Figure 25 C), where also no increase in activation of STAT3 phosphorylation after cross-linking at any concentration was observed (Figure 25 D).

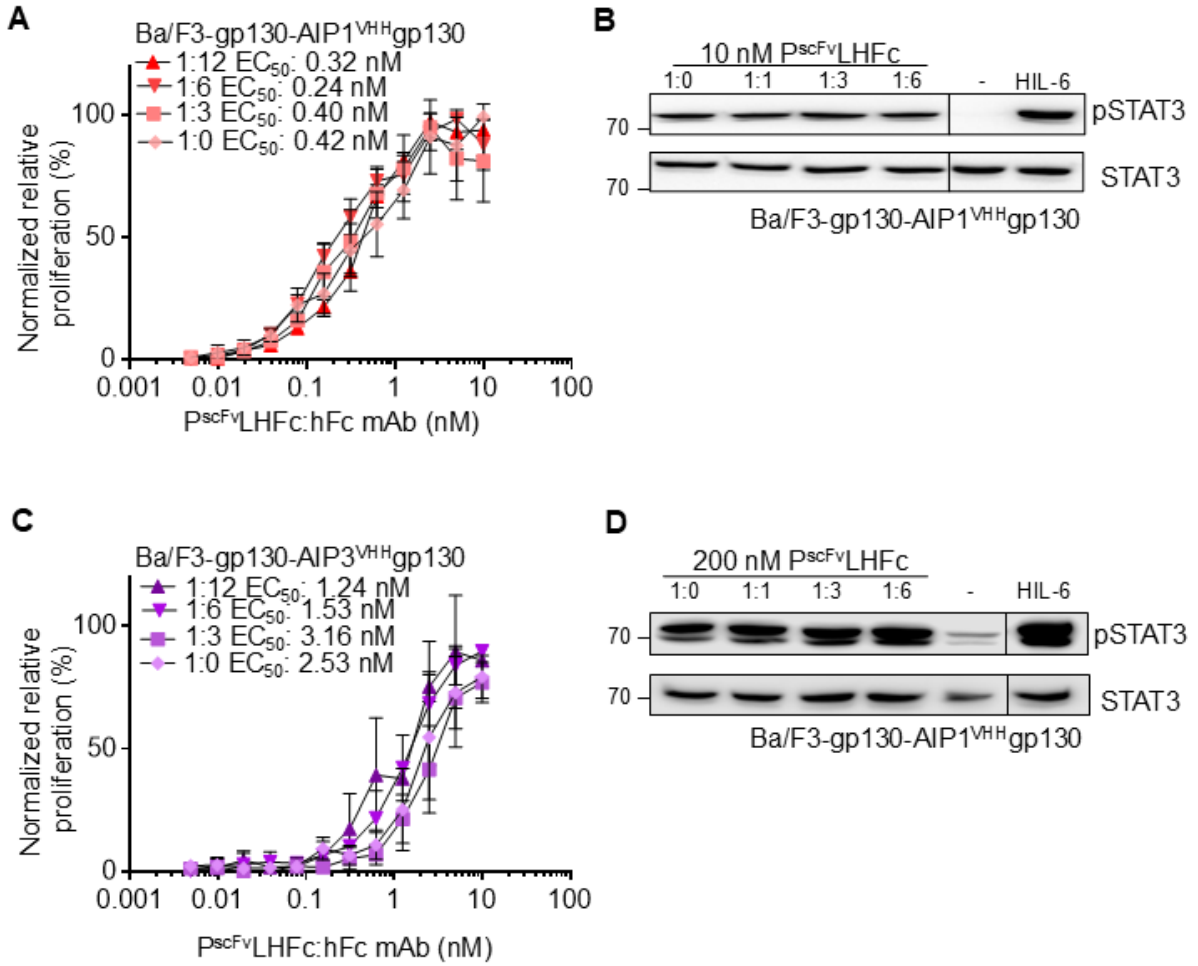

Figure 25: P^{scFv}Fc are effective activators of synthetic AIP^{VHH}gp130 receptors without cross-linking.
(A) Dose-dependent proliferation analysis of Ba/F3-gp130 cells expressing AIP1^{VHH}gp130 in response to P^{scFv}LHFc (0.0049-10 nM) in the presence of hFc-mAb at 3-, 6-, and 12-fold molar excess. Proliferation rates were normalized to maximal response induced by HIL-6 (10 ng/ml) for each cell line. Data represent mean ± SD from three biological replicates of one representative experiment out of three independent experiments. **(B)** Western blotting analysis of STAT3 phosphorylation in Ba/F3-gp130 cells expressing AIP1^{VHH}gp130 after 90 min treatment with 10 nM P^{scFv}LHFc in the presence of 1-, 3-, and 6-fold molar excess of hFc-mAb, HIL-6 (10 ng/ml), or vehicle control. Total protein loading was 50 µg per lane. Phospho-STAT3 and total STAT3 were detected using specific antibodies. Representative blot from three independent experiments. **(C)** Dose-dependent proliferation analysis of Ba/F3-gp130 cells expressing AIP3^{VHH}gp130 in response to P^{scFv}LHFc (0.0049-10 nM) in the presence of hFc-mAb at 3-, 6-, and 12-fold molar excess. Proliferation rates were normalized to maximal response induced by HIL-6 (10 ng/ml) for each cell line. Data represent mean ± SD from three biological replicates of one representative experiment out of three independent experiments. **(D)** Western blotting of STAT3 phosphorylation in Ba/F3-gp130 cells expressing AIP3^{VHH}gp130 after 90 min treatment with 200 nM P^{scFv}LHFc in the presence of 1-, 3-, and 6-fold molar excess of hFc-mAb, HIL-6 (10 ng/ml), or vehicle control. Total protein loading was 50 µg per lane. Phospho-STAT3 and total STAT3 were detected using specific antibodies. Representative blot from three independent experiments.

4.13 P^{scFv}LHFc specifically activate STAT3 via gp130 signaling through SyCyRs

To validate the specificity of the STAT3 activation, we employed the pan-JAK inhibitor P6 (*141*), which effectively suppressed the P^{scFv}Fc-induced STAT3 phosphorylation in the Ba/F3-gp130-AIP1^{VHH}gp130 cells (Figure 26).

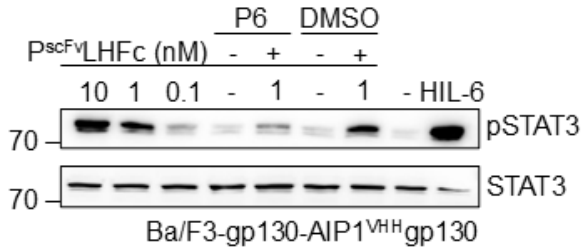

Figure 26: Inhibitor analysis of STAT3 phosphorylation in Ba/F3-gp130-AIP1^{VHH}gp130 cells. Cells were treated for 90 min with P^{scFv}LHFc at three concentrations (0.1, 1, and 10 nM) in the presence or absence of P6 inhibitor (10 µM). Additional conditions included HIL-6 stimulation (10 ng/ml), DMSO vehicle control (1% v/v), and untreated cells. STAT3 phosphorylation was analyzed as described above.

This finding confirmed that the STAT3 activation was mediated specifically through the JAK/STAT signaling pathway following the activation of the AIP1^{VHH}gp130 synthetic receptor.

4.14 Competitive Inhibition of P^{scFv}LHFc induced activation by Palivizumab

Competition experiments to elucidate the functional dynamics using a constant concentration of P^{scFv}LHFc and increasing amounts of the Palivizumab IgG1 antibody (Figure 27 A). The addition of Palivizumab resulted in a dose-dependent suppression of the P^{scFv}LHFc-induced AIP1^{VHH}-gp130 receptor activation. The calculated IC_{50} for this inhibition was 8.28 nM, indicating that a 4-fold molar excess of Palivizumab over P^{scFv}LHFc (2 nM) was sufficient to fully block activation of AIP1^{VHH}-gp130 (Figure 27 B).

This competitive inhibition was also evident in the analysis of STAT3 phosphorylation, where at least an 8-fold molar excess of Palivizumab over P^{scFv}LHFc (2 nM) was required to achieve complete suppression of the signal transduction in Ba/F3-gp130-AIP1^{VHH}gp130 cells (Figure 27 C).

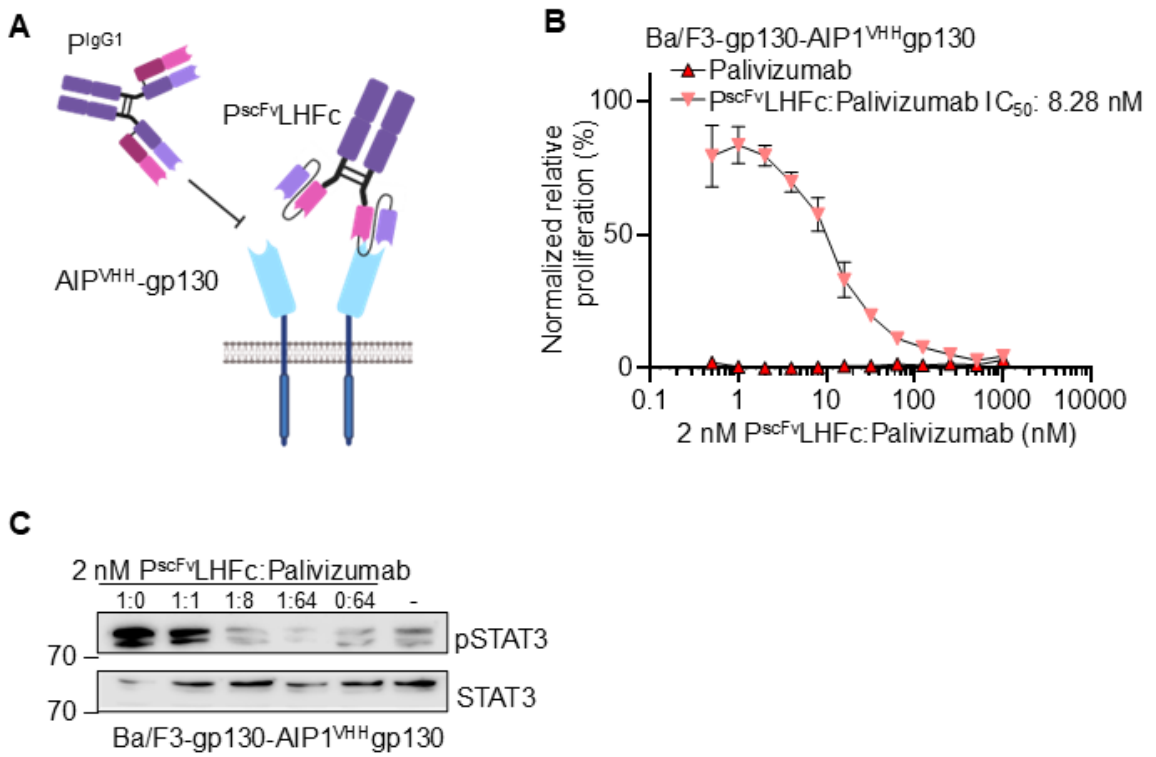

Figure 27:Competition of Palivizumab and P^{scFv} inhibits synthetic AIP1^{VHH}gp130 signaling. **(A)** Scheme depicting the mechanism of P^{IgG1} inhibiting P^{scFv}LHFc **(B)** Proliferation analysis of Ba/F3-gp130 cells expressing AIP1^{VHH}gp130 treated with 1.8 nM P^{scFv}LHFc in the presence of increasing Palivizumab concentrations (0.49-1000 nM). Proliferation rates were normalized to HIL-6 (10 ng/ml) response. Cells treated with Palivizumab alone served as negative control. Data represent mean ± SD from three biological replicates of one representative experiment out of three independent experiments. **(C)** Western blotting of STAT3 phosphorylation in Ba/F3-gp130 cells expressing AIP1^{VHH}gp130 following 90 min treatment with 2 nM P^{scFv}LHFc in the presence of 0-, 1-, 8-, and 64-fold molar excess of Palivizumab or vehicle control. Total protein loading was 50 µg per lane. Phospho-STAT3 and total STAT3 were detected using specific antibodies. Representative blot of three independent experiments.

Our findings demonstrate two key aspects of Palivizumab (IgG1) interaction with the engineered receptor system. First, while Palivizumab binds to the receptor, it does not induce activation. Second, this binding sterically prevents P^{scFv}Fc from accessing the receptor binding sites. This feature provides a valuable safety mechanism, as it enables rapid inactivation of the system in clinical settings should emergency intervention become necessary.

4.15 Inhibitory Potential of Monomeric AIP^{VHH}s

Another way to implement this safety mechanism is to employ the inhibitory potential of the monomeric AIP^{VHH}s against the P^{scFv}LHFc-induced activation of the synthetic AIP1^{VHH}gp130 receptor by binding of AIP^{VHH} to the ligand preventing it from binding to the receptors (Figure 28 A). The high-affinity AIP1^{VHH} exhibited the most potent inhibitory effect, with an IC$_{50}$ of 2.79 nM and thus the only one able to outcompete and effectively block the

P^{scFv}LHFc-induced activation. In contrast, $AIP2^{VHH}$ and $AIP3^{VHH}$ required higher inhibitory concentrations, with IC_{50} values of 83.14 nM and 364.40 nM, respectively to even have a small effect. Interestingly, $AIP4^{VHH}$, which displayed the weakest binding affinity, did not function as an effective antagonist, likely due to its high dissociation rate (k*d*) compared to $AIP2^{VHH}$ and $AIP3^{VHH}$ (Figure 28 B).

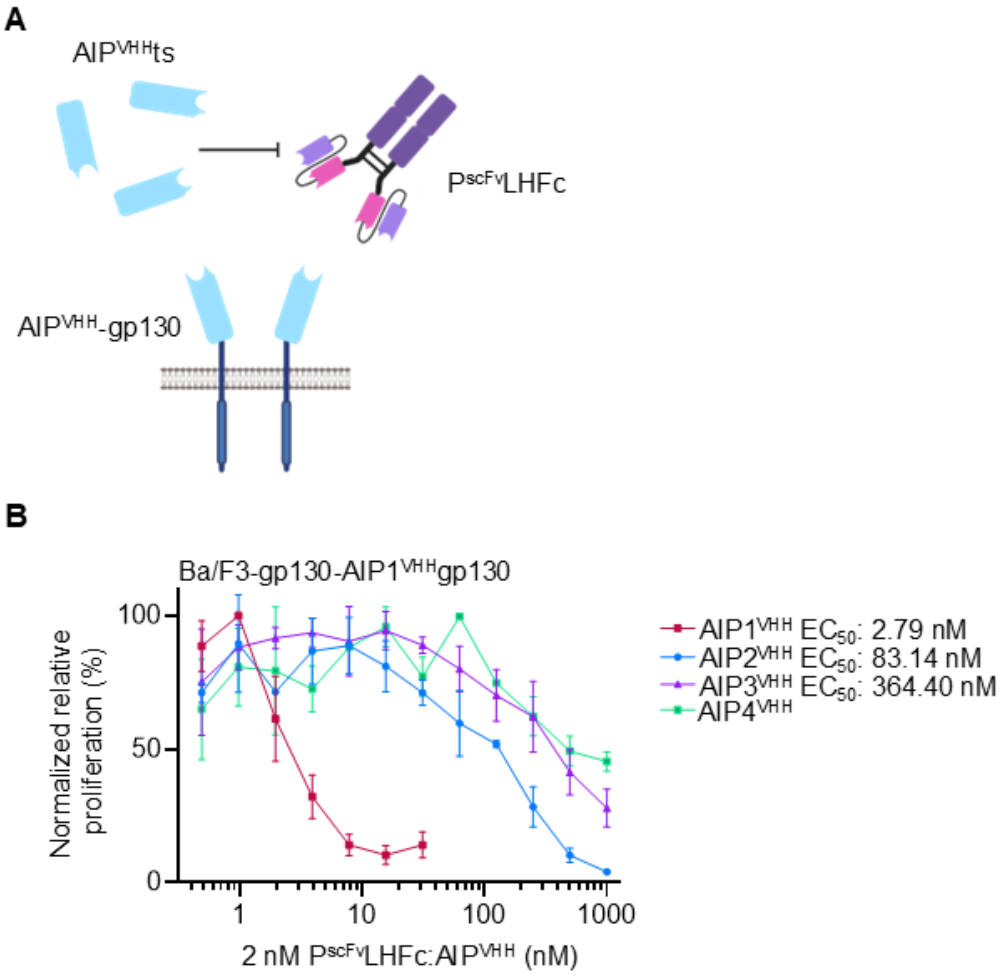

Figure 28:Palivizumab and P^{scFv} inhibit synthetic $AIP1^{VHH}$gp130 signaling.
(A) Schematic depiction of soluble AIP^{VHH} nanobodies inhibiting P^{scFv}LHFc **(B)** Proliferation of Ba/F3-gp130 cells expressing $AIP1^{VHH}$gp130 was assessed in the presence of increasing concentrations of soluble AIP1-4VHH (0.49 to 1000 nM) and a fixed concentration of P^{scFv}LHFc (2 nM). Cell proliferation was normalized to that induced by IL-6 (10 ng/ml). Data represent mean ± SD from three biological replicates of one representative experiment out of three independent experiments.

4.16 Optimization of signaling efficacy through stalk region deletion

After engineering Palivizumab into a functional ligand the role of the stalk region in the synthetic AIP^{VHH}gp130 constructs was further investigated in an attempt to enable activation by Palivizumab IgG1. The original receptor design included a 6-amino acid stalk region

(AQGEIE) derived from the gp130 protein, which was positioned between the AIP^{VHH} domain and the transmembrane domain to provide some flexibility in the positioning of the binding domain (Figure 29).

It was hypothesized that the deletion of this stalk region might influence the positioning, rigidity, and ultimately, the signaling activation. To test this, we generated AIP^{VHH}gp130 variants with the complete deletion of the stalk region, designated as AIP1-4VHHgp130Δstalk. The sequences of the deletion variants can be found in the supplemental information section.

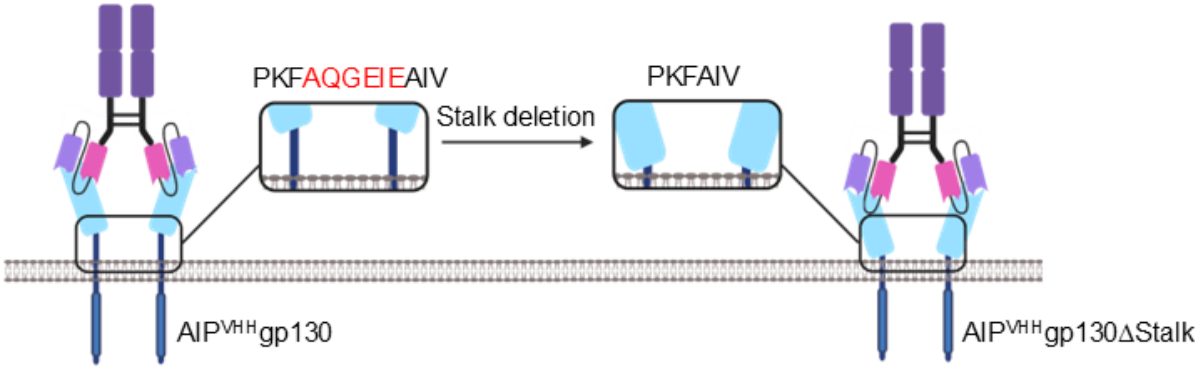

Figure 29:Schematic depiction of transformation of AIP^{VHH}gp130 to AIP^{VHH}gp130Δstalk variants.
The stalk region (with its AA sequence marked in red) that is native to the gp130 receptor was deleted, this shortens the distance and possibly changes the orientation of the intracellular part of the receptor upon binding. The depiction a cartoon, and not true to scale.

4.17 Expression and Surface Localization of stalk-deleted AIP^{VHH}gp130 Receptors

Analysis of the surface expression of the AIP^{VHH}gp130Δstalk variants in transduced Ba/F3-gp130 cells revealed some notable differences compared to the original constructs. While the expression of the AIP1^{VHH}gp130Δstalk receptor was decreased compared to the non-deletion variant, in contrast the deletion of the stalk region resulted in higher expression levels for the AIP3-4VHHgp130Δstalk variants, while AIP2^{VHH}gp130Δstalk remained on a similar level (Figure 30).

This observation suggested that the stalk region might have a differential impact on the expression and surface localization of the various AIP^{VHH}gp130 receptors. As the expression levels can influence the receptor activation thresholds and dynamics, these differences could contribute to the distinct functional behaviors observed among the variants. However, the activation of the signaling cascade can occur even with low surface expression of the receptors.

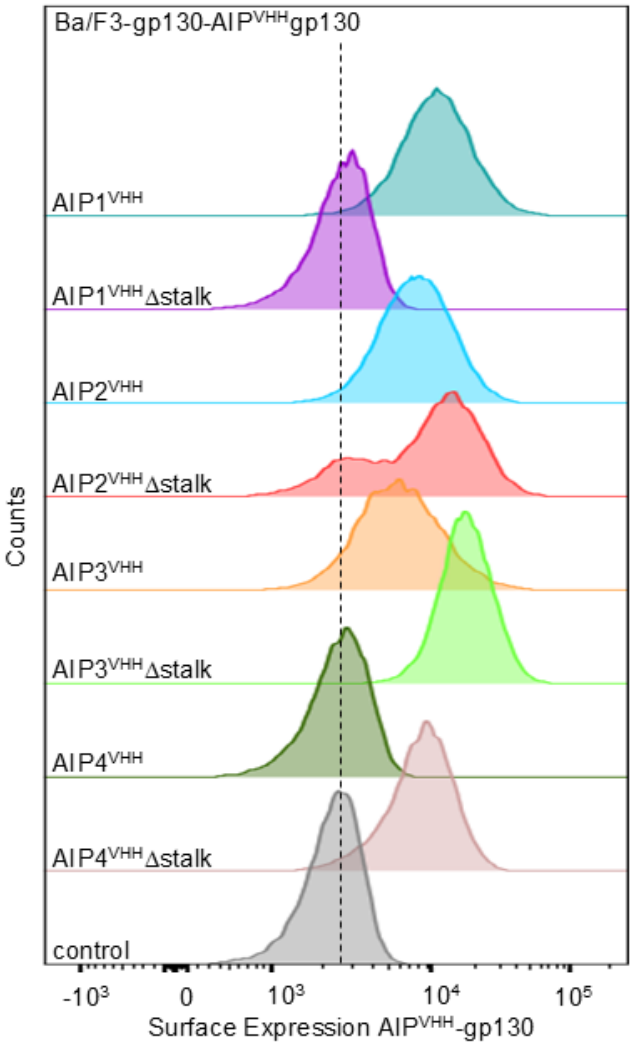

Figure 30: FACS analysis of surface expression.
Flow cytometric analysis of myc-tagged synthetic receptors on Ba/F3gp130 cells expressing AIP1-4VHH-gp130 and AIP1-4^{VHH}gp130ΔStalk.

4.18 Activation of stalk-deleted AIP^{VHH}gp130 Receptors by P^{scFv}LHFc

After establishing the Ba/F3-gp130 cell lines expressing AIP^{VHH}gp130 receptors with and without stalk region deletion a functional analysis of the activation of the synthetic AIP^{VHH}gp130 receptors by the P^{scFv}LHFc ligand was conducted. Consistent with previous findings, the P^{scFv}LHFc stimulus effectively activated the newly transduced AIP1^{VHH}gp130 (EC50 = 0.15 nM) and AIP3^{VHH}gp130 (EC50 = 39.07 nM) variants in the Ba/F3-gp130 cells. AIP1^{VHH}gp130Δstalk on the other hand was not able to induce proliferation of Ba/F3-gp130 cells, while AIP3^{VHH}gp130 with an EC50 of 6.07 nM was more potent than its full-length counterpart. Interestingly, the deletion of the stalk region rendered the previously inactive AIP2^{VHH}gp130, with EC50 value of 18.31 nM into an active receptor. AIP4^{VHH}gp130 and its stalk deletion variant AIP4^{VHH}gp130Δstalk were both unresponsive (Figure 31).

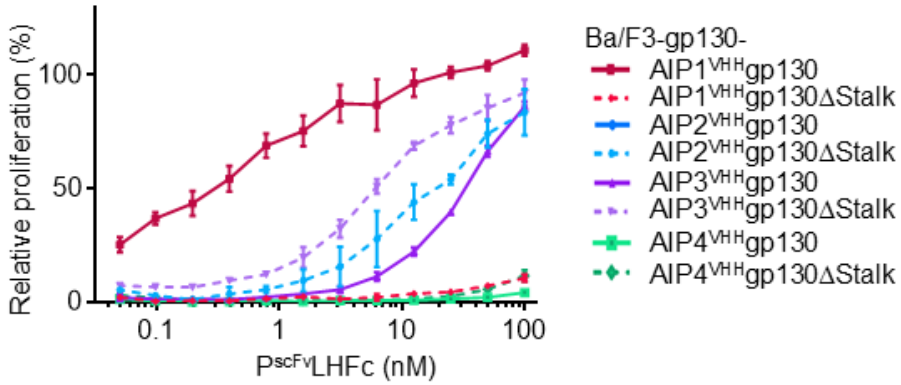

Figure 31: P^{scFv}LH23Fc activates AIP^{VHH}gp130 different than AIP^{VHH}gp130Δstalk.
(A) Dose-dependent proliferation of Ba/F3-gp130 cells expressing AIP1-4VHHgp130 and AIP1-4VHHgp130Δstalk in response to P^{scFv}LH23Fc (0.05-300 nM). Proliferation was normalized to HIL-6 (10 ng/ml) induced proliferation for each cell line. Data represent mean ± S.D. of three biological replicates from one representative experiment out of three.

This activation pattern was further corroborated by the analysis of STAT3 phosphorylation, where the full-length AIP1^{VHH}gp130 (Figure 32 A), stalk-deleted AIP2^{VHH}gp130Δstalk (Figure 32 B) and AIP3^{VHH}gp130Δstalk (Figure 32 C) variants as well as the full-length AIP3^{VHH}gp130 (Figure 32 C) exhibited robust STAT3 activation in response to P^{scFv}LHFc after 45 min of stimulation at concentrations of 75 nM, 19 nM and 75 nM and above respectively, mirroring the proliferative responses.

In agreement with proliferation assays AIP2^{VHH}gp130 remained unresponsive to the P^{scFv}LHFc stimulus, underscoring the complex and receptor-specific nature of the impact of the stalk region deletion (Figure 32 B).

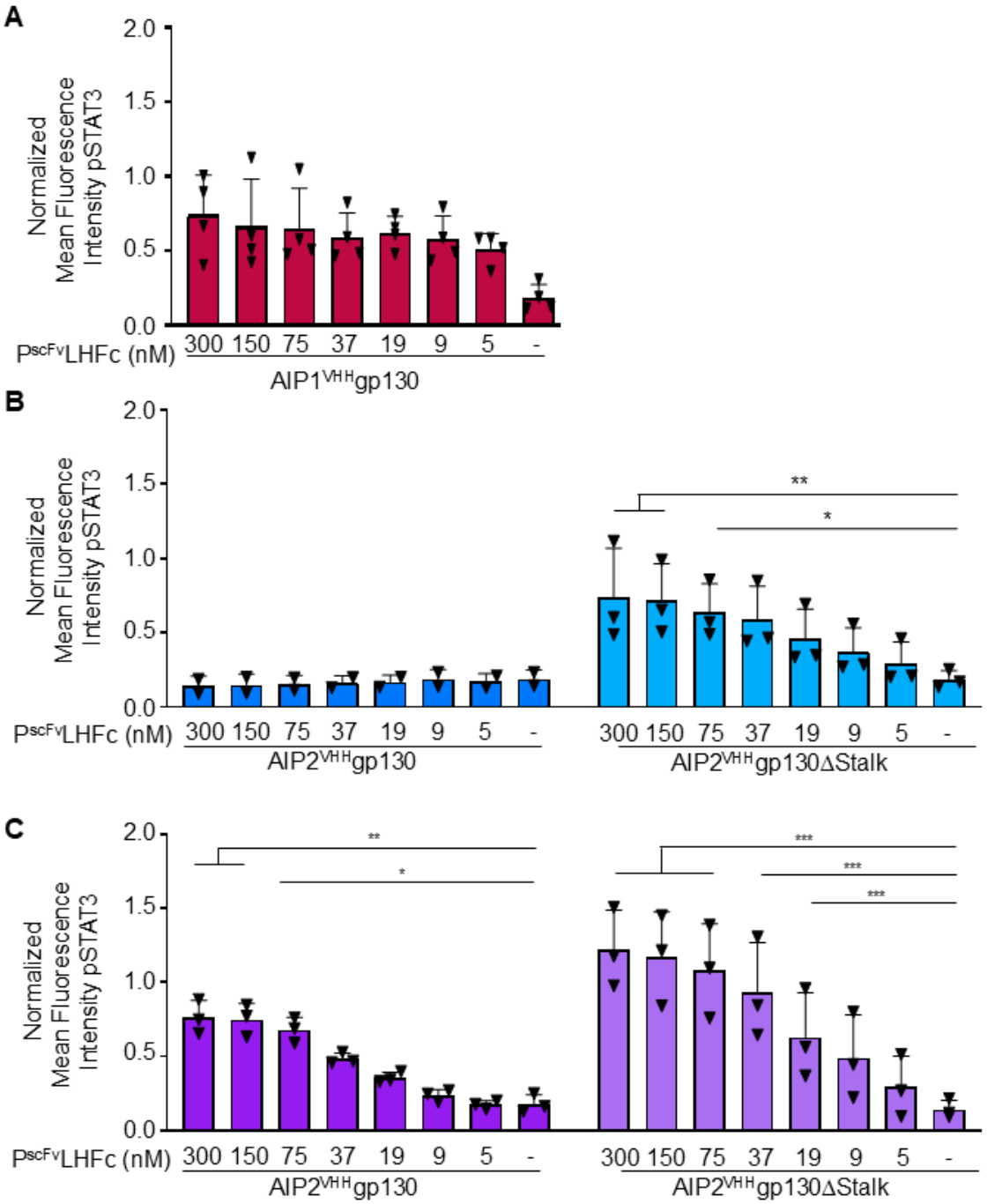

Figure 32: P^{scFv}LH23Fc activates AIP^{VHH}gp130 different than AIP^{VHH}gp130Δstalk. Normalized Mean Fluorescence Intensity of STAT3 phosphorylation in response to 45 min of incubation with P^{scFv}LHFc (5-300 nM) for (A) AIP1^{VHH}gp130, (B) AIP2^{VHH}gp130 and AIP2^{VHH}gp130Δstalk, (C) AIP3^{VHH}gp130 and AIP3^{VHH}gp130Δstalk. Data represent mean ± S.D. of three biological replicates (n=3).

4.19 Changing the linker peptide length in P^{scFv}LHFc changed biological activity

Shortening the stalk region showed that rigidity and orientation of the system play an important role, to further investigate the influence of this the flexibility of the linker connecting the scFv and Fc regions of the ligand was reduced. P^{scFv}LH0Fc was derived by deleting the 23 amino acid linker. Afterward a 4 and 8 EAAAK repeat between the scFv and Fc regions of P^{scFv}LH0Fc was inserted, resulting in P^{scFv}LH4Fc and P^{scFv}LH8Fc, respectively. These repeats form alpha-helical coils which lead to more rigid linkers of different lengths (Figure 33). The sequences of these proteins can be found in the supplemental information section. Yields of P^{scFv}0Fc were very high and 30 ml of supernatant was sufficient for purification, while P^{scFv}4Fc and P^{scFv}8Fc had to be isolated from 120 ml of supernatant

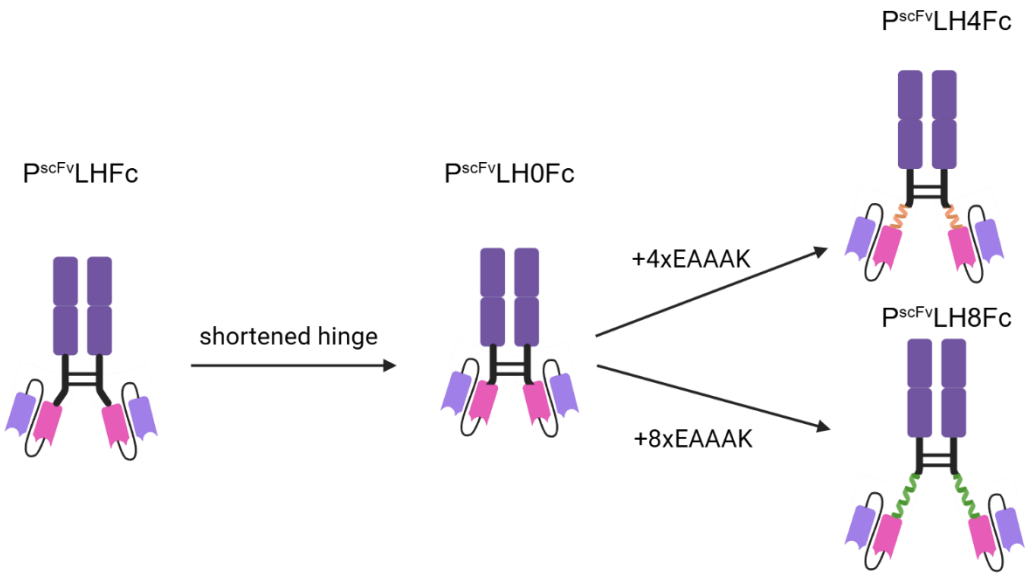

Figure 33:Schematic depiction of the different P^{scFv}Fc variants.
The hinge region of P^{scFv}LHFc was deleted resulting in the short version P^{scFv}LH0Fc. The hinge region of this protein was then elongated using either 4 EAAAK or 8 EAAAK tandem repeats that form α-helices increasing the size of the ligands.

The engineered proteins were expressed in Expi293F cells and purified as dimers (Figure 34). Surface plasmon resonance was then used to determine the affinities of these proteins for the nanobody AIP2^{VHH}. The P^{scFv}LH0Fc (Figure 35 A), P^{scFv}LH4Fc (Figure 35 B), and P^{scFv}LH8Fc (Figure 35 C) fusion proteins displayed similar affinities for AIP2^{VHH}, with dissociation constants (KD) of 20 nM, 14 nM, and 12 nM, respectively similar to that of Palivizumab (IgG1) to AIP2^{VHH}.

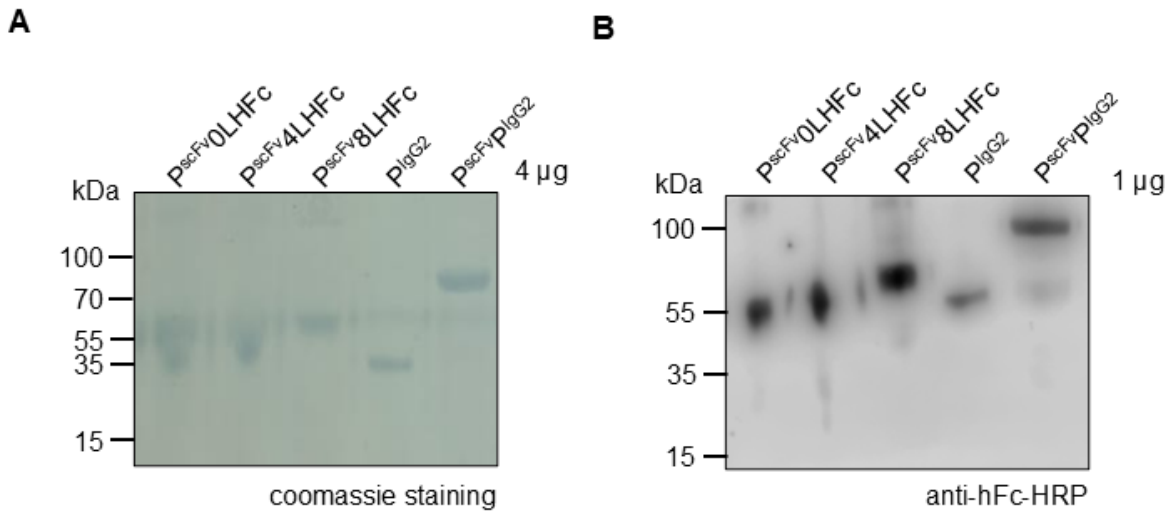

Figure 34: Analysis of purified PscFvLHFc, PscFv0LHFc, PscFv4LHFc, PscFv8LHFc, PIgG2 and PscFvPIgG2.
(A) Coomassie brilliant blue-stained gel of 4 µg purified protein P^{scFv}LHFc, P^{scFv}0LHFc, P^{scFv}4LHFc, P^{scFv}8LHFc, P^{IgG2}, and $P^{scFv}P^{IgG2}$, left and right respectively, **(B)** Western blotting of the same protins using 1 µg with anti-human Fc-HRP antibody of 1 µg purified protein as indicated.

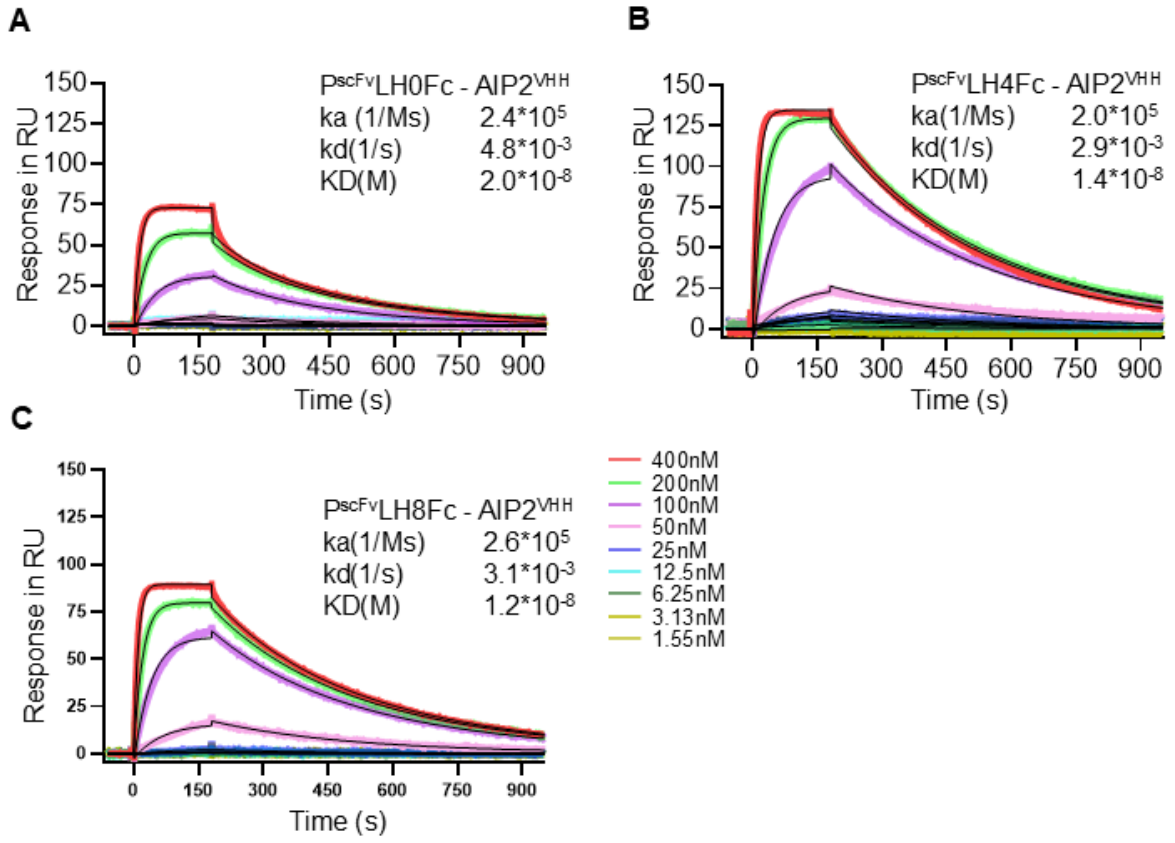

Figure 35: Binding curve of Surface plasmon resonance (BIAcore) analysis of:
(A) P^{scFv}0LHFc, (B) P^{scFv}4LHFc, and (C) P^{scFv}8LHFc captured on a Protein A chip with soluble $AIP2^{VHH}$ as analyte (concentration range: 1.55-400 nM).

4.20 Activation of AIP^{VHH}gp130 Receptors and the stalk deletion variants by P^{scFv}Fc variants with different linker lenghts

Biological activity of P^{scFv}LH0Fc, P^{scFv}LH4Fc, and P^{scFv}LH8Fc proteins to induce cellular proliferation and STAT3 phosphorylation in Ba/F3 cells expressing various AIP^{VHH}gp130 receptor variants was tested.

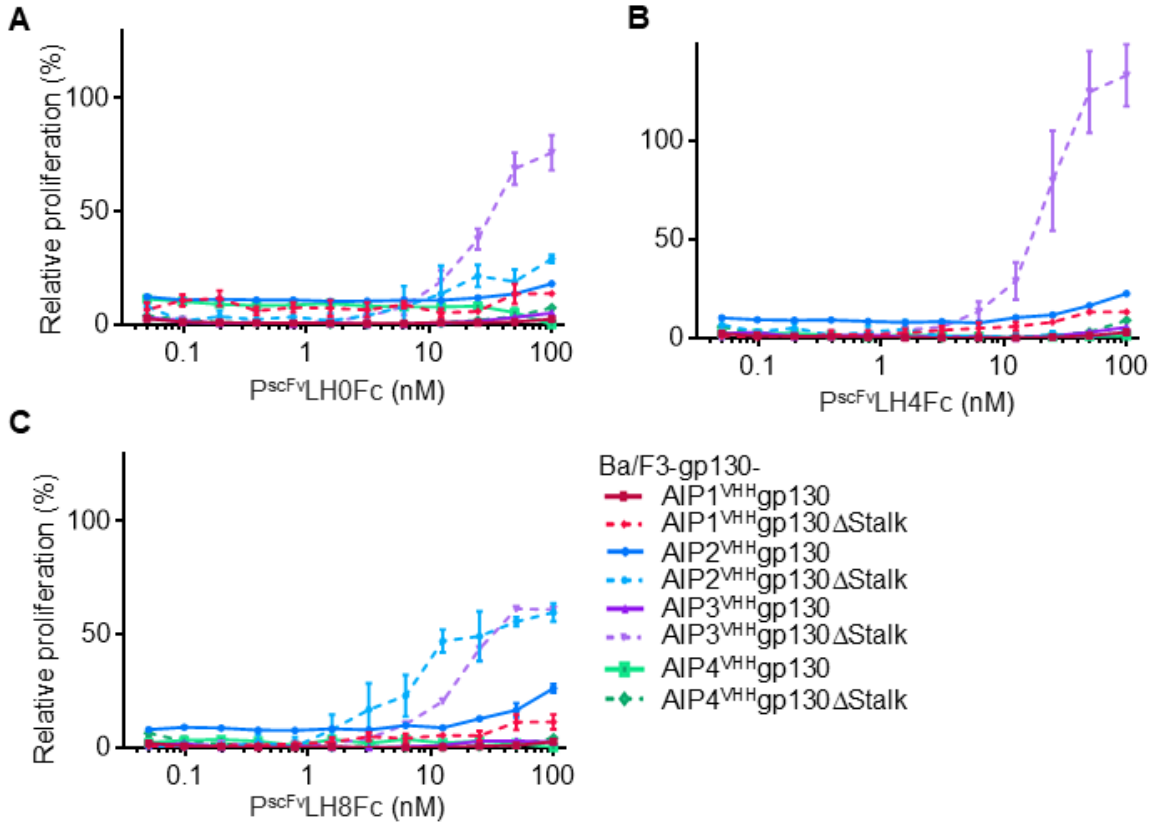

Figure 36: P^{scFv}LHFc of varying size differentially activate AIP^{VHH}gp130 variants.
(A) Dose-dependent proliferation of Ba/F3-gp130 cells expressing AIP1-4VHHgp130 and AIP1-4VHHgp130Δstalk in response to (B) P^{scFv}LH0Fc,(C) P^{scFv}LH4Fc, and (D) P^{scFv}LH8Fc (0.05-300 nM). Proliferation was normalized to HIL-6 (10 ng/ml) induced proliferation for each cell line. Data represent mean ± S.D. of three biological replicates from one representative experiment out of three.

Noticably, none of the synthetic ligands were able to stimulate proliferation or sustained STAT3 phosphorylation in cells expressing the full-length AIP^{VHH}gp130 receptors (Figure 36 A-C, Figure 37). P^{scFv}LH0Fc, P^{scFv}LH4Fc, and P^{scFv}LH8Fc were all able to induce proliferation in cells expressing the AIP3^{VHH}gp130Δstalk variant, with EC50 values ranging from 17.63 nM to 26.31 nM (Figure 36 A-C). Additionally, P^{scFv}LH8Fc could also activate the AIP2^{VHH}gp130Δstalk variant, with an EC50 of 6.954 nM (Figure 37 C).

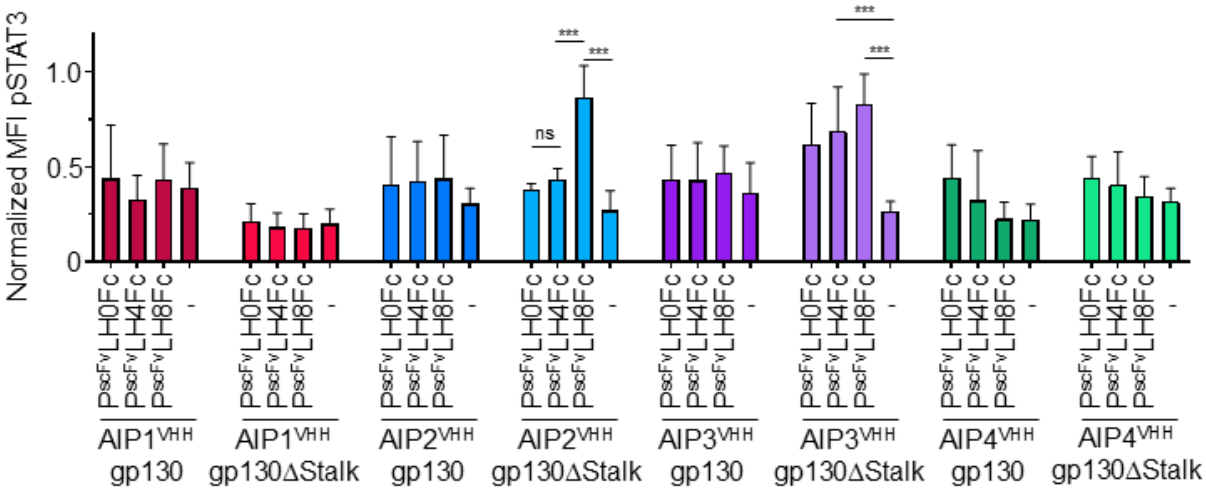

Figure 37: P^{scFv}LHFc of varying size differentially activate AIP^{VHH}gp130 variants.
Normalized Mean Fluorescence Intensity of STAT3 phosphorylation in response to P^{scFv}LH0Fc, P^{scFv}LH4Fc, and P^{scFv}LH8Fc (300 nM) for all AIP^{VHH}gp130 and AIP^{VHH}gp130Δstalk variants. Data represent mean ± S.D. of three biological replicates (n=3).

The different synthetic ligands induce varying levels of STAT3 phosphorylation in the cells expressing the AIP^{VHH}gp130Δstalk variants. Specifically, P^{scFv}LH4Fc stimulation increased STAT3 phosphorylation in AIP3^{VHH}gp130Δstalk-expressing cells, while P^{scFv}LH8Fc activated both the AIP2^{VHH}gp130Δstalk and AIP3^{VHH}gp130Δstalk variants.

These results demonstrate that the length and flexibility of the linker region between the scFv and Fc domains can significantly impact the activation capacity of the synthetic ligands. The original P^{scFv}LHFc ligand with the 23-amino acid linker appeared to have the broadest activation spectrum, suggesting that this linker length may by chance be optimal for achieving the desired receptor activation. Our experimental data did not reveal a systematic activation pattern, and current computational approaches - including AI-driven protein structure prediction - face significant limitations when modeling complex membrane receptor systems(*142*). While these computational tools provide valuable insights for initial design strategies, the development of functional receptor-ligand pairs ultimately requires empirical optimization through systematic experimental testing.

4.21 An engineered IgG2 variant of Palivizumab has similar affinity towards AIP^{VHH}s as IgG1 Palivizumab

Palivizumab-induced signaling via AIP^{VHH}gp130 was found to be almost undetectable without secondary cross-linking (Figure 15). Since antibody-induced cross-linking for synthetic receptor activation would not be feasible in vivo, an alternative Ig-backbone was investigated for synthetic receptor activation. An IgG2 variant of Palivizumab, termed P^{IgG2}, was generated (Figure 38). This approach was based on previous findings demonstrating that the presence of a unique disulfide crossover in human IgG2 variants corresponds with increased agonistic activity on natural receptors such as CD40 (*69*).

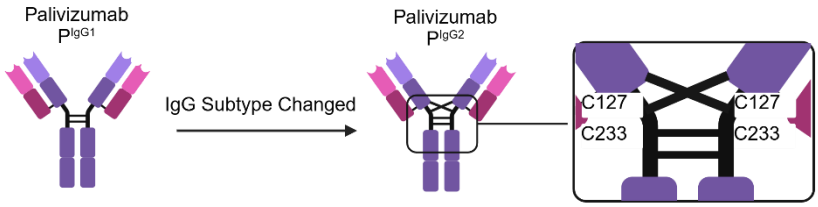

Figure 38: Schematic depiction of transformation of P^{IgG1} to P^{IgG2}.
The fab fragment of Palivizumab was transferred to the very rigid IgG2 backbone. The IgG2 variant comprises 4 disulfite bridges, mutation of S127C and S233C improves rigidity and agonistic character of the antibody.

The variable region of Palivizumab's light and heavy chains (P^{IgG1}) was genetically fused to the IgG2 backbone (Figure 38). P^{IgG2} was expressed in Expi293F™ cells and purified from the cell supernatants via Protein A affinity chromatography (Figure 34). The sequence of heavy and light chain is attached in the supplemental information section. Yields of these proteins were good and 90 ml of ExpiCHO supernatant was harvested. The interaction affinities of captured P^{IgG2} to soluble AIP1-4VHH were determined by surface plasmon resonance. AIP1-4VHH was found to bind P^{IgG2} with affinities of 0.25 nM, 14 nM, 20 nM, and 11 nM, respectively, corresponds to those determined for P^{IgG1} (Figure 39). These findings demonstrated that changing the backbone did not interfere with binding of Palivizumab to the anti-idiotypic nanobodies.

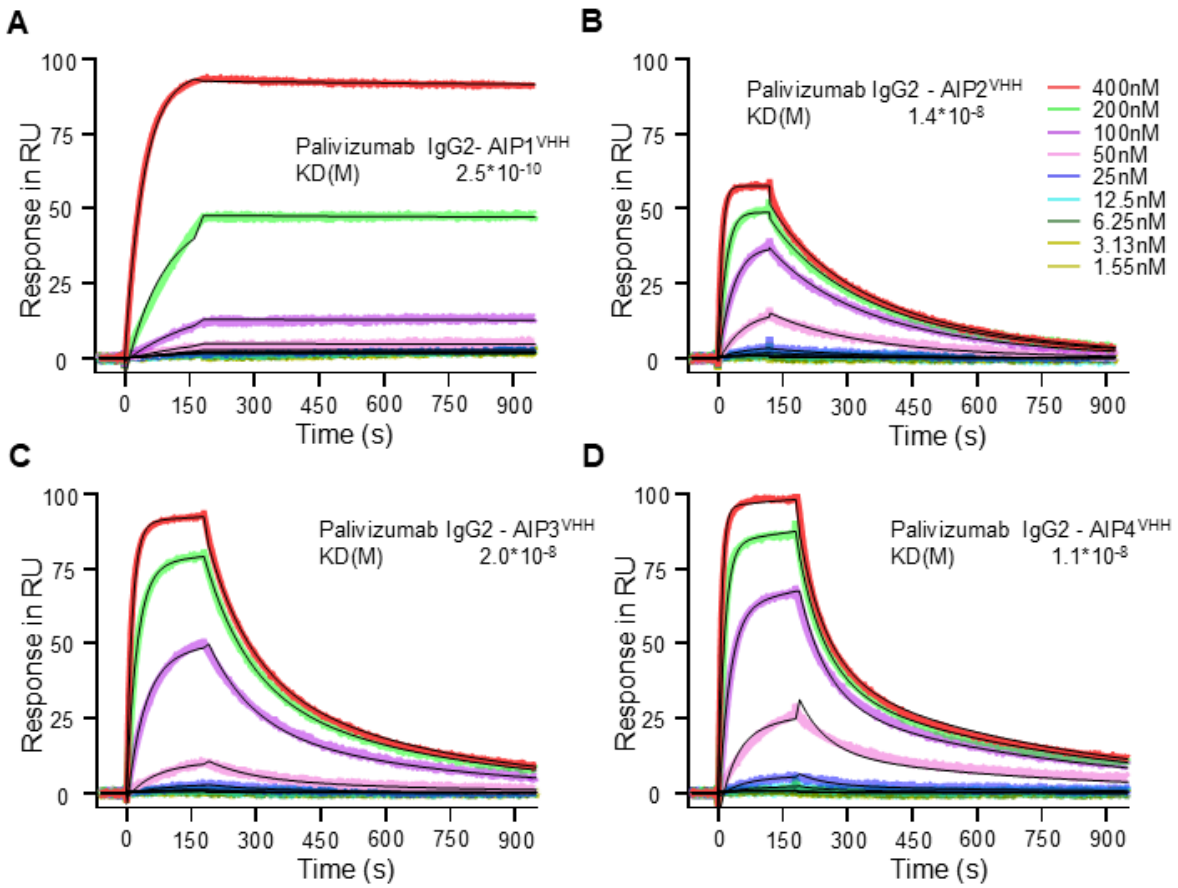

Figure 39: Reformatting of Palivizumab (P^{IgG1}) into P^{IgG2} maintained binding to $AIP1^{VHH}$ - $AIP4^{VHH}$.
(A) Surface plasmon resonance (BIAcore) analysis of P^{IgG2} captured on a Protein A chip with soluble (B) $AIP1^{VHH}$, (C) $AIP2^{VHH}$, (D) $AIP3^{VHH}$, and (E) $AIP4^{VHH}$ as analytes (concentration range: 1.55-400 nM). Sensorgrams show response units (RU) over time (colored lines) with global fit (black lines). Analytes were injected for 120 sec with 900 sec dissociation time.

4.22 Palivizumab confers biological activity via AIP2^{VHH}gp130Δstalk and AIP3^{VHH}gp130Δstalk

The biological activity of P^{IgG1} and P^{IgG2} was compared on Ba/F3-gp130 cells expressing any of the AIP1-4VHHgp130 or AIP1-4VHHgp130Δstalk variants for their ability to induce cellular proliferation and STAT3 phosphorylation. Consistent with previous results in this study, P^{IgG1} induced a very weak proliferation of Ba/F3-gp130 cells expressing AIP3^{VHH}gp130 but not via the AIP1,2,4VHHgp130 variants (Figure 40 A). Interestingly, stimulation with the Palivizumab IgG2 subclass P^{IgG2} not only induced proliferation of Ba/F3-gp130 cells expressing AIP3^{VHH}gp130 in a comparable manner as P^{IgG1}, but deletion of the stalk region in AIP3^{VHH}gp130Δstalk resulted in much stronger proliferation of respective Ba/F3-gp130 cells (EC_{50}: 24.35 nM). More importantly the deletion of the stalk region in AIP2^{VHH}gp130Δstalk led to a very strong proliferative response in respective Ba/F3-gp130 cells (EC50: 11.25 nM) (Figure 40 B).

This observation was mirrored by determination of dose-dependent ligand-induced STAT3 phosphorylation in all Ba/F3-gp130 cells expressing the AIP1-3VHHgp130 or AIP2-3VHHgp130Δstalk variants. No STAT3 phosphorylation was observed in Ba/F3-gp130 cells expressing AIP1-3VHHgp130 when stimulated with P^{IgG2} (Figure 41 A-C).Significant STAT3 phosphorylation was only achieved by stimulation of Ba/F3-gp130 cells expressing AIP2^{VHH}gp130Δstalk (Figure 41 B) or AIP3^{VHH}gp130Δstalk (Figure 41 C) with P^{IgG2} for 45 min at concentrations between 150-300 nM and 75-300 nM, respectively. In conclusion, it was demonstrated that the engineered P^{IgG2} conferred biological activity specifically of AIP2^{VHH}gp130Δstalk and AIP3^{VHH}gp130Δstalk again demonstrating the importance of rigidity and orientation of the binding regions.

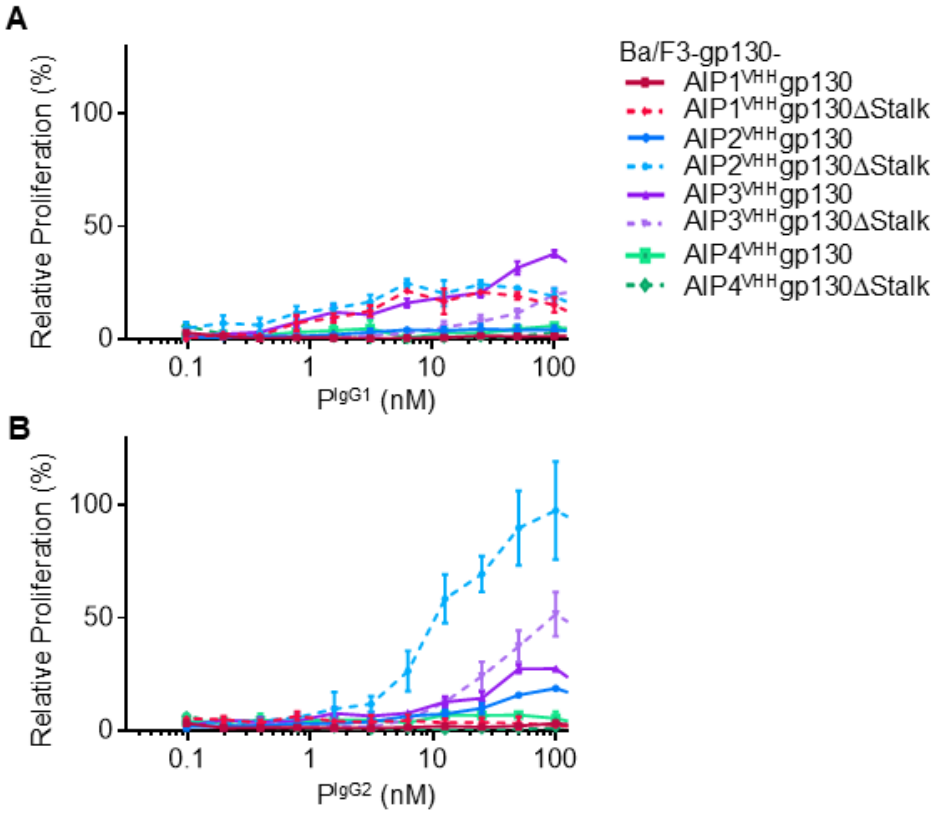

Figure 40: P^{IgG2} is an effective activator of synthetic AIP^{VHH}gp130 receptors, while (P^{IgG1}) is not.
(A) Dose-dependent proliferation of Ba/F3-gp130 cells expressing AIP1-4VHHgp130 and AIP1-4VHHgp130Δstalk in response to (B) P^{IgG1} and (C) P^{IgG2} (0.05-300 nM). Proliferation was normalized to HIL-6 (10 ng/ml) induced proliferation for each cell line. Data represent mean ± S.D. of three biological replicates from one representative experiment out of three.

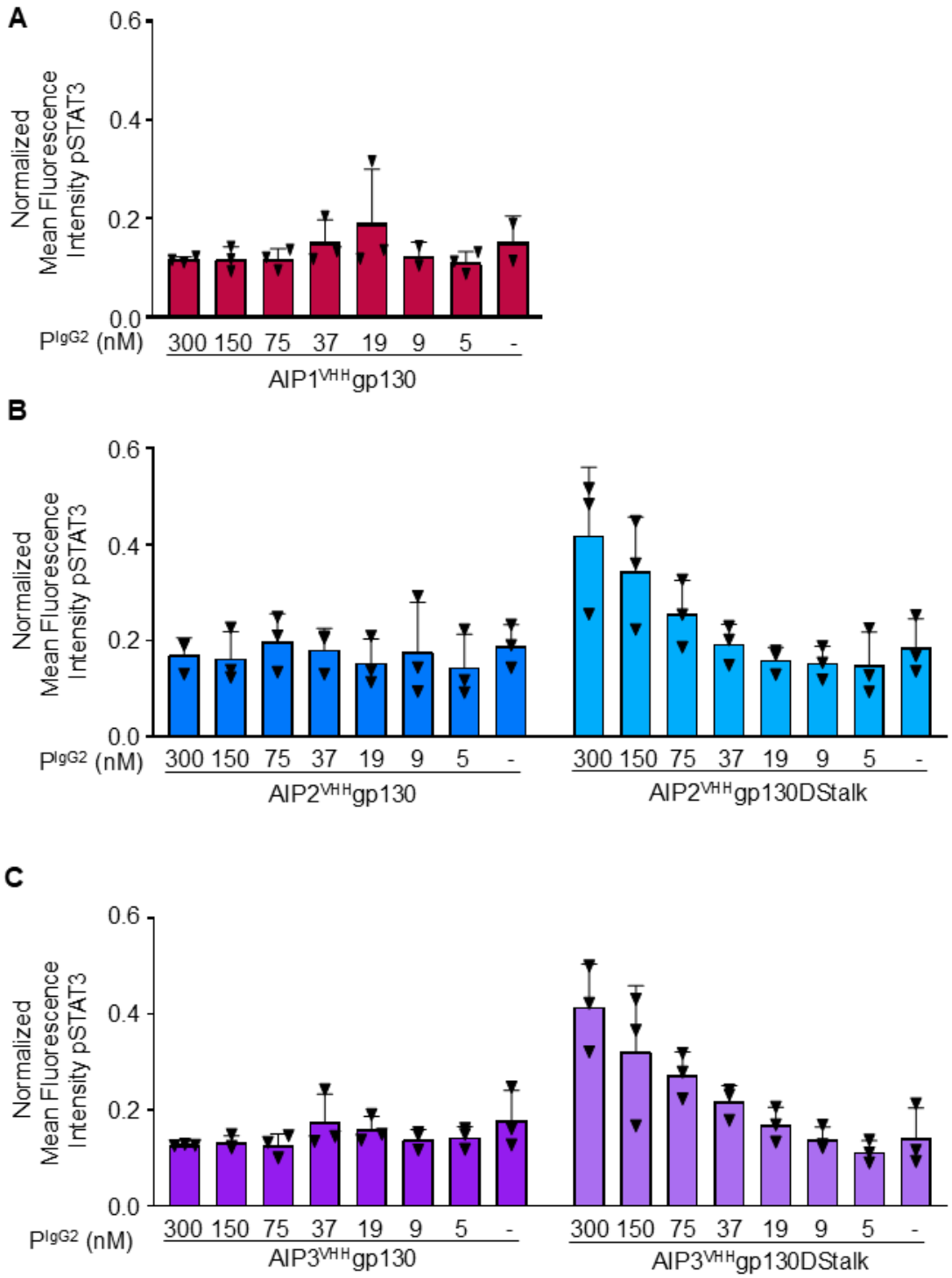

Figure 41: P^{IgG2} is an effective activator of synthetic $AIP^{VHH}gp130$ receptors, while (P^{IgG1}) is not.
(A) Normalized Mean Fluorescence Intensity of STAT3 phosphorylation in response to P^{IgG2} (5-300 nM) for (B) $AIP1^{VHH}gp130$, (C) $AIP2^{VHH}gp130$, (D) $AIP2^{VHH}gp130\Delta stalk$, (E) $AIP3^{VHH}gp130$, and (F) $AIP3^{VHH}gp130\Delta stalk$. Data represent mean ± S.D. of three biological replicates (n=3).

4.23 AIP-SyCyRs function in murine T Cells after stimulation with P^{IgG2}

To demonstrate the broader applicability of our system, primary mouse T cells were retrovirally transduced to express either AIP2gp130Δstalk or AIP3gp130Δstalk SyCyRs. Flow cytometric analysis confirmed successful surface expression of both receptor variants, with comparable expression levels (Figure 42).

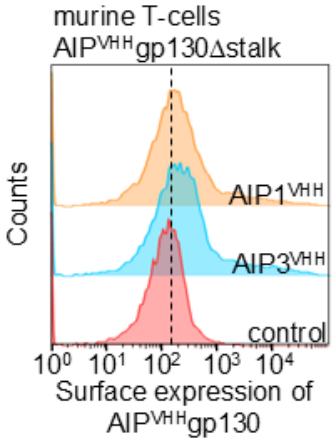

Figure 42: Expression levels of AIP^{VHH}gp130Δstalk receptors on primary murine T cells.
Flow cytometric analysis of myc-tagged synthetic receptors on transduced T cells expressing AIP2^{VHH}gp130Δstalk and AIP3^{VHH}gp130Δstalk.

STAT3 activation was examined in CD4 positive and CD8 positive T cell populations following 45 min stimulation with 300 nM of P^{scFv}LHFc, P^{IgG1}, or P^{IgG2}. Flow cytometric analysis revealed significant enhancement of STAT3 phosphorylation specifically in cells expressing AIP2gp130Δstalk and AIP3gp130Δstalk when treated with P^{IgG2}, while P^{IgG1} and P^{scFv}LHFc failed to induce comparable signaling responses in CD4 positive T cells (Figure 43 A) as well as CD8 positive T cells (Figure 43 B).

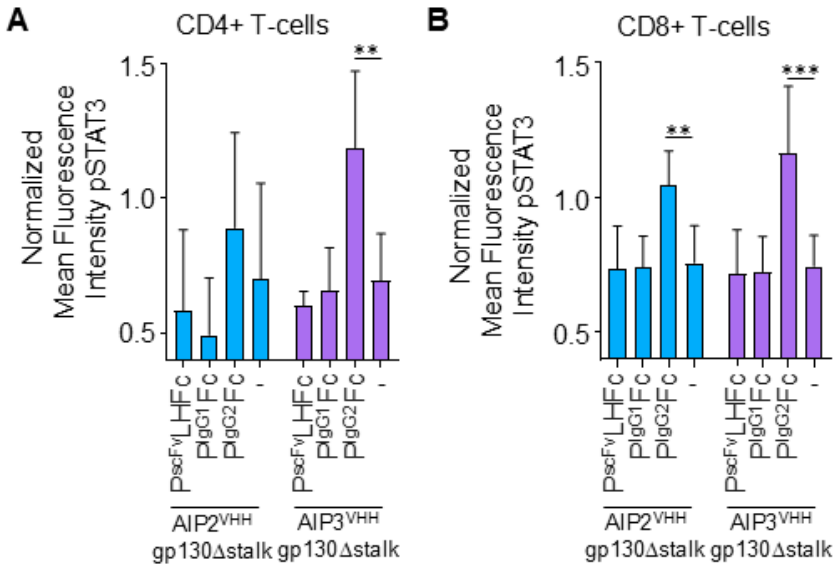

Figure 43: P^{IgG2} is an effective activator of synthetic AIP^{VHH}gp130Δstalk receptors on primary murine T cells while (P^{IgG1}) is not.
Normalized Mean Fluorescence Intensity of STAT3 phosphorylation in response to P^{scFv}LH23Fc, P^{IgG1} and P^{IgG2} (300 nM) for $AIP2^{VHH}$gp130Δstalk and $AIP3^{VHH}$gp130Δstalk in (A) CD4+ cells and (B) CD8+ cells. Data represent mean ± S.D. of three biological replicates (n=3).

4.24 Design of synthetic AIP^{VHH}Fas receptors

The death receptor Fas has been shown to induce apoptosis through initiator Caspase 8 and effector Caspase 3/7 via the trimeric FasL. Recent data, however, suggests that higher than trimeric receptor-oligomerization upon binding can also induce apoptosis. Previous studies with GFP/mCherry as synthetic ligands demonstrated that apoptosis by the Fas-SyCyR could be induced by dimers, although this was less efficient than the trimeric or oligomeric Fas-SyCyR complexes (*111*).

Building on this foundation, the anti-idiotypic synthetic cytokine system was adapted to Fas-induced apoptosis. AIP1-3VHH were genetically fused to the transmembrane and intracellular domain of human Fas. Cell surface expression of synthetic AIP1,2,3VHHFas receptors on Ba/F3-gp130 cells was confirmed by flow cytometry against the N-terminal myc-tag.

This analysis confirmed the cell surface expression of these synthetic AIP1-3VHHFas receptors on Ba/F3-gp130 cells (Figure 44). An example sequence can be found in the supplemental information section.

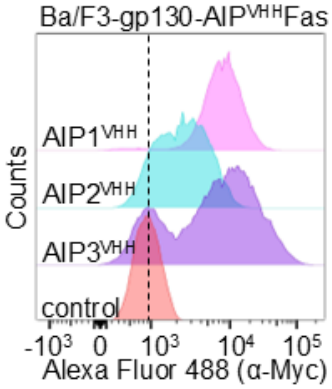

Figure 44: AIP^{VHH} fusion to Fas efficiently induce cellular apoptosis.
(A) Flow cytometry analysis of myc-tagged synthetic receptors on the surface of Ba/F3-gp130 cells expressing AIP1-3VHHFas.

Since Fas needs trimerization a ligand was designed that could potentially tetramerize receptors. Construction of 2xP^{scFv}LHFc was achieved through a linker peptide connected tandem arrangement of two P^{scFv} fused to the IgG1-Fc fragment (Figure 45). The protein was expressed in HEK293T cells and purified using Protein A beads (Figure 34 on page 80). The yield of these tetrameric ligands was quite low and 150 ml of ExpiCHO supernatant yielded enough to carry out the experiments.

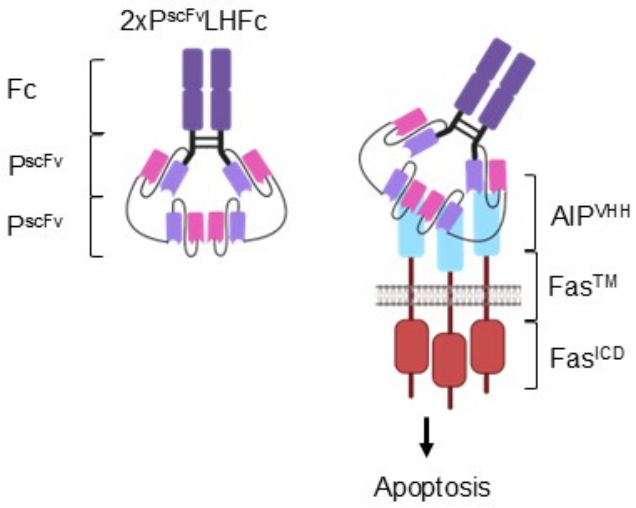

Figure 45: Schematic depiction of AIP^{VHH}Fas by tetrameric 2xP^{scFv}Fc.
The tetrameric ligand 2xP^{scFv}Fc, which has a second scFv fused to the first scFv separated by a short GS linker can bind and trimerize AIP^{VHH}Fas activating apoptosis.

4.25 AIP^{VHH}Fas receptors efficiently induce cellular apoptosis using tetravalent ligands

Ba/F3-gp130-AIP1-3VHHFas cells were subjected to analysis for activation of caspase 3/7 and induction of apoptosis after AIP^{VHH}Fas stimulation, which was compared to HIL6-induced gp130 activation.

First activation of caspase 3/7 after 6 h was evaluated, a key step in the apoptotic pathway. 2xP^{scFv}Fc was used as a tetrameric ligand while higher-ordered Fas oligomerization was induced by cross-linking of 2xP^{scFv}LHFc with hFc-mAb (1:6 molar ratio) as a control P^{scFv}Fc was used to dimerize receptors. Tetramerization and oligomerization were found to induce caspase 3/7 activation after 4 h in Ba/F3-gp130-AIP1^{VHH}Fas and Ba/F3-gp130-AIP3^{VHH}Fas cells. Oligomerization of AIP1^{VHH}Fas was approximately 2.5 to 5-fold more effective in inducing caspase 3/7 compared to tetramerization. When oligomerization clustered AIP1^{VHH}Fas, the amount of activated caspase 3/7 was always maximal, independent of the applied ligand concentration (Figure 46 A). No caspase activation was induced via AIP2^{VHH}Fas when incubated with any of the synthetic ligands (Figure 46 B). For AIP3^{VHH}Fas, tetramerization-induced caspase 3/7 activation and was as effective as oligomerization at least for 1, 10 and 100 nM. At very low concentrations of 0.1 nM only oligomerization was able to induce caspase 3/7 activation. Furthermore, dimeric P^{scFv}LHFc was found to activate AIP3^{VHH}Fas up to 50% compared to oligomerization at high concentrations of 100 nM (Figure 46 C).

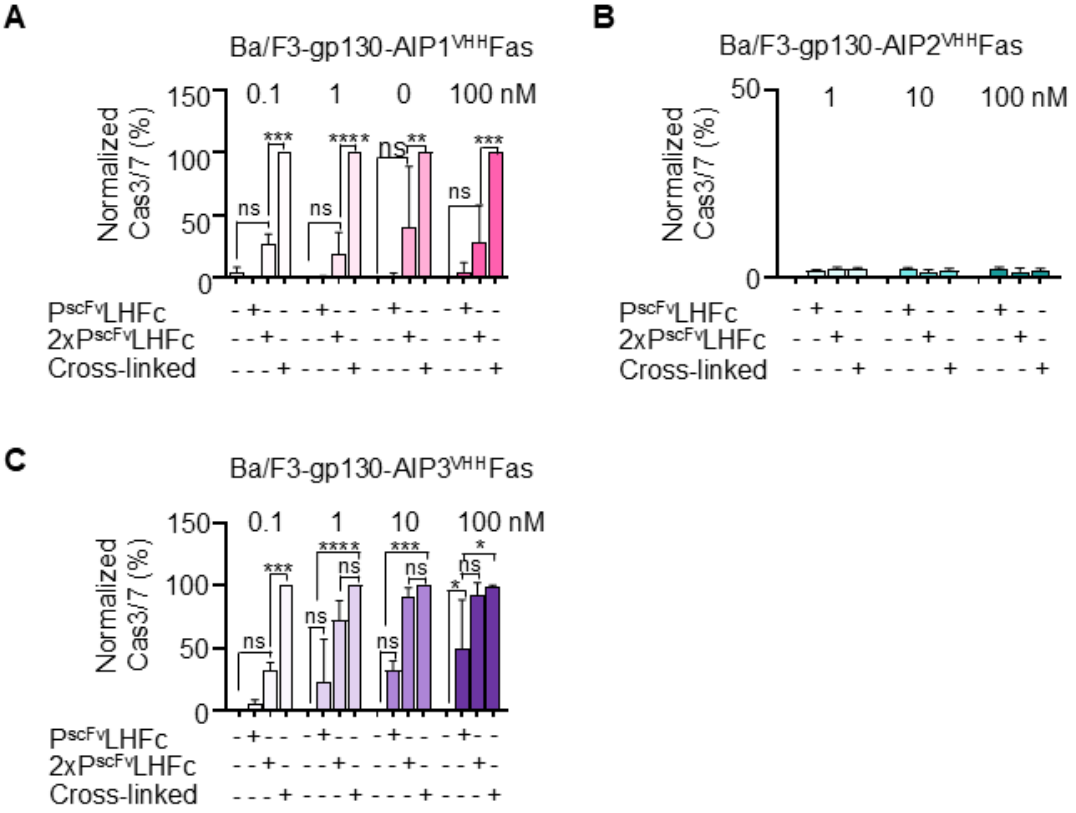

Figure 46: AIP^{VHH} fusion to Fas efficiently induce caspase activity.
(A) Relative caspase-3/7 activity after incubation of Ba/F3-gp130 cells expressing AIP1-3VHHFas with increasing concentrations (0.1, 1, 10, 100 nM) of dimeric P^{scFv}LHFc, tetrameric 2xP^{scFv}LHFc or cross-linked 2xP^{scFv}LHFc for 4 h, control cells were left untreated.

Apoptosis of Ba/F3-gp130-AIP^{VHH}Fas cells was quantified using flow cytometry after 24 and 48 h of stimulation with synthetic cytokine ligands. Cells were simultaneously stained for 7AAD and Annexin V to determine cell death. Ethanol treatment and HIL-6 stimulation were used as positive and proliferation controls, respectively. Whereas apoptotic responses were observed in Ba/F3-gp130 cells expressing AIP1^{VHH}Fas and AIP3^{VHH}Fas following ligand stimulation. In cells expressing AIP1^{VHH}Fas, tetrameric and oligomeric receptor activation efficiently induced apoptosis within 24 h and was still detectable after 48 h. Interestingly, apoptotic cells were detected after dimeric receptor activation with P^{scFv}LHFc, after 48 h, but not after 24 h (Figure 47 A). Matching the results from the caspase assay no apoptosis was induced when AIP2^{VHH}Fas was stimulated in Ba/F3-gp130 cells, with any of the ligands (Figure 47 B). Ba/F3-gp130 cells expressing AIP3^{VHH}Fas showed apoptosis after 24 h or 48 h stimulation with dimeric, tetrameric, and oligomeric P^{scFv}LHFc (Figure 47 C).

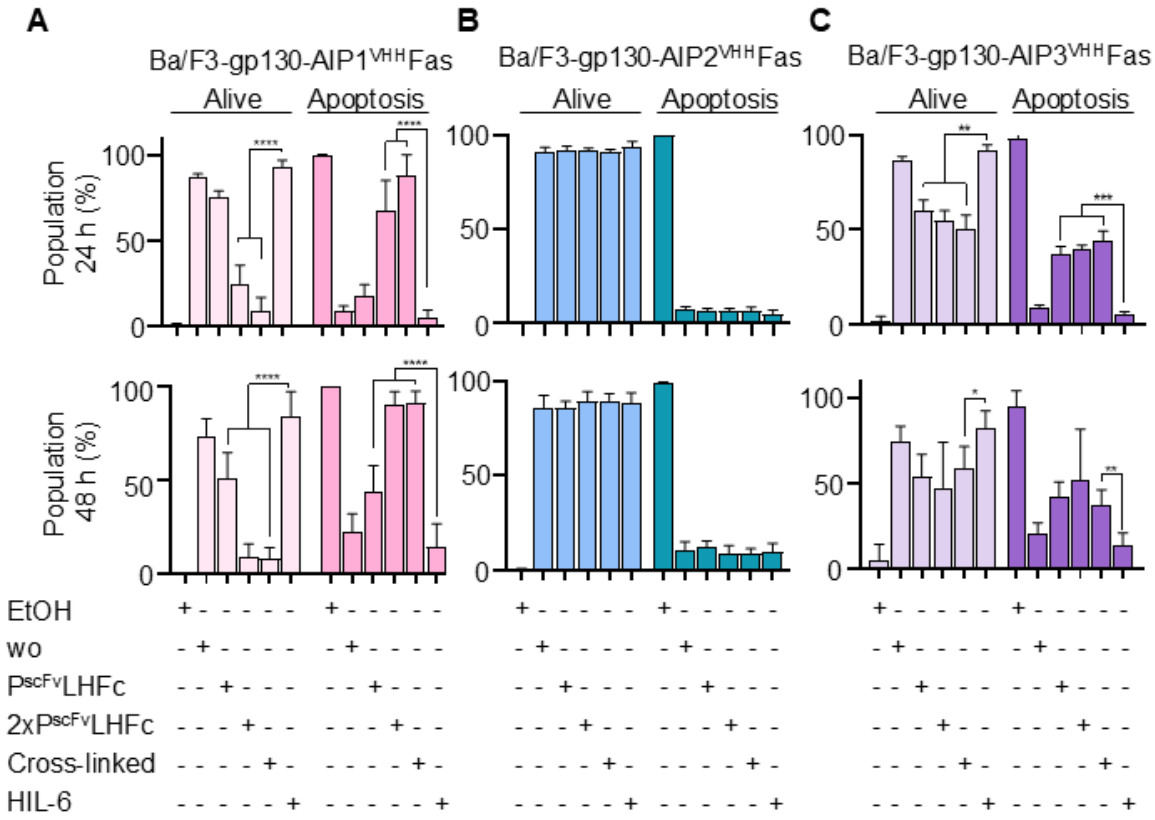

Figure 47: AIP^{VHH} fusion to Fas efficiently induce cellular apoptosis.
(A) Ba/F3-gp130 cells expressing AIP1^{VHH}Fas (B) AIP2^{VHH}Fas (C) AIP3^{VHH}Fas were incubated for 24 h or 48 h with 100 nM dimeric P^{scFv}LHFc, tetrameric 2xP^{scFv}LHFc or cross-linked 2xP^{scFv}LHFc (1:6). Controls cells were either untreated or grown with HIL-6 (10 ng/ml). Cells were incubated with HIL-6 (10 ng/ml) and washed with 70% EtOH before the measurement for the EtOH condition. Cells were stained with AnnexinV and 7-AAD and analysis was carried out using flow cytometry.

4.26 A tetravalent IgG2 Palivizumab variant mediates cellular apoptosis via AIP1 VHH hFas

A tetravalent synthetic ligand, termed P^{scFv}P^{IgG2}, was engineered by incorporating a second P^{scFv} fragment into the P^{IgG2} heavy chain backbone. This modification generated a fusion protein with four AIP binding sites, designed to facilitate receptor tetramerization (Figure 48). The sequence can be found in the supplemental information section. P^{scFv}P^{IgG2} was expressed in transiently transfected ExpiCho™ cells and purified from the cell supernatant via Protein A affinity chromatography (Figure 34 on page 80). The yield of the tetrameric ligand with an IgG2 backbone was poor and 250 ml of ExpiCHO supernatant barely yielded enough to carry out the experiments, this might be a constraint for clinical use of this ligand. However, optimization of expression and purification can overcome this drawback.

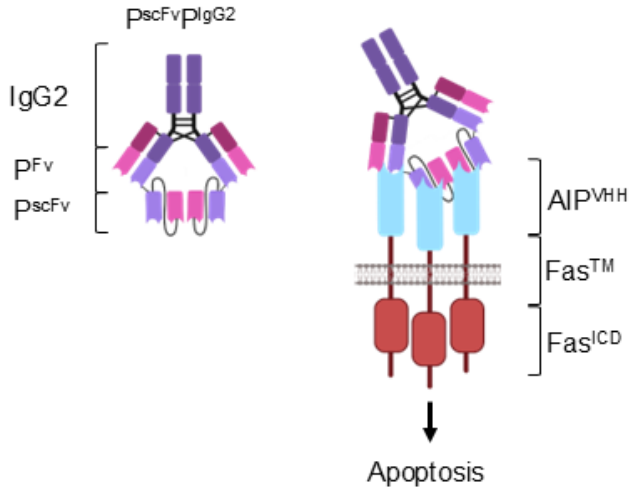

Figure 48: Schematic depiction of $P^{scFv}P^{IgG2}$ binding AIP^{VHH}Fas.
A P^{scFv} fragment was added to the heavy chain of P^{IgG2} with a short GS linker. The resulting tetravalent antibody was used to trimerize AIP^{VHH}Fas resulting in apoptosis.

The expression of the $AIP1^{VHH}$Fas and $AIP3^{VHH}$Fas receptors on the Ba/F3-gp130 cells was confirmed by flow cytometry. Both cell lines showed high expression levels, noticeable is however that there is a second population in $AIP3^{VHH}$gp130 that does not show high expression of the receptor, which can also be observed in the first transduction (Figure 49).

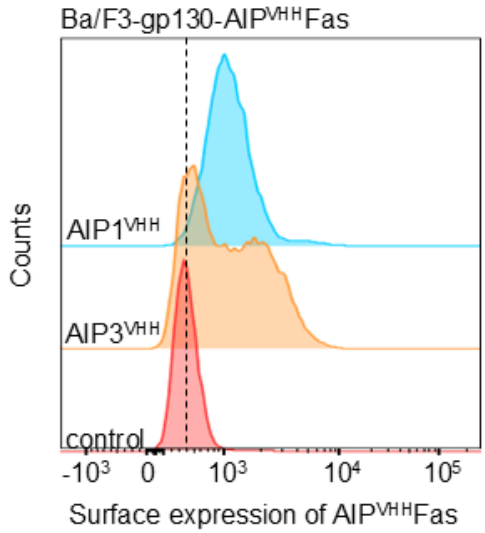

Figure 49: AIP^{VHH} fusion to hFas efficiently induce cellular apoptosis.
Flow cytometric analysis of myc-tagged synthetic receptors on Ba/F3-gp130 cells expressing $AIP1^{VHH}$Fas and $AIP3^{VHH}$Fas.

The tetravalent Palivizumab variant was functionally evaluated using the synthetic Fas receptor system. After 6 h of $P^{scFv}P^{IgG2}$ stimulation, caspase 3/7 activity was detected in Ba/F3-gp130-AIP1^{VHH}Fas cells (Figure 50 A), while no activity was observed in Ba/F3-gp130-AIP3^{VHH}Fas cells (Figure 50 B). As expected, receptor dimerization by P^{IgG2} failed to induce caspase 3/7 activity in either AIP1^{VHH}Fas or AIP3^{VHH}Fas expressing cells during the same time period.

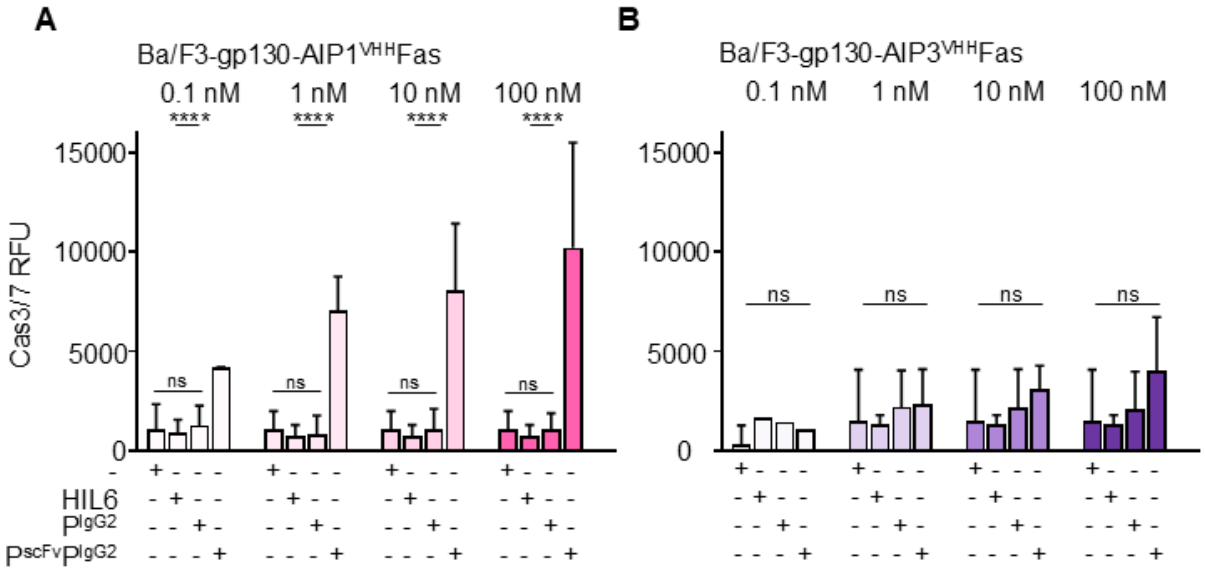

Figure 50: AIP^{VHH} fusion to hFas efficiently induce caspase activation.
Flow cytometric analysis of myc-tagged synthetic receptors on Ba/F3-gp130 cells expressing AIP1^{VHH}Fas and AIP3^{VHH}Fas. Caspase-3/7 activity after 6 h incubation of Ba/F3-gp130 cells expressing (A) AIP1^{VHH}Fas or (B) AIP3^{VHH}Fas with dimeric P^{IgG2} or tetrameric $P^{scFv}P^{IgG2}$ (0.1-100 nM). Controls: untreated or HIL-6 (10 ng/ml) treated cells.

$P^{scFv}P^{IgG2}$ ligand was able to induce apoptosis in a dose-dependent manner in the Ba/F3-gp130-AIP1^{VHH}Fas cells ranging from 0.1 nM to 100 nM, while dimerization by the parental P^{IgG2} antibody did not (Figure 51 A). In contrast, the $P^{scFv}P^{IgG2}$ ligand did not trigger apoptosis in the Ba/F3-gp130-AIP3^{VHH}Fas cells (Figure 51 B).

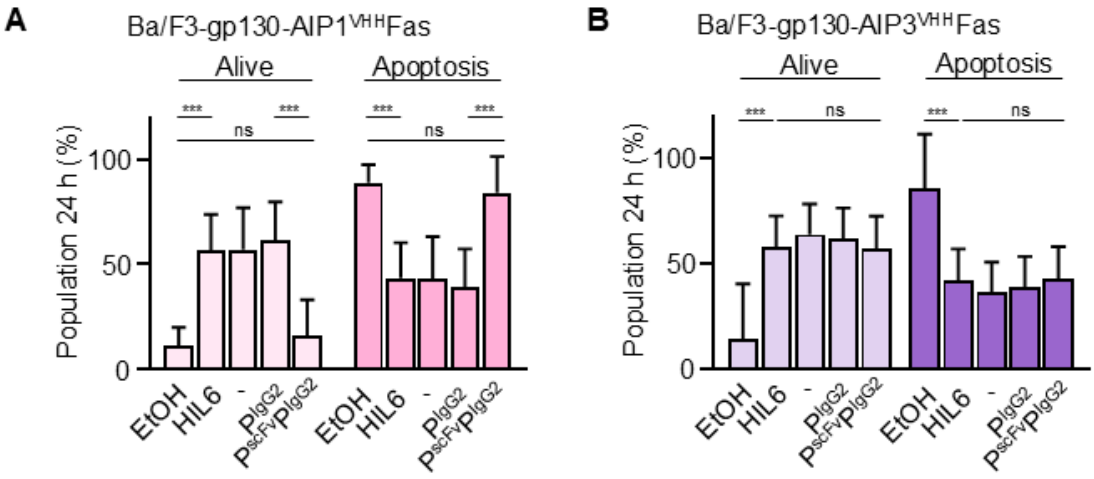

Figure 51: AIP^{VHH} fusion to hFas efficiently induce cellular apoptosis.
(A) Flow cytometric analysis of myc-tagged synthetic receptors on Ba/F3-gp130 cells expressing AIP1^{VHH}Fas and AIP3^{VHH}Fas. (B) Caspase-3/7 activity after 6 h incubation of Ba/F3-gp130 cells expressing (C) AIP1^{VHH}Fas or (D) AIP3^{VHH}Fas with dimeric P^{IgG2} or tetrameric $P^{scFv}P^{IgG2}$ (0.1-100 nM). Controls: untreated or HIL-6 (10 ng/ml) treated cells. (E) AnnexinV and 7-AAD staining of Ba/F3-gp130 cells expressing (F) AIP1^{VHH}Fas or (G) AIP3^{VHH}Fas after 24 h incubation with 100 nM P^{IgG2} or $P^{scFv}P^{IgG2}$. Controls: untreated, HIL-6 (10 ng/ml) treated, or HIL-6 treated and 70% EtOH washed cells. Analysis was performed by flow cytometry.

These findings demonstrate the potential of the engineered tetravalent ligands based on Palivizumab for use on receptors comprising AIPs. Especially interesting is that $P^{scFv}P^{IgG2}$ ligand very closely resembles the FDA approved antibody Palivizumab and is able to induce higher-order receptor clustering and effectively activate pathways that require receptor trimerization or tetramerization, such as Fas-mediated apoptosis.

5 Discussion

In this study, we present the systematic development of a novel synthetic cytokine receptor (SyCyR) system, which demonstrates significant advancements in specificity, control mechanisms and, with particular emphasis on potential clinical applicability in the next generation of cell gene therapy. Through methodical progression from SyCyR^{1st} to SyCyR^{3rd}, fundamental limitations were addressed and the system's functionality systematically optimized. The fundamental importance of cytokine signaling pathways in biological processes and their therapeutic potential in cell gene therapy, when precisely regulated is at the center of the study. While existing approaches such as cytokimeras, cytokine mimetics, synthekines, and fusokines represent innovative developments in cytokine engineering, they exhibit inherent limitations regarding cellular specificity, potentially resulting in undesired activation of non-target cells. The established success of CAR-T cell therapy, which employs synthetic receptors for tumor antigen recognition, provides compelling evidence for the development of analogous systems with broader therapeutic applications. These observations formed the theoretical foundation for the experimental approach in this study.

5.1 Antibodies as ligands for SyCyRs

The developmental trajectory of the SyCyR system encompasses three distinct generations, each representing a significant advancement for applicability. The initial iteration, SyCyR^{1st}(*89, 112*), utilized nanobodies specific to GFP or mCherry(*143, 144*) as extracellular receptor domains, complemented by dimeric GFP/mCherry fusion proteins serving as corresponding ligands. This configuration demonstrated unprecedented background-free activation and cell-type specificity. The system exhibits remarkable molecular adaptability, as evidenced by successful incorporation of diverse intracellular signaling domains, including those derived from tumor necrosis factor (TNF) (*111*), Fas (*111*), glypkoprotein of 130 kDa (gp130) (*112*), interferon alpha receptor complex (IFNAR) (*113*), IL-12, and IL-23 receptors (*112*). This inherent modularity facilitates the construction of precise control mechanisms like survival or apoptosis, particularly advantageous for chimeric antigen receptors CAR-T cell therapeutic applications. In vivo functionality was conclusively demonstrated through expression of the first generation synthetic receptors in murine models, followed by systematic administration of dimeric fluorophores(*112*). Hence, there is also the possibility to use the system to emulate disease phenotypes in vivo by specifically growing or diminishing populations of cells expressing the receptors under control of tamoxifen in mice which transgenically contain an expression cassette. However, a significant limitation emerged: the non-human nature of

GFP/mCherry ligands would induce immunogenic responses upon repeated in vivo administration, presenting a substantial obstacle for clinical applications in cell and gene therapy, including CAR-T therapeutic approaches. Nanobodies on the other hand can be easily humanized, making them the perfect choice for use in a therapeutic setting (*145*).

To overcome the immunogenicity limitations inherent in the first SyCyR generation, we developed SyCyR^{2nd}, implementing antibody-anti-idiotypic nanobody pairs as non-immunogenic synthetic ligands (*100*). This strategic approach was chosen because approved commercial antibodies targeting non-human antigens could function as surrogate synthetic ligands for anti-idiotypic nanobody-cytokine receptors, thereby circumventing interactions with endogenous human targets while being non-immunogenic. Following this rationale, we systematically excluded food and drug administration (FDA)/ european medicines agency (EMA)-approved antibodies targeting human proteins, such as Tocilizumab (anti-IL-6R) (*84*), Infliximab (anti-TNF) (*85*), and Ipilimumab (anti-CTLA-4) (*86*), from consideration, since they would not specifically bind to engineered cells in patients and would have effects on other cells. Instead, we identified and evaluated multiple FDA/EMA-approved antibodies specifically targeting foreign viral and bacterial antigens: the anti-RSV humanized IgG1 antibodies Palivizumab (*82*) and Nirsevimab (*87*); the anti-SARS-CoV-2 human IgG1 antibodies Sotrovimab (*146*), Regdanvimab (*147*), Imdevimab, and Casirivimab (*148*); the anti-Ebola human IgG1 Ansuvimab and REGN-EB3 cocktail (atoltivimab, maftivimab, odesivimab) (*88*); and the anti-bacterial/anthrax human IgG1 Raxibacumab (*149*). Among these candidates, we selected Palivizumab as our model ligand, based on its established safety profile since its 1998 FDA approval and its well-characterized mechanism of targeting the antigenic site of the RSV fusion (F) protein (*82*).

5.2 Generation and characterization of Anti-idiotypic nanobodies against Palivizumab

Since no anti-idiotypic nanobodies against Palivizumab were available, the nanobodies were generated by llama immunization and high affinity candidates selected by yeast display technology. This approach yielded four distinct anti-idiotypic nanobody variants (AIPs 1-4), each demonstrating different binding affinities to Palivizumab as determined by Surface Plasmon Resonance (SPR) ranging from low 3.14 nM to high 25.97 pM. These AIPs were subsequently fused to the transmembrane and intracellular domain of gp130 to create synthetic cytokine receptor fusion proteins resulting in SyCyRs. However, initial attempts at receptor activation using unmodified Palivizumab IgG1 proved unsuccessful, necessitating system

optimization. While receptor activation could be achieved through Fc antibody-mediated cross-linking of Palivizumab proving that the receptors can be activated. However, since this is not possible in vivo we hypothesized that the distance between the epitopes was too long in the original antibody. We subsequently engineered dimeric and tetrameric scFv-Fc fusion proteins, which demonstrated high biological activity, leading to SyCyR^{2nd} (*138*). This success was attributed to the deletion of constant domains in the constant domain of the antibody, resulting in reduced spatial separation of variable domains and more efficient receptor clustering.

5.3 Receptor and antibody engineering of gp130 based SyCyRs and Palivizumab to improve efficacy

The development of SyCyR^{3rd} incorporated fundamental structural modifications to both receptor and ligand components, representing a significant advancement in synthetic receptor design and understanding of the interplay between receptor and ligand. A critical innovation involved the strategic truncation of the extracellular stalk region, originally derived from native gp130, which serves as the architectural bridge between transmembrane and extracellular domains. This modification was implemented to enhance interaction rigidity and optimize cytoplasmic domain rotation, thereby improving receptor signaling efficacy (*150*). This approach was theoretically supported by established knowledge of juxtamembrane region functionality in both gp130 and analogous systems such as GEMS (*102, 116*). Our investigation of the stalk region revealed its crucial regulatory role; its deletion resulted in enhanced cell surface expression and, notably, activated previously non-responsive synthetic receptor variants, suggesting significant influence on receptor conformational states and accessibility. The structural characteristics of this juxtamembrane segment, including its length, flexibility, and amino acid composition, are determinant factors in receptor oligomerization and subsequent signal transduction. The deletion of the stalk region led to dramatically altered activation pattern upon treatment with P^{scFv}Fc, rendering the previously active AIP1gp130 variant inactive and the inactive AIP2gp130 variant active, while AIP3gp130 was merely substantially more active than the non-deleted variant. It was found that this region significantly influences the signaling efficacy of SyCyRs similar to what has been described in both gp130 and GEMS. Through systematic modification of these parameters, optimization of receptor performance and signal modulation could be established. It is possible that deletion or addition of further amino acids could lead to improved efficacy of the receptors. In both GEMS and

gp130 addition of alanine residues to the intracellular juxtamembrane region led to unpredictable changes in efficacy and often no change was observed (*102, 116*).

Further structural optimization involved systematic modification of linker lengths between scFv and Fc domains to precisely control receptor spacing. Through systematic experimentation with varying linker lengths in P^{scFv}LHFc constructs, we demonstrated the critical nature of spatial constraints, establishing that precise control of inter-domain distance and flexibility between scFv and Fc regions is essential for optimal receptor function. A fundamental discovery emerged from our systematic analysis: the critical determinants of enhanced signaling are primarily structural parameters - specifically rigidity, molecular distance, and spatial orientation/rotation, rather than binding affinity alone as has been shown in CD40 activating antibodies (*69*). This principle was conclusively proven through our observation of differential signaling responses to various P^{scFv} constructs: P^{scFv}0Fc, with a deleted hinge region and P^{scFv}4Fc, with 4 rigid EAAAK repeats, exhibited signaling disruption for most receptors and were only able to activate AIP3^{VHH}gp130Δstalk, while P^{scFv}8Fc, with 8 EAAAK repeats, successfully activated AIP2^{VHH}gp130Δstalk and AIP3^{VHH}gp130Δstalk. The longest linker resulted in the highest potency of any ligand on cells expressing AIP3^{VHH}gp130Δstalk. It is worth noting, that receptor expression levels did not influence downstream signaling efficiency, presumably due to signal amplification mediated through STAT3 pathways. Interestingly the linker length of P^{scFv}LH8Fc is, based on AI generated structure predictions, similar to that of the previously deleted constant domain of IgG1 Palivizumab. This led us to hypothesize that not the length, but the rigidity is crucial for receptor activation.

The implementation of an IgG2 backbone for Palivizumab (P^{IgG2}) represented a crucial advancement in our system's development. This modification, characterized by enhanced agonistic activity due to its distinctively rigid hinge region due to distinct disulfate bridges, demonstrated remarkable improvement in receptor activation, particularly in conjunction with stalk deletion variants (Figure 52). P^{IgG2} is able to activate AIP2^{VHH}gp130Δstalk at a concentration of 300nM with an EC50 of 11.25 nM and AIP3^{VHH}gp130Δstalk at a concentration of 75nM and an EC50 of 24.35 nM. These results provide compelling evidence for the utility of antibody engineering in modulating synthetic receptor system functionality (*150*). However, the necessary concentrations for persistent activation are quite high. These main findings creating SyCyR^{3rd} are summarized in Figure 52.

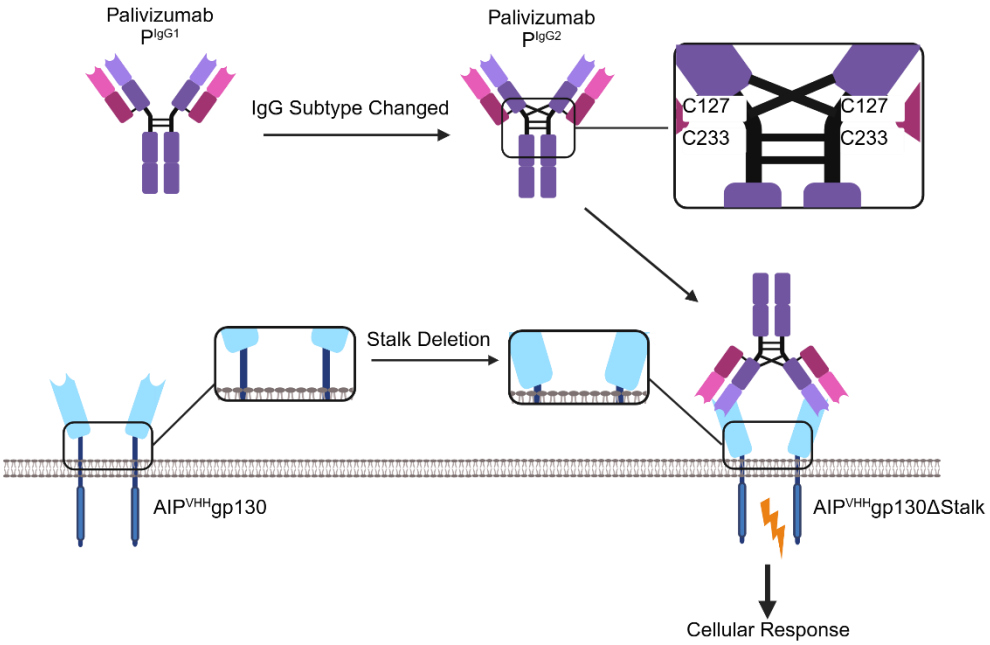

Figure 52: Schematic summary of the generation of third generation SyCyRs (SyCyR^{3rd}). Convergence of two approaches led to the development of a functioning receptor and ligand pair suitable for therapeutic use. The first step was to change the rigidity of the antibody by transforming it from a its flexible IgG1 backbone to a more rigid IgG2 backbone (top part). The second step was to truncate the flexible stalk region from the receptor resulting in a possibly more rigid receptor, possibly leading to different orientation of the intracellular part of the receptor.

5.4 Applicability to primary T cells

The system's therapeutic relevance was validated through successful demonstration of P^{IgG2}-mediated activation in primary mouse T cells, establishing functionality in clinically relevant contexts. Primary cells T cells retrovirally expressing AIP2^{VHH}gp130 or AIP3^{VHH}gp130 and presenting either CD4 or CD8 both exhibited increased significant STAT3 activation when stimulated with P^{IgG2} but not P^{IgG1} or, surprisingly P^{scFv}LHFc which was able to activate these two receptors in Ba/F3-gp130 cells.

5.5 SyCyR oligomerization using tetravalent Palivizumab variants

SyCyRs incorporating nanobodies that bind to GFP or mCherry in their extracellular domain were engineered utilizing diverse intracellular receptor components, including those from the IL-23 receptor family and, notably, members of the TNFR family such as Fas (*111*), which requires trimerization or higher-order oligomerization for signal transduction. To demonstrate that oligomerization could be achieved using AIP as an extracellular domain, we generated three novel receptors comprising AIP1-3 fused to the transmembrane and intracellular domains of Fas.

As an initial proof-of-concept for activation through oligomerization, we engineered Fc fusion proteins containing tandem-linked Palivizumab scFv fragments connected by a short glycine-serine linker, thereby creating a tetravalent ligand. Subsequently, we observed Fas-induced apoptosis after 6 h, as evidenced by caspase 3/7 activation in AIP1^{VHH}Fas and AIP3^{VHH}Fas at concentrations of 1 nM. Further crosslinking with anti-human Fc antibody resulted in activation at 0.1 nM, presumably due to enhanced clustering via oligomerization. This activation pattern remained consistent when apoptosis was measured after 24 or 48 h. Notably, AIP2^{VHH}Fas showed no activation at any concentration or time point, leading to its exclusion from subsequent experiments.

In pursuit of enhanced therapeutic applicability, we modified the system by utilizing the IgG2 backbone of Palivizumab. This modification involved incorporating a short glycine-serine linker followed by Palivizumab scFv to the heavy chain of the construct, yielding a tetravalent ligand with an IgG2 base. The resultant tetravalent P^{scFv}P^{IgG2} successfully induced caspase 3/7 activity after 6 h at concentrations as low as 0.1 nM. The subsequent apoptosis, measured after 24 h for AIP1^{VHH}Fas, clearly demonstrated our capability to precisely regulate receptor clustering and downstream signaling cascades. Interestingly P^{scFv}P^{IgG2} was unable to activate AIP3^{VHH}Fas, while dimeric P^{IgG2} showed no activity on either receptor, as is expected.

5.6 Clinical Translation and Therapeutic Applications

The engineering of customized SyCyR represents a significant advancement in CAR-T cell therapy optimization. These novel receptor systems enable precise modulation of CAR-T cell function, addressing fundamental limitations in current therapeutic approaches. It has been

shown that enhanced T cell activation through STAT3 in CD8+ T cells could substantially improve CAR-T cell efficacy against solid tumors and those expressing low antigen levels (*130*). It was shown that SyCyR^{3rd} can activate STAT3 signaling in those cells.

The system's potential for clinical translation is substantiated by several key attributes: firstly, the utilization of Palivizumab, an FDA-approved antibody with established safety profiles; secondly, the absence of off-target effects since Palivizumab targets a viral protein; and thirdly, the inherent modularity of the design, permitting integration with diverse intracellular signaling domains. This architectural flexibility renders the system adaptable across a broad spectrum of therapeutic applications, with particular relevance to CAR-T cell therapy or other cell gene therapies.

A particularly significant feature of our system is its precise controllability, manifested through an effective "On/Off" switching mechanism achieved via the administration of soluble nanobodies or Palivizumab. This capability represents a crucial safety feature for therapeutic applications. The system's design incorporates several strategic elements that enhance its clinical potential: the utilization of approved antibodies, emphasis on non-immunogenic ligand development, and systematic optimization of both receptor and ligand architectures.

5.7 Outlook

The following sections will explore in detail how this system can be applied to address T cell exhaustion, implement Fas-mediated apoptosis, and fine-tune T cell activation through the possibility of implementing sophisticated logic gates, as precise control mechanisms, representing key advances for cellular therapeutic applications.

Of particular significance is the potential to overcome T cell exhaustion, a critical barrier in maintaining durable patient responses. This is marked by decrease in STAT3 activation. One potential application of the AIP^{VHH}gp130 system could be to prevent T cell exhaustion through controlled STAT3 activation, thereby maintaining T cell functionality over extended periods. (*130*).

There are however also more severe complications of CAR-T therapy. Cytokine Release Syndrome (CRS) remains a significant challenge, manifesting through massive release of IL-6, IL-1, and TNF, with symptoms ranging from mild flu-like symptoms to severe organ failure. CRS is managed with tocilizumab, an anti-IL-6R antibody (*151, 152*). Other severe toxicities include Immune Effector Cell-Associated Neurotoxicity Syndrome (ICANS), presenting with confusion, seizures, and cerebral edema, treated with corticosteroids (*153, 154*). Safety mechanisms have been extensively developed to control CAR-T cell activity. Inducible CARs respond to small molecule activators, allowing temporal control of T cell function. Split systems separate antigen-binding and signaling domains for additional control. Suicide genes, including iCASP9 (*155*)or CD20-transduced T cells responsive to rituximab (*156*), enable rapid elimination of CAR-T cells when severe toxicities occur and are undergoing clinical trials at the moment. The development of SyCyRs offer promising avenues for enhancing the specificity, safety, and efficacy of cellular therapies. These advancements could potentially address some of the current limitations of CAR-T cell therapy. The AIP^{VHH}Fas system could be utilized to rapidly eliminate CAR-T cells upon early signs of CRS, leading to apoptosis after application of the corresponding ligand, providing a safety mechanism. Another application could be to abolish the modified cells after successful therapy, since CAR-T cells were found to persist in patients for 10 years (*157*).

To escape CAR-T cells tumors can evolve to downregulate the targeted tumor antigen (*158*). To address this antigen escape mechanism and tumor heterogeneity, CAR-T cells that can target multiple antigens simultaneously are being developed. These include tandem CARs, targeting

two antigens with a single CAR construct by linking two scFvs in the extracellular domain and dual CARs expressing two different CARs on the same cell (*159-161*).

CAR-T cells are prone to off target effects and over activation by detecting cells that are expressing the tumor antigen at a lower level than the tumor cells (*120*). Logic-gated CAR systems are being developed that require the presence of multiple antigens for activation, improving specificity and reducing off-target effects. Logic-gated CAR systems represent a sophisticated advancement in cellular immunotherapy, employing complex molecular strategies to enhance targeting specificity and safety (*162*). AND-gate CARs utilize dual antigen recognition mechanisms, requiring the presence of two distinct tumor antigens for full T cell activation. These systems are implemented through various approaches, including split CAR designs where CD3ζ and costimulatory domains are separated onto different receptors, synthetic Notch (synNotch) systems enabling sequential activation, and the computationally designed Co-LOCKR system with molecular switches (*163*). Complementing these, NOT-gate CARs incorporate inhibitory signals to prevent activation in the presence of antigens on healthy tissues, primarily through iCARs expressing both activating and inhibitory components (*120*). Recent innovations have expanded these concepts to include three-input logic gates, tunable systems with adjustable activation thresholds, and Boolean logic combinations, enabling more precise control over cellular responses *in vivo* in mice (*164*). These advanced designs are particularly relevant for addressing challenges in solid tumor treatment, where distinguishing between malignant and healthy tissues is crucial. SyCyRs could also be employed in these systems offering the ability to temporally control activation of signals specifically in CARs without off target effects by either injecting the antibodies into the tumor or targeting it using a fused fab fragment against proteins enriched on the tumor surface. For example to the antibody F8 binding to a cancer-specific fibronectin isoform, similar to the immunocytokine F8-IL2 (*165*).

The findings of this study demonstrate considerable promise, it has to be acknowledged that comprehensive in vivo studies as well as detailed pharmacokinetic/pharmacovigilance analyses are necessary. Nevertheless, this research establishes a robust foundation for the development of highly precise and controllable cell and gene therapies. The molecular principles elucidated in this study provide critical insights for future optimization and clinical implementation of synthetic receptor systems.

The therapeutic potential of this system extends significantly beyond conventional immunotherapy applications. The therapeutic application of synthetic cytokines faces several critical limitations despite its potential. Due to the pleiotropic nature of cytokines, their activity across diverse cell populations can trigger adverse effects including inflammatory responses and cytokine release syndrome. While cytokimeras, cytokine mimetics(*50, 51*), synthekines, and fusokines(*49, 166*) represent innovative cytokine engineering approaches designed to activate specific cell types based on receptor expression, they cannot exclusively target engineered cells, limiting their specificity in cellular activation. Furthermore, the immune system may recognize these engineered proteins as foreign entities, eliciting neutralizing antibodies and allergic responses. The challenge of achieving precise targeting persists, as even directed approaches can result in undesired systemic effects. In contrast, our Palivizumab-based third generation SyCyR system, activated by engineered antibodies, offers unique advantages in specificity and control by exclusively targeting engineered cells. Additionally, SyCyRs offer a potential solution through the implementation of logical gating mechanisms while preserving natural signaling pathways. For instance, SyCyR-expressing engineered B cells can be engineered to exhibit dual antigen specificity, locally releasing IL-2 only when both a tumor antigen and a SyCyR-specific antibody targeting a second tumor antigen are present, which has been attempted against HIV (*167*) and other infectious diseases (*168*). SyCyRs could potentially also have a function in CAR NK cells (*169*).

6 Summary

Since the first cell-gene therapy was approved in 2017 the field evolved significantly and clinical trials as well as academic research progress at rapid speed. Novel components, like logic gates, death switches, and systems for different immune cells are being developed.

In this thesis I present significant advancements in the development of synthetic cytokine receptor (SyCyR) systems, specifically addressing the limitations of first-generation designs that utilized potentially immunogenic fluorescent proteins as ligands. The research introduces SyCyR^{2nd} and SyCyR^{3rd}, novel generations of synthetic receptors based on Palivizumab, an FDA-approved antibody targeting respiratory syncytial virus proteins being employed as a receptor agonist.

The cornerstone innovation lies in the development of anti-idiotypic nanobodies against Palivizumab (AIP), which were integrated as the receptor's extracellular binding domain. Engineering of the ligand included conversion to single-chain variable fragments (scFvs) with the Palivizumab antigen binding site, integration of Fc tags with varying spacer lengths (P^{scFv}23Fc, P^{scFv}LH0Fc, P^{scFv}LH4Fc, P^{scFv}LH8Fc), and transformation of Palivizumab's variable region to an IgG2 backbone (P^{IgG2}) which maintained binding affinity to AIP. While engineering of the receptor involved exploring four different anti-idiotypic nanobodies (AIP1-4) in the extracellular domain, and deletion of amino acids of the juxtamembrane stalk region between transmembrane and AIP^{VHH} in SyCyRs.

The development of SyCyR^{2nd} proved that activation of SyCyRs comprising of AIPs was possible with scFv with P^{scFv}23Fc but not Palivizumab.

While developing SyCyR^{3rd} it was demonstrated that AIP2^{VHH}gp130Δstalk andAIP3^{VHH}gp130Δstalk had enhanced biological activity with P^{scFv}23Fc and P^{scFv}8Fc. It Furthermore, P^{IgG2} had higher agonistic properties on the two aforementioned receptor variants in Ba/F3-gp130 and murine CD4+ and CD8+ T cells.

A notable achievement was the engineering of a tetravalent Fc fusion protein comprising four scFv fragemtns in tandem (2xP^{scFv}Fc) as well as Palivizumab variant (P^{scFv}P^{IgG2}) capable of inducing higher-order receptor clustering and activating Fas-induced apoptosis.

This system represents a significant advancement as it utilizes clinically approved components with established safety profiles and minimal immunogenicity, thereby offering enhanced potential for therapeutic applications in immunotherapy.

7 Zusammenfassung

Seit der Zulassung der ersten zellulären Gentherapie im Jahr 2017 hat sich das Feld erheblich weiterentwickelt, und klinische Versuche sowie die akademische Forschung schreiten in rasantem Tempo voran. Es werden neuartige Komponenten wie logische Gatter, Todesschalter und Systeme für verschiedene Immunzellen entwickelt.

In dieser Arbeit stelle ich wichtige Fortschritte in der Entwicklung synthetischer Zytokinrezeptorsysteme (SyCyR) vor, wobei ich insbesondere die Grenzen der ersten Generation von Designs anspreche, die potenziell immunogene fluoreszierende Proteine als Liganden verwenden. Die Forschung stellt SyCyR^{2nd} und SyCyR^{3rd} vor, neue Generationen von synthetischen Rezeptoren, die auf Palivizumab basieren, einem von der FDA zugelassenen Antikörper, der auf Proteine des Respiratorischen Synzytialvirus abzielt und als Rezeptor-Agonist eingesetzt wird.

Der Eckpfeiler der Innovation liegt in der Entwicklung von anti-idiotypischen Nanokörpern gegen Palivizumab (AIP), die als extrazelluläre Bindungsdomäne des Rezeptors integriert wurden. Die Entwicklung des Liganden umfasste die Umwandlung in einkettige variable Fragmente (scFvs) mit der Palivizumab-Antigenbindungsstelle, die Integration von Fc-Tags mit unterschiedlichen Spacerlängen (P^{scFv}23Fc, P^{scFv}LH0Fc, P^{scFv}LH4Fc, P^{scFv}LH8Fc) und die Umwandlung der variablen Region von Palivizumab in ein IgG2-Grundgerüst (P^{IgG2}), das die Bindungsaffinität zu AIP beibehält. Die Entwicklung von SyCyR^{2nd} hat gezeigt, dass die Aktivierung von SyCyRs, die aus AIPs bestehen, mit scFv mit P^{scFv}23Fc, aber nicht mit Palivizumab möglich war.

Bei der Entwicklung von SyCyR^{3rd} wurde nachgewiesen, dass AIP2^{VHH}gp130Δstalk undAIP3^{VHH}gp130Δstalk eine erhöhte biologische Aktivität mit P^{scFv}23Fc und P^{scFv}8Fc aufweisen. Darüber hinaus hatte P^{IgG2} höhere agonistische Eigenschaften auf die beiden oben genannten Rezeptorvarianten in Ba/F3 gp130 und CD4+ und CD8+ T-Zellen der Maus.

Ein weiterer Erfolg war die Entwicklung eines tetravalenten Fc-Fusionsproteins, das vier scFv-Fragmente im Tandem (2xP^{scFv}Fc) sowie eine Palivizumab-Variante (P^{scFv}P^{IgG2}) umfasst, die in der Lage ist, ein Rezeptor-Clustering höherer Ordnung zu induzieren und die Fas-induzierte Apoptose zu aktivieren.

Dieses System stellt eine wichtige weiterentwicklung dar, da es klinisch zugelassene Komponenten mit etablierten Sicherheitsprofilen und minimaler Immunogenität verwendet und damit ein größeres Potenzial für therapeutische Anwendungen in der Immuntherapie bietet.

8 References

1. K. Efstathiou, M. Efstathiou, Celestial Gearbox. *Mechanical Engineering* **140**, 31-35 (2018).
2. T. Freeth *et al.*, Decoding the ancient Greek astronomical calculator known as the Antikythera Mechanism. *Nature* **444**, 587-591 (2006).
3. A. D. Pinotsis, The Antikythera mechanism: who was its creator and what was its use and purpose? *Astronomical & Astrophysical Transactions* **26**, 211-226 (2007).
4. S. Dasgupta, *It Began with Babbage: The Genesis of Computer Science*. (Oxford University Press, 2014).
5. B. J. B. Copeland, Jonathan P.; Wilson, Robin; Sprevak, Mark, *The Turing Guide*. (Oxford University Press, 2017).
6. G. O'Regan, *A Brief History of Computing*. (Springer Science & Business Media, 2012).
7. D. Kahng, in *Semiconductor Devices: Pioneering Papers*. (1991), pp. 583-596.
8. J.-P. V. Deschamps, Elena; Terés, Lluís, *Digital Systems: From Logic Gates to Processors*. (Springer, 2016).
9. W. C. Ruder, T. Lu, J. J. Collins, Synthetic biology moving into the clinic. *Science* **333**, 1248-1252 (2011).
10. D. E. Cameron, C. J. Bashor, J. J. Collins, A brief history of synthetic biology. *Nat Rev Microbiol* **12**, 381-390 (2014).
11. Y. Wang, J. Xu, T. Pierson, B. W. O'Malley, S. Y. Tsai, Positive and negative regulation of gene expression in eukaryotic cells with an inducible transcriptional regulator. *Gene Ther* **4**, 432-441 (1997).
12. T. S. Moon, C. Lou, A. Tamsir, B. C. Stanton, C. A. Voigt, Genetic programs constructed from layered logic gates in single cells. *Nature* **491**, 249-253 (2012).
13. P. C. Heinrich, I. Behrmann, G. Muller-Newen, F. Schaper, L. Graeve, Interleukin-6-type cytokine signalling through the gp130/Jak/STAT pathway. *Biochem J* **334 (Pt 2)**, 297-314 (1998).
14. D. M. Floss, J. Schroder, M. Franke, J. Scheller, Insights into IL-23 biology: From structure to function. *Cytokine Growth Factor Rev* **26**, 569-578 (2015).
15. D. M. Floss, J. Scheller, Naturally occurring and synthetic constitutive-active cytokine receptors in disease and therapy. *Cytokine Growth Factor Rev* **47**, 1-20 (2019).
16. E. Y. Kim, K. D. Moudgil, Immunomodulation of autoimmune arthritis by pro-inflammatory cytokines. *Cytokine* **98**, 87-96 (2017).
17. S. A. Jones, J. Scheller, S. Rose-John, Therapeutic strategies for the clinical blockade of IL-6/gp130 signaling. *J Clin Invest* **121**, 3375-3383 (2011).
18. J. R. Tisoncik *et al.*, Into the eye of the cytokine storm. *Microbiol Mol Biol Rev* **76**, 16-32 (2012).
19. M. Akdis *et al.*, Interleukins, from 1 to 37, and interferon-gamma: receptors, functions, and roles in diseases. *J Allergy Clin Immunol* **127**, 701-721 e701-770 (2011).
20. J. F. Bazan, Structural design and molecular evolution of a cytokine receptor superfamily. *Proc Natl Acad Sci U S A* **87**, 6934-6938 (1990).
21. L. L. Jones, D. A. Vignali, Molecular interactions within the IL-6/IL-12 cytokine/receptor superfamily. *Immunol Res* **51**, 5-14 (2011).
22. W. J. Leonard, J. J. O'Shea, Jaks and STATs: biological implications. *Annu Rev Immunol* **16**, 293-322 (1998).
23. S. A. Jones, S. Horiuchi, N. Topley, N. Yamamoto, G. M. Fuller, The soluble interleukin 6 receptor: mechanisms of production and implications in disease. *FASEB J* **15**, 43-58 (2001).
24. J. Wolf, S. Rose-John, C. Garbers, Interleukin-6 and its receptors: a highly regulated and dynamic system. *Cytokine* **70**, 11-20 (2014).
25. M. J. Boulanger, K. C. Garcia, Shared cytokine signaling receptors: structural insights from the gp130 system. *Adv Protein Chem* **68**, 107-146 (2004).

26. A. L. Croxford, F. Mair, B. Becher, IL-23: one cytokine in control of autoimmunity. *Eur J Immunol* **42**, 2263-2273 (2012).
27. M. J. Boulanger, D. C. Chow, E. E. Brevnova, K. C. Garcia, Hexameric structure and assembly of the interleukin-6/IL-6 alpha-receptor/gp130 complex. *Science* **300**, 2101-2104 (2003).
28. N. Stahl *et al.*, Association and activation of Jak-Tyk kinases by CNTF-LIF-OSM-IL-6 beta receptor components. *Science* **263**, 92-95 (1994).
29. C. Stuhlmann-Laeisz *et al.*, Forced dimerization of gp130 leads to constitutive STAT3 activation, cytokine-independent growth, and blockade of differentiation of embryonic stem cells. *Mol Biol Cell* **17**, 2986-2995 (2006).
30. N. J. Kershaw *et al.*, SOCS3 binds specific receptor-JAK complexes to control cytokine signaling by direct kinase inhibition. *Nat Struct Mol Biol* **20**, 469-476 (2013).
31. U. Lehmann *et al.*, SHP2 and SOCS3 contribute to Tyr-759-dependent attenuation of interleukin-6 signaling through gp130. *J Biol Chem* **278**, 661-671 (2003).
32. K. Abell, C. J. Watson, The Jak/Stat pathway: a novel way to regulate PI3K activity. *Cell Cycle* **4**, 897-900 (2005).
33. T. Hou *et al.*, Roles of IL-6-gp130 Signaling in Vascular Inflammation. *Curr Cardiol Rev* **4**, 179-192 (2008).
34. S. Schreiber *et al.*, Therapeutic Interleukin-6 Trans-signaling Inhibition by Olamkicept (sgp130Fc) in Patients With Active Inflammatory Bowel Disease. *Gastroenterology* **160**, 2354-2366 e2311 (2021).
35. B. C. Trauth *et al.*, Monoclonal antibody-mediated tumor regression by induction of apoptosis. *Science* **245**, 301-305 (1989).
36. S. T. Ju *et al.*, Fas(CD95)/FasL interactions required for programmed cell death after T-cell activation. *Nature* **373**, 444-448 (1995).
37. M. Tanaka, T. Suda, T. Takahashi, S. Nagata, Expression of the functional soluble form of human fas ligand in activated lymphocytes. *EMBO J* **14**, 1129-1135 (1995).
38. H. T. Idriss, J. H. Naismith, TNFα and the TNF receptor superfamily: Structure-function relationship (s). *Microscopy research and technique* **50**, 184-195 (2000).
39. M. E. Peter, P. H. Krammer, The CD95(APO-1/Fas) DISC and beyond. *Cell Death Differ* **10**, 26-35 (2003).
40. L. S. Dickens *et al.*, A death effector domain chain DISC model reveals a crucial role for caspase-8 chain assembly in mediating apoptotic cell death. *Mol Cell* **47**, 291-305 (2012).
41. J.-H. Ahn *et al.*, Non-apoptotic Signaling Pathways Activated by Soluble Fas Ligand in Serum-starved Human Fibroblasts. *J Biol Chem* **276**, 47100-47106 (2001).
42. L. Wang *et al.*, Osteoblast-induced osteoclast apoptosis by fas ligand/FAS pathway is required for maintenance of bone mass. *Cell Death & Differentiation* **22**, 1654-1664 (2015).
43. D. J. Van Antwerp, S. J. Martin, I. M. Verma, D. R. Green, Inhibition of TNF-induced apoptosis by NF-κB. *Trends in cell biology* **8**, 107-111 (1998).
44. S. Gupta, Tumor necrosis factor-alpha-induced apoptosis in T cells from aged humans: a role of TNFR-I and downstream signaling molecules. *Exp Gerontol* **37**, 293-299 (2002).
45. S. J. Crowley *et al.*, Neoleukin-2 enhances anti-tumour immunity downstream of peptide vaccination targeted by an anti-MHC class II VHH. *Open Biol* **10**, 190235 (2020).
46. M. Guo *et al.*, Proliferation of Highly Cytotoxic Human Natural Killer Cells by OX40L Armed NK-92 With Secretory Neoleukin-2/15 for Cancer Immunotherapy. *Front Oncol* **11**, 632540 (2021).
47. H. N. Lode, R. Xiang, J. C. Becker, S. D. Gillies, R. A. Reisfeld, Immunocytokines: a promising approach to cancer immunotherapy. *Pharmacol Ther* **80**, 277-292 (1998).
48. D. Neri, P. M. Sondel, Immunocytokines for cancer treatment: past, present and future. *Curr Opin Immunol* **40**, 96-102 (2016).
49. J. Deng, J. Galipeau, Reprogramming of B cells into regulatory cells with engineered fusokines. *Infect Disord Drug Targets* **12**, 248-254 (2012).

50. B. Lipinski *et al.*, Generation and engineering of potent single domain antibody-based bispecific IL-18 mimetics resistant to IL-18BP decoy receptor inhibition. *MAbs* **15**, 2236265 (2023).
51. L. Pekar, S. Krah, S. Zielonka, Taming the beast: engineering strategies and biomedical potential of antibody-based cytokine mimetics. *Expert Opin Biol Ther* **24**, 115-118 (2024).
52. P. Rafii *et al.*, Cytokimera GIL-11 rescued IL-6R deficient mice from partial hepatectomy-induced death by signaling via non-natural gp130:LIFR:IL-11R complexes. *Commun Biol* **6**, 418 (2023).
53. J. Zhao, S. Turpin-Nolan, M. A. Febbraio, IL-6 family cytokines as potential therapeutic strategies to treat metabolic diseases. *Cytokine* **144**, 155549 (2021).
54. P. G. Spear, G. M. Edelman, Maturation of the humoral immune response in mice. *J Exp Med* **139**, 249-263 (1974).
55. W. Hoffman, F. G. Lakkis, G. Chalasani, B Cells, Antibodies, and More. *Clin J Am Soc Nephrol* **11**, 137-154 (2016).
56. A. F. Ochsenbein *et al.*, Control of early viral and bacterial distribution and disease by natural antibodies. *Science* **286**, 2156-2159 (1999).
57. R. L. Coffman, Surface antigen expression and immunoglobulin gene rearrangement during mouse pre-B cell development. *Immunol Rev* **69**, 5-23 (1982).
58. C. Zhang, Hybridoma technology for the generation of monoclonal antibodies. *Methods Mol Biol* **901**, 117-135 (2012).
59. D. R. Davies, S. Chacko, Antibody structure. *Accounts of chemical research* **26**, 421-427 (1993).
60. C. Janeway, P. Travers, M. Walport, M. Shlomchik, *Immunobiology: the immune system in health and disease*. (Garland Pub. New York, 2001), vol. 2.
61. A. Bastian, H. Kratzin, K. Eckart, N. Hilschmann, Intra- and interchain disulfide bridges of the human J chain in secretory immunoglobulin A. *Biol Chem Hoppe Seyler* **373**, 1255-1263 (1992).
62. R. J. Brezski, G. Georgiou, Immunoglobulin isotype knowledge and application to Fc engineering. *Curr Opin Immunol* **40**, 62-69 (2016).
63. P. Bruhns *et al.*, Specificity and affinity of human Fcgamma receptors and their polymorphic variants for human IgG subclasses. *Blood* **113**, 3716-3725 (2009).
64. S. Lightle *et al.*, Mutations within a human IgG2 antibody form distinct and homogeneous disulfide isomers but do not affect Fc gamma receptor or C1q binding. *Protein Sci* **19**, 753-762 (2010).
65. G. Vidarsson, G. Dekkers, T. Rispens, IgG subclasses and allotypes: from structure to effector functions. *Front Immunol* **5**, 520 (2014).
66. F. Nimmerjahn *et al.*, FcgammaRIV deletion reveals its central role for IgG2a and IgG2b activity in vivo. *Proc Natl Acad Sci U S A* **107**, 19396-19401 (2010).
67. M. Khalil, R. H. Vonderheide, Anti-CD40 agonist antibodies: preclinical and clinical experience. *Update Cancer Ther* **2**, 61-65 (2007).
68. C. M. Orr *et al.*, Hinge disulfides in human IgG2 CD40 antibodies modulate receptor signaling by regulation of conformation and flexibility. *Sci Immunol* **7**, eabm3723 (2022).
69. X. Yu *et al.*, Reducing affinity as a strategy to boost immunomodulatory antibody agonism. *Nature* **614**, 539-547 (2023).
70. S. S. Wang, Y. S. Yan, K. Ho, US FDA-approved therapeutic antibodies with high-concentration formulation: summaries and perspectives. *Antib Ther* **4**, 262-272 (2021).
71. H. Modjtahedi, S. Ali, S. Essapen, Therapeutic application of monoclonal antibodies in cancer: advances and challenges. *Br Med Bull* **104**, 41-59 (2012).
72. T. Tanaka, M. Narazaki, T. Kishimoto, Anti-interleukin-6 receptor antibody, tocilizumab, for the treatment of autoimmune diseases. *FEBS Lett* **585**, 3699-3709 (2011).

73. H. C. Meissner *et al.*, Immunoprophylaxis with palivizumab, a humanized respiratory syncytial virus monoclonal antibody, for prevention of respiratory syncytial virus infection in high risk infants: a consensus opinion. *Pediatr Infect Dis J* **18**, 223-231 (1999).
74. G. Casi, D. Neri, Antibody-drug conjugates: basic concepts, examples and future perspectives. *J Control Release* **161**, 422-428 (2012).
75. T. Oliphant *et al.*, Development of a humanized monoclonal antibody with therapeutic potential against West Nile virus. *Nat Med* **11**, 522-530 (2005).
76. M. S. Topp *et al.*, Targeted therapy with the T-cell-engaging antibody blinatumomab of chemotherapy-refractory minimal residual disease in B-lineage acute lymphoblastic leukemia patients results in high response rate and prolonged leukemia-free survival. *J Clin Oncol* **29**, 2493-2498 (2011).
77. D. Seimetz, H. Lindhofer, C. Bokemeyer, Development and approval of the trifunctional antibody catumaxomab (anti-EpCAM x anti-CD3) as a targeted cancer immunotherapy. *Cancer Treat Rev* **36**, 458-467 (2010).
78. T. Kitazawa *et al.*, A bispecific antibody to factors IXa and X restores factor VIII hemostatic activity in a hemophilia A model. *Nat Med* **18**, 1570-1574 (2012).
79. S. Krah, H. Kolmar, S. Becker, S. Zielonka, Engineering IgG-Like Bispecific Antibodies-An Overview. *Antibodies (Basel)* **7**, 28 (2018).
80. R. M. Giusti, K. A. Shastri, M. H. Cohen, P. Keegan, R. Pazdur, FDA drug approval summary: panitumumab (Vectibix). *Oncologist* **12**, 577-583 (2007).
81. J. I. Silverberg *et al.*, Phase 2B randomized study of nemolizumab in adults with moderate-to-severe atopic dermatitis and severe pruritus. *J Allergy Clin Immunol* **145**, 173-182 (2020).
82. B. Resch, Product review on the monoclonal antibody palivizumab for prevention of respiratory syncytial virus infection. *Hum Vaccin Immunother* **13**, 2138-2149 (2017).
83. A. Gupta *et al.*, Early Treatment for Covid-19 with SARS-CoV-2 Neutralizing Antibody Sotrovimab. *N Engl J Med* **385**, 1941-1950 (2021).
84. E. H. Choy *et al.*, Translating IL-6 biology into effective treatments. *Nat Rev Rheumatol* **16**, 335-345 (2020).
85. F. Cornillie, Ten years of infliximab (remicade) in clinical practice: the story from bench to bedside. *Eur J Pharmacol* **623 Suppl 1**, S1-4 (2009).
86. D. M. Pardoll, The blockade of immune checkpoints in cancer immunotherapy. *Nat Rev Cancer* **12**, 252-264 (2012).
87. J. Domachowske *et al.*, Safety of Nirsevimab for RSV in Infants with Heart or Lung Disease or Prematurity. *N Engl J Med* **386**, 892-894 (2022).
88. S. Mulangu, P. Mbala-Kingebeni, O. T. Mbaya, Antibody Use during an Outbreak of Ebola Virus Disease in the Democratic Republic of Congo, 2020. *N Engl J Med* **386**, 1188-1191 (2022).
89. J. Wesolowski *et al.*, Single domain antibodies: promising experimental and therapeutic tools in infection and immunity. *Med Microbiol Immunol* **198**, 157-174 (2009).
90. S. Y. Pan *et al.*, Immunomodulatory potential of anti-idiotypic antibodies for the treatment of autoimmune diseases. *Future Sci OA* **7**, FSO648 (2020).
91. H. D. Herce *et al.*, Cell-permeable nanobodies for targeted immunolabelling and antigen manipulation in living cells. *Nat Chem* **9**, 762-771 (2017).
92. M. Keyaerts *et al.*, Phase I Study of 68Ga-HER2-Nanobody for PET/CT Assessment of HER2 Expression in Breast Carcinoma. *J Nucl Med* **57**, 27-33 (2016).
93. W. Shi *et al.*, A new PD-1-specific nanobody enhances the antitumor activity of T-cells in synergy with dendritic cell vaccine. *Cancer Lett* **522**, 184-197 (2021).
94. M. Babamohamadi *et al.*, Anti-CTLA-4 nanobody as a promising approach in cancer immunotherapy. *Cell Death Dis* **15**, 17 (2024).
95. C. Ishiwatari-Ogata *et al.*, Ozoralizumab, a Humanized Anti-TNFalpha nanobody. Compound, Exhibits Efficacy Not Only at the Onset of Arthritis in a Human TNF Transgenic Mouse but

Also During Secondary Failure of Administration of an Anti-TNFalpha IgG. *Front Immunol* **13**, 853008 (2022).
96. M. Schoof *et al.*, An ultrapotent synthetic nanobody neutralizes SARS-CoV-2 by stabilizing inactive Spike. *Science* **370**, 1473-1479 (2020).
97. S. Kasturirangan *et al.*, Nanobody specific for oligomeric beta-amyloid stabilizes nontoxic form. *Neurobiol Aging* **33**, 1320-1328 (2012).
98. E. Pothin, D. Lesuisse, P. Lafaye, Brain Delivery of Single-Domain Antibodies: A Focus on VHH and VNAR. *Pharmaceutics* **12**, (2020).
99. S. Duggan, Caplacizumab: first global approval. *Drugs* **78**, 1639-1642 (2018).
100. Y. Pan, S. C. Yuhasz, L. M. Amzel, Anti-idiotypic antibodies: biological function and structural studies. *FASEB J* **9**, 43-49 (1995).
101. K. A. Schwarz, N. M. Daringer, T. B. Dolberg, J. N. Leonard, Rewiring human cellular input-output using modular extracellular sensors. *Nat Chem Biol* **13**, 202-209 (2017).
102. L. Scheller, T. Strittmatter, D. Fuchs, D. Bojar, M. Fussenegger, Generalized extracellular molecule sensor platform for programming cellular behavior. *Nat Chem Biol* **14**, 723-729 (2018).
103. L. Scheller, M. Fussenegger, From synthetic biology to human therapy: engineered mammalian cells. *Curr Opin Biotechnol* **58**, 108-116 (2019).
104. S. Mohammed *et al.*, Improving Chimeric Antigen Receptor-Modified T Cell Function by Reversing the Immunosuppressive Tumor Microenvironment of Pancreatic Cancer. *Mol Ther* **25**, 249-258 (2017).
105. J. Manhas, H. I. Edelstein, J. N. Leonard, L. Morsut, The evolution of synthetic receptor systems. *Nat Chem Biol* **18**, 244-255 (2022).
106. R. Kojima, L. Scheller, M. Fussenegger, Nonimmune cells equipped with T-cell-receptor-like signaling for cancer cell ablation. *Nat Chem Biol* **14**, 42-49 (2018).
107. L. Morsut *et al.*, Engineering Customized Cell Sensing and Response Behaviors Using Synthetic Notch Receptors. *Cell* **164**, 780-791 (2016).
108. A. E. Firor, A. Jares, Y. Ma, From humble beginnings to success in the clinic: Chimeric antigen receptor-modified T-cells and implications for immunotherapy. *Exp Biol Med (Maywood)* **240**, 1087-1098 (2015).
109. D. B. Kohn *et al.*, CARs on Track in the Clinic: Workshop of the Blood and Marrow Transplant Clinical Trials Network Subcommittee on Cell and Gene Therapy Washington DC, 18 May 2010. *Molecular therapy* **19**, 432-438 (2011).
110. W. Si, C. Li, P. Wei, Synthetic immunology: T-cell engineering and adoptive immunotherapy. *Synth Syst Biotechnol* **3**, 179-185 (2018).
111. S. Mossner, D. M. Floss, J. Scheller, Pro- and anti-apoptotic fate decisions induced by di- and trimeric synthetic cytokine receptors. *iScience* **24**, 102471 (2021).
112. E. Engelowski *et al.*, Synthetic cytokine receptors transmit biological signals using artificial ligands. *Nat Commun* **9**, 2034 (2018).
113. N. Zoellner *et al.*, Synthetic mimetics assigned a major role to IFNAR2 in type I interferon signaling. *Front Microbiol* **13**, 947169 (2022).
114. S. Mossner *et al.*, Synthetic interleukin 22 (IL-22) signaling reveals biological activity of homodimeric IL-10 receptor 2 and functional cross-talk with the IL-6 receptor gp130. *J Biol Chem* **295**, 12378-12397 (2020).
115. L. A. F. Baumgartner *et al.*, Unpaired cysteine insertions favor transmembrane dimerization and induce ligand-independent constitutive cytokine receptor signaling. *Biol Chem* **405**, 531-544 (2024).
116. J. S. Greiser, C. Stross, P. C. Heinrich, I. Behrmann, H. M. Hermanns, Orientational constraints of the gp130 intracellular juxtamembrane domain for signaling. *J Biol Chem* **277**, 26959-26965 (2002).
117. J. Martinez-Fabregas *et al.*, Kinetics of cytokine receptor trafficking determine signaling and functional selectivity. *Elife* **8**, e49314 (2019).

118. X. Wang, I. Riviere, Clinical manufacturing of CAR T cells: foundation of a promising therapy. *Mol Ther Oncolytics* **3**, 16015 (2016).
119. C. C. Kloss, M. Condomines, M. Cartellieri, M. Bachmann, M. Sadelain, Combinatorial antigen recognition with balanced signaling promotes selective tumor eradication by engineered T cells. *Nat Biotechnol* **31**, 71-75 (2013).
120. V. D. Fedorov, M. Themeli, M. Sadelain, PD-1- and CTLA-4-based inhibitory chimeric antigen receptors (iCARs) divert off-target immunotherapy responses. *Sci Transl Med* **5**, 215ra172 (2013).
121. M. Sadelain, I. Riviere, S. Riddell, Therapeutic T cell engineering. *Nature* **545**, 423-431 (2017).
122. G. Dotti, H. E. Heslop, Current status of genetic modification of T cells for cancer treatment. *Cytotherapy* **7**, 262-272 (2005).
123. C. Rossig, M. K. Brenner, Genetic modification of T lymphocytes for adoptive immunotherapy. *Mol Ther* **10**, 5-18 (2004).
124. A. H. Long *et al.*, 4-1BB costimulation ameliorates T cell exhaustion induced by tonic signaling of chimeric antigen receptors. *Nat Med* **21**, 581-590 (2015).
125. J. H. Esensten, Y. A. Helou, G. Chopra, A. Weiss, J. A. Bluestone, CD28 Costimulation: From Mechanism to Therapy. *Immunity* **44**, 973-988 (2016).
126. D. G. Song *et al.*, CD27 costimulation augments the survival and antitumor activity of redirected human T cells in vivo. *Blood* **119**, 696-706 (2012).
127. S. Guedan *et al.*, Enhancing CAR T cell persistence through ICOS and 4-1BB costimulation. *JCI Insight* **3**, (2018).
128. A. A. Hombach, J. Heiders, M. Foppe, M. Chmielewski, H. Abken, OX40 costimulation by a chimeric antigen receptor abrogates CD28 and IL-2 induced IL-10 secretion by redirected CD4(+) T cells. *Oncoimmunology* **1**, 458-466 (2012).
129. C. L. Flugel *et al.*, Overcoming on-target, off-tumour toxicity of CAR T cell therapy for solid tumours. *Nat Rev Clin Oncol* **20**, 49-62 (2023).
130. Q. Sun *et al.*, STAT3 regulates CD8+ T cell differentiation and functions in cancer and acute infection. *J Exp Med* **220**, (2023).
131. J. H. Choe *et al.*, SynNotch-CAR T cells overcome challenges of specificity, heterogeneity, and persistence in treating glioblastoma. *Sci Transl Med* **13**, eabe7378 (2021).
132. J. Khanali, M. Azangou-Khyavy, M. Boroomand-Saboor, M. Ghasemi, H. Niknejad, JAK/STAT-Dependent Chimeric Antigen Receptor (CAR) Expression: A Design Benefiting From a Dual AND/OR Gate Aiming to Increase Specificity, Reduce Tumor Escape and Affect Tumor Microenvironment. *Front Immunol* **12**, 638639 (2021).
133. D. Gumber, L. D. Wang, Improving CAR-T immunotherapy: Overcoming the challenges of T cell exhaustion. *EBioMedicine* **77**, 103941 (2022).
134. M. Koneru, R. O'Cearbhaill, S. Pendharkar, D. R. Spriggs, R. J. Brentjens, A phase I clinical trial of adoptive T cell therapy using IL-12 secreting MUC-16(ecto) directed chimeric antigen receptors for recurrent ovarian cancer. *J Transl Med* **13**, 102 (2015).
135. S. Depil, P. Duchateau, S. A. Grupp, G. Mufti, L. Poirot, 'Off-the-shelf' allogeneic CAR T cells: development and challenges. *Nat Rev Drug Discov* **19**, 185-199 (2020).
136. U. Mock *et al.*, Automated manufacturing of chimeric antigen receptor T cells for adoptive immunotherapy using CliniMACS prodigy. *Cytotherapy* **18**, 1002-1011 (2016).
137. V. Wang, M. Gauthier, V. Decot, L. Reppel, D. Bensoussan, Systematic Review on CAR-T Cell Clinical Trials Up to 2022: Academic Center Input. *Cancers (Basel)* **15**, (2023).
138. J. Ettich *et al.*, Respiratory syncytial virus-approved mAb Palivizumab as ligand for anti-idiotype nanobody-based synthetic cytokine receptors. *J Biol Chem* **299**, 105270 (2023).
139. M. A. Anderson *et al.*, Relative strength of cation-pi vs salt-bridge interactions: the Gtalpha(340-350) peptide/rhodopsin system. *J Am Chem Soc* **128**, 7531-7541 (2006).
140. M. Fischer *et al.*, I. A bioactive designer cytokine for human hematopoietic progenitor cell expansion. *Nat Biotechnol* **15**, 142-145 (1997).

141. J. E. Thompson *et al.*, Photochemical preparation of a pyridone containing tetracycle: a Jak protein kinase inhibitor. *Bioorg Med Chem Lett* **12**, 1219-1223 (2002).
142. M. A. Jambrich, G. E. Tusnady, L. Dobson, How AlphaFold2 shaped the structural coverage of the human transmembrane proteome. *Scientific Reports* **13**, 20283 (2023).
143. P. C. Fridy *et al.*, A robust pipeline for rapid production of versatile nanobody repertoires. *Nat Methods* **11**, 1253-1260 (2014).
144. U. Rothbauer *et al.*, A versatile nanotrap for biochemical and functional studies with fluorescent fusion proteins. *Mol Cell Proteomics* **7**, 282-289 (2008).
145. C. Vincke *et al.*, General strategy to humanize a camelid single-domain antibody and identification of a universal humanized nanobody scaffold. *J Biol Chem* **284**, 3273-3284 (2009).
146. M. Mirzaee Godarzee *et al.*, Strategies to overcome the side effects of chimeric antigen receptor T cell therapy. *Ann N Y Acad Sci* **1510**, 18-35 (2022).
147. C. Kim *et al.*, A therapeutic neutralizing antibody targeting receptor binding domain of SARS-CoV-2 spike protein. *Nat Commun* **12**, 288 (2021).
148. R. C. Group., Casirivimab and imdevimab in patients admitted to hospital with COVID-19 (RECOVERY): a randomised, controlled, open-label, platform trial. *Lancet* **399**, 665-676 (2022).
149. T. S. Migone *et al.*, Raxibacumab for the treatment of inhalational anthrax. *N Engl J Med* **361**, 135-144 (2009).
150. C. Wittich *et al.*, An engineered palivizumab IgG2 subclass for synthetic gp130 and fas-mediated signaling. *J Biol Chem* **301**, 108205 (2025).
151. V. S. Sheth, J. Gauthier, Taming the beast: CRS and ICANS after CAR T-cell therapy for ALL. *Bone Marrow Transplant* **56**, 552-566 (2021).
152. C. Kotch, D. Barrett, D. T. Teachey, Tocilizumab for the treatment of chimeric antigen receptor T cell-induced cytokine release syndrome. *Expert Rev Clin Immunol* **15**, 813-822 (2019).
153. J. Gust, R. Ponce, W. C. Liles, G. A. Garden, C. J. Turtle, Cytokines in CAR T Cell-Associated Neurotoxicity. *Front Immunol* **11**, 577027 (2020).
154. M. Wehrli *et al.*, Single-center experience using anakinra for steroid-refractory immune effector cell-associated neurotoxicity syndrome (ICANS). *J Immunother Cancer* **10**, (2022).
155. C. A. Ramos *et al.*, An inducible caspase 9 suicide gene to improve the safety of mesenchymal stromal cell therapies. *Stem Cells* **28**, 1107-1115 (2010).
156. M. Introna *et al.*, Genetic modification of human T cells with CD20: a strategy to purify and lyse transduced cells with anti-CD20 antibodies. *Hum Gene Ther* **11**, 611-620 (2000).
157. J. J. Melenhorst *et al.*, Decade-long leukaemia remissions with persistence of CD4+ CAR T cells. *Nature* **602**, 503-509 (2022).
158. N. Chen, X. Li, N. K. Chintala, Z. E. Tano, P. S. Adusumilli, Driving CARs on the uneven road of antigen heterogeneity in solid tumors. *Curr Opin Immunol* **51**, 103-110 (2018).
159. M. Hegde *et al.*, Tandem CAR T cells targeting HER2 and IL13Ralpha2 mitigate tumor antigen escape. *J Clin Invest* **126**, 3036-3052 (2016).
160. Z. Liang *et al.*, Tandem CAR-T cells targeting FOLR1 and MSLN enhance the antitumor effects in ovarian cancer. *Int J Biol Sci* **17**, 4365-4376 (2021).
161. M. Yang *et al.*, Tandem CAR-T cells targeting CD70 and B7-H3 exhibit potent preclinical activity against multiple solid tumors. *Theranostics* **10**, 7622-7634 (2020).
162. C. A. Land, P. R. Musich, D. Haydar, G. Krenciute, Q. Xie, Chimeric antigen receptor T-cell therapy in glioblastoma: charging the T cells to fight. *J Transl Med* **18**, 428 (2020).
163. M. J. Lajoie *et al.*, Designed protein logic to target cells with precise combinations of surface antigens. *Science* **369**, 1637-1643 (2020).
164. A. Hyrenius-Wittsten *et al.*, SynNotch CAR circuits enhance solid tumor recognition and promote persistent antitumor activity in mouse models. *Sci Transl Med* **13**, eabd8836 (2021).

165. K. Frey *et al.*, The immunocytokine F8-IL2 improves the therapeutic performance of sunitinib in a mouse model of renal cell carcinoma. *The Journal of urology* **184**, 2540-2548 (2010).
166. P. Williams, J. Galipeau, GM-CSF-based fusion cytokines as ligands for immune modulation. *J Immunol* **186**, 5527-5532 (2011).
167. A. D. Nahmad *et al.*, Engineered B cells expressing an anti-HIV antibody enable memory retention, isotype switching and clonal expansion. *Nat Commun* **11**, 5851 (2020).
168. H. F. Moffett *et al.*, B cells engineered to express pathogen-specific antibodies protect against infection. *Sci Immunol* **4**, eaax0644 (2019).
169. E. Wrona, M. Borowiec, P. Potemski, CAR-NK Cells in the Treatment of Solid Tumors. *Int J Mol Sci* **22**, 5899 (2021).

9 Supplemental information

Sequences of the four AIPs:

AIP1^{VHH} DVQLQESGGGLVQAGGSLRLSCVASGLTF-RYDMGWFRQAPGKEREFVAQITW-RGGSAT
AIP2^{VHH} DVQLQESGGGLVQAGGSLRLSCAASESLFRLNAMGWYRQAPGKQRELVAGIT---TSGDA
AIP3^{VHH} DVQLQESGGGLVQPGGSLRLSCVASGRTWSIYAMGWFRQAPGKEREFVTAISISRSESVT
AIP4^{VHH} DVQLQESGGGLVQAGGSLRLSCVASGRAFSRYDMGWFRQAPGKEREFVAQISW-RGGSAT

CDR1 **CDR2**

AIP1^{VHH} YYADSVKGRFTIARDIAKNAVYLQMNSLKPEDTAVYYCAAAYGSAGYRPDEYDSWGQGTQVTVSS
AIP2^{VHH} VYADSVKGRFTISRDSAKNTVYLQTNNLKPEDTAVYYCNVRPRAGTWENARIGVWGQGTQVTVSS
AIP3^{VHH} HYAESVTGRFTISRDNAKNTLHLQMNSLKPEDTAVYFCAADRRSID-PHHTIDYWGQGTQVTVSS
AIP4^{VHH} SYADTVKGRFTIARDNAKNTVYLQMNSLKPEDTAVYYCNA-------RTPTLSSWGQGTQVTVSS

CDR3

Examplatory sequences of AIP1^{VHH}gp130, AIP1^{VHH}gp130Δstalk and AIP1^{VHH}Fas

AIP1^{VHH}gp130

MSSSCSGLSRVLVAVATALVSASSEQKLISEEDLGSDVQLQESGGGLVQAGGSLRLSCVASGLTFRYDMGWFRQA
PGKEREFVAQITWRGGSATYYADSVKGRFTIARDIAKNAVYLQMNSLKPEDTAVYYCAAAYGSAGYRPDEYDSWG
QGTQVTVSSEFTFTTPKF**AQGEIE**AIVVPVCLAFLLTTLLGVLFCFNKRDLIKKHIWPNVPDPSKSHIAQWSPHT
PPRHNFNSKDQMYSDGNFTDVSVVEIEANDKKPFPEDLKSLDLFKKEKINTEGHSSGIGGSSCMSSSRPSISSSD
ENESSQNTSSTVQYSTVVHSGYRHQVPSVQVFSRSEATQPLLDSEERPEDLQLVDHVDGGDGILPRQQYFKQNCS
QHESSPDISHFERSKQVSSVNEEDFVRLKQQISDHISQSCGSGQMKMFQEVSAADAFGPGTEGQVERFETVGMEA
ATDEGMPKSYLPQTVRQGGYMPQAAARV

Signal peptide – Myc – AIP1^{VHH} – gp130(stalk in **bold**)

AIP1^{VHH}gp130Δstalk

MSSSCSGLSRVLVAVATALVSASSEQKLISEEDLGSDVQLQESGGGLVQAGGSLRLSCVASGLTFRYDMGWFRQA
PGKEREFVAQITWRGGSATYYADSVKGRFTIARDIAKNAVYLQMNSLKPEDTAVYYCAAAYGSAGYRPDEYDSWG
QGTQVTVSSEFTFTTPKFAIVVPVCLAFLLTTLLGVLFCFNKRDLIKKHIWPNVPDPSKSHIAQWSPHTPPRHNF
NSKDQMYSDGNFTDVSVVEIEANDKKPFPEDLKSLDLFKKEKINTEGHSSGIGGSSCMSSSRPSISSSDENESSQ
NTSSTVQYSTVVHSGYRHQVPSVQVFSRSEATQPLLDSEERPEDLQLVDHVDGGDGILPRQQYFKQNCSQHESSP
DISHFERSKQVSSVNEEDFVRLKQQISDHISQSCGSGQMKMFQEVSAADAFGPGTEGQVERFETVGMEAATDEGM
PKSYLPQTVRQGGYMPQAAARV

Signal peptide – Myc – AIP1^{VHH} – gp130

AIP1^{VHH}Fas

MSSSCSGLSRVLVAVATALVSASSEQKLISEEDLGSDVQLQESGGGLVQAGGSLRLSCVASGLTFRYDMGWFRQA
PGKEREFVAQITWRGGSATYYADSVKGRFTIARDIAKNAVYLQMNSLKPEDTAVYYCAAAYGSAGYRPDEYDSWG
QGTQVTVSSEFMCKEEGSRSNLGWLCLLLLPIPLIVWVKRKEVQKTCRKHRKENQGSHESPTLNPETVAINLSDV
DLSKYITTIAGVMTLSQVKGFVRKNGVNEAKIDEIKNDNVQDTAEQKVQLLRNWHQLHGKKEAYDTLIKDLKKAN
LCTLAEKIQTIILKDITSDSENSNFRNEIQSLV

Signal peptide – Myc – AIP1^{VHH} – Fas

Sequence alignment of single chain variant Fc fusions with different linker length

```
PscFvLH(23)Fc      MSSSCSGLSRVLVAVATALVSASSGQKLISEEDLTGDIQMTQSPSTLSASVGDRVTITCK  50
PscFvLH0Fc         MSSSCSGLSRVLVAVATALVSASSEQKLISEEDLTGDIQMTQSPSTLSASVGDRVTITCK  60
PscFvLH4Fc         MSSSCSGLSRVLVAVATALVSASSEQKLISEEDLTGDIQMTQSPSTLSASVGDRVTITCK  60
PscFvLH8Fc         MSSSCSGLSRVLVAVATALVSASSEQKLISEEDLTGDIQMTQSPSTLSASVGDRVTITCK  60
                   ************************************************************

PscFvLH(23)Fc      CQLSVGYMHWYQQKPGKAPKLLIYDTSKLASGVPSRFSGSGSGTAFTLTISSLQPDDFAT  110
PscFvLH0Fc         CQLSVGYMHWYQQKPGKAPKLLIYDTSKLASGVPSRFSGSGSGTAFTLTISSLQPDDFAT  120
PscFvLH4Fc         CQLSVGYMHWYQQKPGKAPKLLIYDTSKLASGVPSRFSGSGSGTAFTLTISSLQPDDFAT  120
PscFvLH8Fc         CQLSVGYMHWYQQKPGKAPKLLIYDTSKLASGVPSRFSGSGSGTAFTLTISSLQPDDFAT  120
                   ************************************************************

PscFvLH(23)Fc      YYCFQGSGYPFTFGGGTKLEIKGGGGSGGGGSGGGGSGGGGSGGGGSQVTLRESGPALVKPTQTL  170
PscFvLH0Fc         YYCFQGSGYPFTFGGGTKLEIKGGGGSGGGGSGGGGSGGGGSGGGGSQVTLRESGPALVKPTQTL  180
PscFvLH4Fc         YYCFQGSGYPFTFGGGTKLEIKGGGGSGGGGSGGGGSGGGGSGGGGSQVTLRESGPALVKPTQTL  180
PscFvLH8Fc         YYCFQGSGYPFTFGGGTKLEIKGGGGSGGGGSGGGGSGGGGSGGGGSQVTLRESGPALVKPTQTL  180
                   ************************************************************

PscFvLH(23)Fc      TLTCTFSGFSLSTSGMSVGWIRQPPGKALEWLADIWWDDKKDYNPSLKSRLTISKDTSAN  230
PscFvLH0Fc         TLTCTFSGFSLSTSGMSVGWIRQPPGKALEWLADIWWDDKKDYNPSLKSRLTISKDTSAN  240
PscFvLH4Fc         TLTCTFSGFSLSTSGMSVGWIRQPPGKALEWLADIWWDDKKDYNPSLKSRLTISKDTSAN  240
PscFvLH8Fc         TLTCTFSGFSLSTSGMSVGWIRQPPGKALEWLADIWWDDKKDYNPSLKSRLTISKDTSAN  240
                   ************************************************************

PscFvLH(23)Fc      QVVLKVTNMDPADTATYYCARSMITNWYFDVWGAGTTVTVSSAARENLYFQSAAAEFRSC  285
PscFvLH0Fc         QVVLKVTNMDPADTATYYCARSMITNWYFDVWGAGTTVTVSS------------------  282
PscFvLH4Fc         QVVLKVTNMDPADTATYYCARSMITNWYFDVWGAGTTVTVSSAAAEAAAKEAAAKEAAAK  294
PscFvLH8Fc         QVVLKVTNMDPADTATYYCARSMITNWYFDVWGAGTTVTVSSAAAEAAAKEAAAKEAAAK  300
                   ****************************************
```

Continued on next page

```
PscFvLH(23)Fc      DK----------------------THTCPPCPAPEAEGAPSVFLFPPKPKDTLMISRTP  327
PscFvLH0Fc         -------------------------AAACPPCPAPEAEGAPSVFLFPPKPKDTLMISRTP  317
PscFvLH4Fc         EAAAK--------------------AAACPPCPAPEAEGAPSVFLFPPKPKDTLMISRTP  340
PscFvLH8Fc         EAAAKEAAAKEAAAKEAAAKEAAAKAAACPPCPAPEAEGAPSVFLFPPKPKDTLMISRTP  360
                                           : :********************************

PscFvLH(23)Fc      EVTCVVVDVSHEDPEVKFNWYVDGVEVHNAKTKPREEQYNSTYRVVSVLTVLHQDWLNGK  387
PscFvLH0Fc         EVTCVVVDVSHEDPEVKFNWYVDGVEVHNAKTKPREEQYNSTYRVVSVLTVLHQDWLNGK  377
PscFvLH4Fc         EVTCVVVDVSHEDPEVKFNWYVDGVEVHNAKTKPREEQYNSTYRVVSVLTVLHQDWLNGK  400
PscFvLH8Fc         EVTCVVVDVSHEDPEVKFNWYVDGVEVHNAKTKPREEQYNSTYRVVSVLTVLHQDWLNGK  420
                   ************************************************************

PscFvLH(23)Fc      EYKCKVSNKALPAPIEKTISKAKGQPREPQVYTLPPSREEMTKNQVSLTCLVKGFYPSDI  447
PscFvLH0Fc         EYKCKVSNKALPAPIEKTISKAKGQPREPQVYTLPPSREEMTKNQVSLTCLVKGFYPSDI  437
PscFvLH4Fc         EYKCKVSNKALPAPIEKTISKAKGQPREPQVYTLPPSREEMTKNQVSLTCLVKGFYPSDI  460
PscFvLH8Fc         EYKCKVSNKALPAPIEKTISKAKGQPREPQVYTLPPSREEMTKNQVSLTCLVKGFYPSDI  480
                   ************************************************************

PscFvLH(23)Fc      AVEWESNGQPENNYKTTPPVLDSDGSFFLYSKLTVDKSRWQQGNVFSCSVMHEALHNHYT  507
PscFvLH0Fc         AVEWESNGQPENNYKTTPPVLDSDGSFFLYSKLTVDKSRWQQGNVFSCSVMHEALHNHYT  497
PscFvLH4Fc         AVEWESNGQPENNYKTTPPVLDSDGSFFLYSKLTVDKSRWQQGNVFSCSVMHEALHNHYT  520
PscFvLH8Fc         AVEWESNGQPENNYKTTPPVLDSDGSFFLYSKLTVDKSRWQQGNVFSCSVMHEALHNHYT  540
                   ************************************************************

PscFvLH(23)Fc      QKSLSLSPGK--      517
PscFvLH0Fc         QKSLSLSPGKGS      509
PscFvLH4Fc         QKSLSLSPGKGS      532
PscFvLH8Fc         QKSLSLSPGKGS      552
                   **********
```

Sequence alignment of heavy chains of P^{IgG1} and P^{IgG2}

```
PIgG1      QVTLRESGPALVKPTQTLTLTCTFSGFSLSTSGMSVGWIRQPPGKALEWLADIWWDDKKD   60
PIgG2      QVTLRESGPALVKPTQTLTLTCTFSGFSLSTSGMSVGWIRQPPGKALEWLADIWWDDKKD   60
           ************************************************************

PIgG1      YNPSLKSRLTISKDTSANQVVLKVTNMDPADTATYYCARSMITNWYFDVWGAGTTVTVSS   120
PIgG2      YNPSLKSRLTISKDTSANQVVLKVTNMDPADTATYYCARSMITNWYFDVWGAGTTVTVSS   120
           ************************************************************

PIgG1      ASTKGPSVFPLAPSSAAAAGGTAALGCLVKDYFPEPVTVSWNSGALTSGVHTFPAVLQSS   180
PIgG2      ASTKGPSVFPLAPCSRSTSESTAALGCLVKDYFPEPVTVSWNSGALTSGVHTFPAVLQSS   180
           *************.* ::: .**************************************

PIgG1      GLYSLSSVVTVPSSSLGTQTYICNVNHKPSNTKVDKRVEPKSCDKTHTCPPCPAPELLGG   240
PIgG2      GLYSLSSVVTVPSSNFGTQTYTCNVDHKPSNTKVDKTVERKSCV---ECPPCPAPPV-AG   236
           **************.:***** ***:********** ** ***     ******* : .*

PIgG1      PSVFLFPPKPKDTLMISRTPEVTCVVVDVSHEDPEVKFNWYVDGVEVHNAKTKPREEQYN   300
PIgG2      PSVFLFPPKPKDTLMISRTPEVTCVVVDVSHEDPEVQFNWYVDGVEVHNAKTKPREEQFN   296
           ************************************:*********************:*

PIgG1      STYRVVSVLTVLHQDWLNGKEYKCKVSNKALPAPIEKTISKAKGQPREPQVYTLPPSRDE   360
PIgG2      STFRVVSVLTVVHQDWLNGKEYKCKVSNKGLPAPIEKTISKTKGQPREPQVYTLPPSREE   356
           **:********:*****************.***********:****************:*

PIgG1      LTKNQVSLTCLVKGFYPSDIAVEWESNGQPENNYKTTPPVLDSDGSFFLYSKLTVDKSRW   420
PIgG2      MTKNQVSLTCLVKGFYPSDIAVEWESNGQPENNYKTTPPMLDSDGSFFLYSKLTVDKSRW   416
           :************************************:**********************

PIgG1      QQGNVFSCSVMHEALHNHYTQKSLSLSPGK---  450
PIgG2      QQGNVFSCSVMHEALHNHYTQKSLSLSPGKGSG 449
           ******************************
```

Cysteins mutated to serins are red and underlined

Sequence alignment of light chains of P^{IgG1} and P^{IgG2}

```
PIgG1      DIQMTQSPSTLSASVGDRVTITCKCQLSVGYMHWYQQKPGKAPKLLIYDTSKLASGVPSR   60
PIgG2      DIQMTQSPSTLSASVGDRVTITCKCQLSVGYMHWYQQKPGKAPKLLIYDTSKLASGVPSR   60
           ************************************************************

PIgG1      FSGSGSGTAFTLTISSLQPDDFATYYCFQGSGYPFTFGGGTKLEIKRTVAAPSVFIFPPS   120
PIgG2      FSGSGSGTAFTLTISSLQPDDFATYYCFQGSGYPFTFGGGTKLEIKRTVAAPSVFIFPPS   120
           ************************************************************

PIgG1      DEQLKSGTASVVCLLNNFYPREAKVQWKVDNALQSGNSQESVTEQDSKDSTYSLSSTLTL   180
PIgG2      DEQLKSGTASVVCLLNNFYPREAKVQWKVDNALQSGNSQESVTEQDSKDSTYSLSSTLTL   180
           ************************************************************

PIgG1      SKADYEKHKVYACEVTHQGLSSPVTKSFNRGEC 213
PIgG2      SKADYEKHKVYACEVTHQGLSSPVTKSFNRGES 213
           ********************************.
```

Cysteins mutated to serins are red and underlined

Sequence of $P^{scFv}P^{IgG2}$

Heavy Chain

```
PscFvPIgG2 DIQMTQSPSTLSASVGDRVTITCKCQLSVGYMHWYQQKPGKAPKLLIYDTSKLASGVPSR 60
PscFvPIgG2 FSGSGSGTAFTLTISSLQPDDFATYYCFQGSGYPFTFGGGTKLEIKGGGGSGGGGSGGGG 120
PscFvPIgG2 SGGGGSQVTLRESGPALVKPTQTLTLTCTFSGFSLSTSGMSVGWIRQPPGKALEWLADIW 180
PscFvPIgG2 WDDKKDYNPSLKSRLTISKDTSANQVVLKVTNMDPADTATYYCARSMITNWYFDVWGAGT 240
PscFvPIgG2 TVTVSSPRGGGGSGGGGSGGGGSGGGGSDQVTLRESGPALVKPTQTLTLTCTFSGFSLST 300
PscFvPIgG2 SGMSVGWIRQPPGKALEWLADIWWDDKKDYNPSLKSRLTISKDTSANQVVLKVTNMDPAD 360
PscFvPIgG2 TATYYCARSMITNWYFDVWGAGTTVTVSSASTKGPSVFPLAPCSRSTSESTAALGCLVKD 420
PscFvPIgG2 YFPEPVTVSWNSGALTSGVHTFPAVLQSSGLYSLSSVVTVPSSNFGTQTYTCNVDHKPSN 480
PscFvPIgG2 TKVDKTVERKSCVECPPCPAPPVAGPSVFLFPPKPKDTLMISRTPEVTCVVVDVSHEDPE 540
PscFvPIgG2 VQFNWYVDGVEVHNAKTKPREEQFNSTFRVVSVLTVVHQDWLNGKEYKCKVSNKGLPAPI 600
PscFvPIgG2 EKTISKTKGQPREPQVYTLPPSREEMTKNQVSLTCLVKGFYPSDIAVEWESNGQPENNYK 660
PscFvPIgG2 TTPPMLDSDGSFFLYSKLTVDKSRWQQGNVFSCSVMHEALHNHYTQKSLSLSPGK 715
```

Light Chain

```
PscFvPIgG2 DIQMTQSPSTLSASVGDRVTITCKCQLSVGYMHWYQQKPGKAPKLLIYDTSKLASGVPSR 60
PscFvPIgG2 FSGSGSGTAFTLTISSLQPDDFATYYCFQGSGYPFTFGGGTKLEIKRTVAAPSVFIFPPS 120
PscFvPIgG2 DEQLKSGTASVVCLLNNFYPREAKVQWKVDNALQSGNSQESVTEQDSKDSTYSLSSTLTL 180
PscFvPIgG2 SKADYEKHKVYACEVTHQGLSSPVTKSFNRGES 213
```

10 Eidesstattliche Versicherung

Hiermit versichere ich an Eides Statt, dass die her vorliegende Dissertation selbstständig und nur mit Hilfe der angegebenen Hilfsmittel und Quellen unter Beachtung der „Grundsätze zur Sicherung guter wissenschaftlicher Praxis an der Heinrich-Heine-Universität Düsseldorf“ verfasst wurde. Alle Zitate sind gemäß §6 Abs. 7 MAPO kenntlich gemacht. Diese Dissertation wurde in der hier vorgelegten oder ähnlichen Form noch bei keiner anderen Institution eingereicht. Bisher wurden von mir keine erfolglosen Promotionsversuche unternommen.

Düsseldorf den 06 März 2025

Christoph Wittich

11 Note of thanks

First, I would like to express my gratitude to Prof. Dr. Jürgen Scheller, who made it possible for me to complete my dissertation at the Institute of Biochemistry and Molecular Biology II. I would particularly like to emphasize that I was always able to contribute my own ideas, and through constructive discussions, we were able to find solutions to all scientific questions. Furthermore, I deeply appreciate the support and trust you consistently showed throughout my research.

I would also like to thank Prof. Dr. Lutz Schmitt for his mentorship and for agreeing to review this thesis.

While all members of the institute were supportive during my time there, Dr. Doreen M. Floss truly stood out. She was always helpful in any situation, often solving problems before we even noticed they existed. Her proactive approach and motivational spirit were truly inspiring.

For their invaluable scientific input, engaging discussions, and unwavering helpfulness, I extend my thanks to Dr. Silke Pudewell and Julia Ettich. Without their contributions, my projects would have taken a completely different direction.

The most significant support came from my girlfriend, Chiara Calabrese, who not only helped me by reading through the thesis but also supported me unconditionally throughout this journey. I am truly grateful to have you by my side.

Lastly, I want to thank my parents, Monika and Ulrich Wittich, for always being there for me and supporting me, especially in moments when they might not have agreed with my decisions.